Plane channel flow simulation over porous walls

Technical Note: **ETSIA /MF-9809**

J. Jiménez
A. Pinelli
M. Uhlmann

FROM:
Departamento de Mecánica de Fluidos
E. T. Superior de Ingenieros Aeronáuticos
Universidad Politécnica Madrid.

TO:

BRITE AEROMEMS Consortium

August 1998
(Revised, April 1999)

Contents

1 Introduction

Since many technologically relevant flows can be characterized as turbulent, feasible methods of modifying turbulent flow features according to specific needs are a highly desirable objective. One prominent example of turbulence control is the aim of drag reduction that has received considerable attention in view of evident advantages in external aerodynamics (e.g. [5, 4, 22]). Recent advances in micro-machinery have fueled the hope to be able to efficiently manipulate turbulent wall-bounded flows in many applications by using micron size flow sensor and actuator arrangements (MEMS). However, apart from the technological challenge of size, cost, performance and maintenance of MEMS devices, the underlying fluid mechanical problem is yet to be resolved, namely the understanding of the dynamics of turbulent flow near a boundary being subjected to some kind of manipulation.

Recently, several aspects of how turbulence maintains itself near a solid boundary have been clarified [8, 31, 17]. One can speak of a regeneration cycle with streamwise elongated vortices and velocity streaks as the principal protagonists, generating each other mutually through advection and instability mechanisms. This structural model of near-wall turbulence production proves to be very useful in interpreting the results from artificial modifications of the boundary such as the porous wall condition which is the subject of the present study.

Other than the obvious goal of direct drag-reduction, one sometimes wishes to increase drag upon a body – at least locally. This is the case of near-critical airfoils where flow-separation is to be avoided or delayed. A possible strategy to achieve this is an enhancement of near-wall turbulence which brings more momentum towards the wall such that the boundary layer can resist longer against adverse pressure gradients. One example of a very simple control mechanism in this sense is the use of a permeable wall. The possibility of positive or negative injection of mass ("blowing" or "suction") with the aim of controlling the development of boundary layers has been studied as early as the beginning of this century (Prandtl, cf. [30]). We are, however, concerned with a permeable wall of an essentially mass-neutral type, i.e. no mass is injected on the average into the flow. To this end let us consider a situation in which the flow of interest is developing over a porous wall that allows for transverse velocities according to Darcy's law for porous media (cf. [2, p. 224 ff.]), i.e. the velocity normal to the wall is proportional to the pressure drop across the wall. We adjust the pressure in the adjacent plenum chamber to be equal to the mean flow pressure of the boundary layer such that local "blowing" and "suction" is created only due to local turbulent pressure fluctuations, averaging out to zero over a sufficiently long interval in time (or an ensemble of realizations). At the same time, the porous wall is supposed to be fabricated such that no velocities parallel to the wall are induced on the surface, i.e. that the no-slip condition is obeyed. We note that such wall conditions have been used in attempts to alleviate shock movement on transonic airfoils [7]. In the following, we will be concerned with the response of developed, low-Reynolds number turbulence to such a "non-generic" boundary. With respect to control theory, this type of manipulation can be termed as "passive" although it constitutes a closed loop with Darcy's law acting as the feedback from the flow itself.

To our knowledge the number of previous studies dealing with permeable wall turbulence is quite limited. Perot and Moin [27] investigated perfectly permeable and free slip walls in the absence of mean shear. Their direct simulations revealed that – against intuition – it is the condition acting on the wall-parallel velocity component (no-slip) that is responsible for the intercomponental energy transfer near the wall and not the condition on the wall-normal component. More recently, Wagner and Friedrich [34] (see also [33]) presented a numerical study of flow in perfectly permeable pipes, showing a nearly sixfold rise in wall friction compared to a solid pipe (at a bulk Reynolds number of 5500). Along with higher near-wall turbulence intensity goes an increase in streak spacing and a visible change in near-wall structures, according to these authors. With respect to our porous wall condition, the perfectly permeable wall discussed in the above references constitutes the limiting case of infinite porosity.

Besides the mentioned technological application, the study of turbulence near a porous surface (or in general: a permeable wall) can be seen in line with a number of previous experiments with non-generic walls (shear-free wall turbulence of Hunt and Graham [11]; shear flow and free-slip with regards to fluctuations, Banerjee and co-workers [29, 24]; altered no-slip experiments of Jiménez [12]; the mentioned simulations of Perot and Moin [27]). These studies share a common approach: to separate and clarify the different mechanisms due to the presence of a wall in turbulent flow. The present work can contribute to this purpose by focusing on the impermeability condition of a wall and the effects that relaxing the constraint has on the flow.

The present report is structured as follows. After this brief introduction we will specify the mathematical formulation of the flow problem. Section 3 explains the details of the numerical method used to generate the flow data of plane channel flow at different levels of porosity. In section 4 we will present and discuss the statistics and selected snapshots of our simulations before drawing some conclusions in section 5.

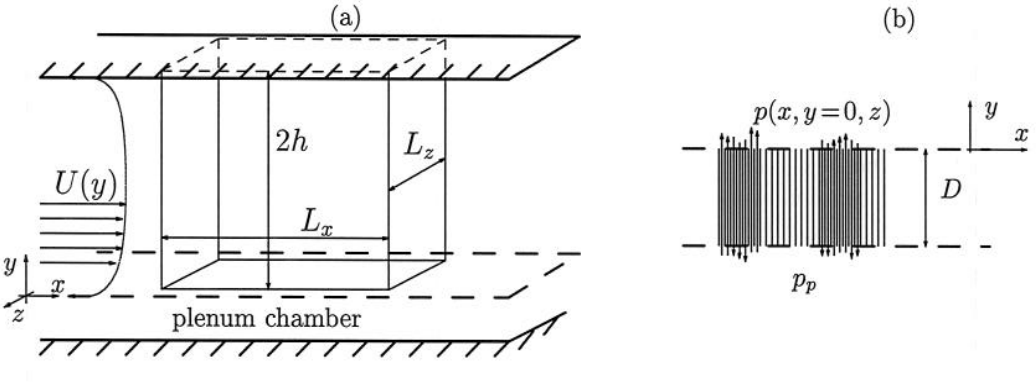

Figure 1: (a) Schematic of the plane channel flow configuration with one porous wall, indicating the domain of integration. (b) Detail of the porous wall below the channel flow.

2 Formulation of the problem

The Navier-Stokes equations governing incompressible flow can be cast into the form [19] of a fourth order equation for the velocity component v,

$$\partial_t(\nabla^2 v) \;=\; h_v \;+\; \frac{1}{\mathrm{Re}}\nabla^2(\nabla^2 v)\,, \tag{1}$$

a second order equation for the corresponding vorticity component ω_y,

$$\partial_t(\omega_y) \;=\; h_g \;+\; \frac{1}{\mathrm{Re}}\nabla^2(\omega_y)\,, \tag{2}$$

and the continuity equation:

$$\nabla\cdot\vec{v} \;=\; 0\,, \tag{3}$$

where the non-linear (advection) terms are defined as:

$$h_v = (\partial_{xx}+\partial_{zz})\,H_2-\partial_{xy}H_1-\partial_{yz}H_3\,,\quad h_g = \partial_z H_1-\partial_x H_3\,,\quad H \;=\; -\left(\vec{\omega}\,\times\,\vec{v}\;+\;\frac{1}{2}\nabla(|\vec{v}^2|)\right)\,. \tag{4}$$

In the above system, all quantities have been non-dimensionalised by the reference length scale h and the velocity U_0, such that the Reynolds number is defined as $\mathrm{Re} \;=\; U_0 h/\nu$, where ν is the kinematic viscosity of the fluid. The main advantage of the above formulation resides in the cancellation of the pressure term and its associated need for a special treatment that arises in an incompressible setting.

The flow configuration we wish to investigate is that of fully developed plane channel flow of infinite spanwise dimension (see figure 1). The domain of integration extends from wall to wall over $L_y = 2h$ as well as over a length of $L_x/h = 2\pi/\alpha$ and $L_z/h = 2\pi/\beta$ in streamwise and spanwise periodic directions respectively.

Boundary conditions need to be provided in the planes $y=0$ and $y=2h$. Both walls obey the no slip condition, viz.

$$u(x, y=y_w, z) = 0, \quad w(x, y=y_w, z) = 0 \qquad y_w = \{0, 2h\}\quad . \tag{5}$$

The upper wall is impermeable, such that

$$v(x, y=2h, z) = 0 \quad . \tag{6}$$

The lower boundary is the interface between the channel and a porous medium across which Darcy's law can be invoked under the assumption that the characteristic Reynolds number of the flow in that medium is small enough to justify neglecting inertial forces [2], thus

$$\nabla p^*/\rho^* = -\frac{\nu^*}{k^*} \cdot \vec{v}^* \quad , \tag{7}$$

where k^* is a constant called the *permeability* of the medium, having the dimension of a surface, and p^*/ρ^* is the kinematic pressure (dimensional quantities are indicated by an asterisk). Allowing for percolation in the wall-normal direction y, integration of (7) over a porous wall of thickness D^* gives:

$$(p^*(x, y\!=\!0, z) - p_p^*)/\rho^* = -\frac{\nu^*}{k^*}\, v^*\, D^* \quad . \tag{8}$$

Adjusting the plenum pressure p_p to be equal to the mean pressure of the flow in the channel, $p_p^* \!=\! \overline{p}^*(x)$, lets us express the pressure difference across the wall through the pressure fluctuations $p'(x, y = 0, z)$ on the lower wall of the channel only. Using our habitual reference values $(h,\, U_0)$, the non-dimensional wall boundary condition can be expressed as:

$$v \;=\; -p'/\rho\, \frac{\mathrm{Re}}{C_\beta} \quad , \tag{9}$$

or, equivalently, using wall units as the reference values:

$$v^+ \;=\; -p^+\, \frac{\mathrm{Re}_\tau}{C_\beta}\,, \qquad \text{where} \quad v^+ = \frac{v}{u_\tau},\; p^+ = \frac{p'/\rho}{u_\tau^2},\; \mathrm{Re}_\tau = \frac{u_\tau\, h}{\nu}\,. \quad . \tag{10}$$

Concerning the study of the flow in the indicated domain of integration, the constant C_β alone determines the degree of porosity of the boundary. Through the condition (9), the transpiration velocity is thus linked directly to the local pressure fluctuations. In other words, a perfect anti-correlation is forced between pressure and wall-normal velocity at the lower wall. Note that this formulation automatically guarantees the condition to be "mass-neutral", since taking the mean of (9) gives $\overline{v}(x, y\!=\!0, z)\!=\!0$. The limiting cases with respect to porosity are the following: as the coefficient of porosity goes to infinity the wall becomes impermeable, $\lim_{C_\beta \to \infty}(v(x, y\!=\!0, z))\!=\!0$; in the opposite case of unlimited porosity ($C_\beta \to 0$), the pressure difference simultaneously goes to zero and the wall-normal velocity becomes unconstrained as in the case of a free boundary.

3 Numerical method

Our approach is generally quite similar to the one employed by Kim *et al.* [19] which formed the blueprint to a former version of the present method [17]. The fact that the wall-normal velocity can take appreciable values in the vicinity of the computational domain boundary where the grid size is very small constitutes a serious restriction on the time step. When using Chebychev polynomials in the expansion of variables in the wall-normal direction, the method becomes prohibitively expensive due to the fact that the corresponding Gauss-Lobatto points for numerical quadrature are situated very close the wall. In the present method we have opted to use b-splines instead as the wall-normal expansion functions, allowing for an arbitrary choice of the knot points. In the two periodic directions of the flow (streamwise and spanwise) a Fourier expansion is employed.

The method for approximating the spatial derivatives is pseudo-spectral in that we calculate the non-linear terms (h_v, h_g) in physical space at individual collocation points. In the periodic direction the transformations between Fourier and physical space are carried out by standard Fast-Fourier-Transforms and dealiasing according to the $3/2$ rule. The system of equations is then solved by a Galerkin method of weighted residuals with those non-linear terms as (explicit) forcing terms. Through this procedure, the algorithm is essentially broken into a succession of one-dimensional (biharmonic and individual) Helmholtz problems for each Fourier mode. The time advancement is performed by a three-step, low-storage Runge-Kutta scheme of third order accuracy, such that the following schematic algorithm is obtained:

```
for $n = 1 \dots N_{it}$
    for $k = 1 \dots 3$
        • calculate    $(f_{NL})^{n+(k-1)/3}$    pseudo-spectrally,
        • solve
              $\frac{\phi^{n+k/3} - \phi^n}{\Delta t\, \alpha_k} - \frac{1}{\mathrm{Re}} \nabla^2(\phi^{n+k/3}) = (f_{NL})^{n+(k-1)/3}$,    $\alpha_k = \{\frac{1}{3}, \frac{1}{2}, 1\}$        (11)
              by a Galerkin MWR,
```

where $\phi = \{\nabla^2(v), \omega_y\}$ and $f_{NL} = \{h_v, h_g\}$.

3.1 Collocation method for the non-linear terms

3.1.1 General method

The advantage of the pseudo-spectral collocation method is that the non-linear terms can be evaluated efficiently when using fast Fourier transforms to change back and forth between physical and spectral space at each time step. However, specific care has to be taken at the boundaries when using expressions computed by a (pointwise) collocation method within a Galerkin scheme (see section 3.2).

Unlike a Galerkin method, a collocation method uses the coefficients of an expansion of the variables in an intermediate step of analytic differentiation only [3]. In this spirit, we expand the variables of the problem in terms of spectral functions in the periodic directions x, z:

$$\phi(x, y, z) = \sum_{k_x, k_z} \hat{\phi}(k_x, y, k_z) \cdot e^{ik_x x} \cdot e^{ik_z z} \quad . \tag{12}$$

Note that we could systematically use our choice of b-spline functional expansion in y to obtain straightforward analytic expressions in that direction as well. However, a direct nth derivation of an expansion in terms of b-splines of order o leads to an approximation of order $o-2(n-1)$ in the collocation framework. With the aim of reducing the computational cost needed to achieve a given formal accuracy, we use a relatively low order b-spline base ($o=4$) combined with an explicit finite difference stencil to express derivatives in the direction y (in fact, as seen from (4), only first derivatives in y appear in the non-linear terms). This approach thus bears some resemblance to a compact finite difference method for its implicit character. Let us denote the numerical representation of a wall-normal derivative of a variable ϕ at a point (x, y_i, z) by:

$$\hat{\phi}_i^S(k_x, k_z) \cdot e^{ik_x x} \cdot e^{ik_z z} = \partial_y(\hat{\phi}(k_x, y_i, k_z) \cdot e^{ik_x x} \cdot e^{ik_z z}) \quad . \tag{13}$$

The details of this numerical derivative as well as its resolution properties can be found in appendix A.1. The final expression only involves the inversion of a tridiagonal matrix – a quite economical operation.

3.1.2 Solving for velocity and vorticity components

According to their definition (4), the computation of the non-linear terms h_v and h_g requires the knowledge of individual velocity and vorticity components. The independent variables of the problem being $\varphi = \nabla^2(v)$, v and ω_y, the missing components have to be deduced first before the non-linear terms can be computed. Using the continuity equation (3) and the definition of y-vorticity, $\omega_y = \partial_z u - \partial_x w$, the following algebraic relations are obtained for the Fourier coefficients:

$$\left.\begin{array}{rcr} \hat{\omega}_z(k_x, y_i, k_z) &=& \left(\hat{\varphi} + \dfrac{k_z}{k_x}(\hat{\omega}_y)_i^S\right) / \left(ik_x - \dfrac{k_z}{ik_x}\right) \\ \hat{\omega}_x(k_x, y_i, k_z) &=& \left((\hat{\omega}_y)_i^S - ik_z\hat{\omega_z}\right) / (ik_x) \\ \hat{w}(k_x, y_i, k_z) &=& \left(-\hat{v}_i^S - \dfrac{k_x}{k_z}\hat{\omega}_y\right) / \left(\dfrac{ik_x^2}{k_z} + ik_z\right) \\ \hat{u}(k_x, y_i, k_z) &=& (\hat{\omega}_y + ik_x\hat{w}) / (ik_z) \end{array}\right\} \quad k_x, k_z \neq 0 \tag{14}$$

and

$$\begin{array}{l} \left.\begin{array}{rcr} \hat{\omega}_z(k_x, y_i, k_z) &=& -(\hat{\omega}_y)_i^S/(ik_z) \\ \hat{\omega}_x(k_x, y_i, k_z) &=& -\hat{\varphi}/(ik_z) \end{array}\right\} \quad k_x = 0, k_z \neq 0 \\ \left.\begin{array}{rcr} \hat{w}(k_x, y_i, k_z) &=& -\hat{\omega}_y/(ik_x) \\ \hat{u}(k_x, y_i, k_z) &=& -\hat{v}_i^S/(ik_x) \end{array}\right\} \quad k_z = 0, k_x \neq 0 \end{array} \tag{15}$$

The expressions for the constant mode ($k_x = 0 \cap k_z = 0$) are not needed since in that case, the equations for the velocity components are directly solved (see below equation (23)).

3.2 Galerkin method for the viscous terms

Initially, the fourth order equation (1) is split up into two coupled second order equations, viz.

$$\left.\begin{array}{rcl} \partial_t(\varphi) - \dfrac{1}{\mathrm{Re}}\nabla^2(\varphi) &=& h_v \\ \nabla^2(v) &=& \varphi\,, \end{array}\right\} \tag{16}$$

such that we need to solve a bi-Helmholtz problem in conjunction with the ordinary Helmholtz equation for vorticity (2). This step facilitates the implementation of various boundary conditions when dealing with a fourth order formulation for velocity v.

We expand the independent variables in terms of spectral and b-spline functions, viz.:

$$\phi(x,y,z) = \sum_{k_x,k_z} \sum_{j=1}^{Ns} \hat{\phi}_j(k_x,k_z)\cdot e^{ik_x x}\cdot e^{ik_z z}\cdot B_j^o(y)\,, \qquad \phi = \{\varphi, v, \omega_y\} \quad . \tag{17}$$

The b-splines B_j^o employed in the Galerkin part of our numerical method are of order $o\!=\!6$. More information about the construction of the specific spline base and its characteristics can be found in appendix A.2.

Resorting to a Galerkin method of weighted residuals as indicated in schematic (11), i.e. inserting test functions

$$\Psi(x,y,z) = e^{-ik_x x}\cdot e^{-ik_z z}\cdot B_i^o(y) \quad , \tag{18}$$

into equations (16) and (2) and integrating over the domain of integration Ω leads to the following system of equations for each pair of modes k_x, k_z and b-spline coefficient j, written at a Runge-Kutta substep k of a time step n:

$$\begin{aligned}
&\sum_j \hat{\varphi}_j^{n+k/3}(k_x,k_z)\int B_j''(y)\,B_i(y)\,\mathrm{d}y - \left(k_x^2+k_z^2+\frac{\mathrm{Re}}{\alpha_k\Delta t}\right)\sum_j \hat{\varphi}_j^{n+k/3}\int B_j(y)\,B_i(y)\,\mathrm{d}y = \\
&\qquad -\frac{\mathrm{Re}}{\alpha_k\Delta t}\sum_j \hat{\varphi}_j^{n}\int B_j(y)\,B_i(y)\,\mathrm{d}y - \mathrm{Re}\sum_j (\hat{h}_v)_j^{n+(k-1)/3}\int B_j(y)\cdot B_j(y)\,\mathrm{d}y \\
&\sum_j \hat{v}_j^{n+k/3}(k_x,k_z)\int B_j''(y)\,B_i(y)\,\mathrm{d}y - \left(k_x^2+k_z^2\right)\sum_j \hat{v}_j^{n+k/3}\int B_j(y)\,B_i(y)\,\mathrm{d}y = \\
&\qquad \sum_j \hat{\varphi}_j^{n+k/3}\int B_j(y)\,B_i(y)\,\mathrm{d}y \\
&\sum_j (\hat{\omega}_y)_j^{n+k/3}(k_x,k_z)\int B_j''(y)\,B_i(y)\,\mathrm{d}y - \left(k_x^2+k_z^2+\frac{\mathrm{Re}}{\alpha_k\Delta t}\right)\sum_j (\hat{\omega}_y)_j^{n+k/3}\int B_j(y)\,B_i(y)\,\mathrm{d}y = \\
&\qquad -\frac{\mathrm{Re}}{\alpha_k\Delta t}\sum_j (\hat{\omega}_y)_j^{n}\int B_j(y)\,B_i(y)\,\mathrm{d}y - \mathrm{Re}\sum_j (\hat{h}_g)_j^{n+(k-1)/3}\int B_j(y)\cdot B_j(y)\,\mathrm{d}y
\end{aligned} \tag{19}$$

This system can be formulated more conveniently in matrix-vector notation for each pair of modes (k_x,k_z):

$$\left.\begin{aligned}
\left[\mathbf{K} - (k_x^2+k_z^2+\frac{\mathrm{Re}}{\alpha_k\Delta t})\,\mathbf{M}\right]\cdot\hat{\boldsymbol{\varphi}}^{n+k/3} &= \left[-\frac{\mathrm{Re}}{\alpha_k\Delta t}\mathbf{M}\right]\cdot\hat{\boldsymbol{\varphi}}^{n} - [\mathrm{Re}\,\mathbf{M}]\cdot\hat{\boldsymbol{h}}_v^{n+(k-1)/3} \\
\left[\mathbf{K} - (k_x^2+k_z^2)\,\mathbf{M}\right]\cdot\hat{\boldsymbol{v}}^{n+k/3} &= \mathbf{M}\cdot\hat{\boldsymbol{\varphi}}^{n+(k-1)/3}
\end{aligned}\right\} \tag{20}$$

$$\left[\mathbf{K} - (k_x^2+k_z^2+\frac{\mathrm{Re}}{\alpha_k\Delta t})\,\mathbf{M}\right]\cdot\hat{\boldsymbol{\omega}}_y^{n+k/3} = \left[-\frac{\mathrm{Re}}{\alpha_k\Delta t}\mathbf{M}\right]\cdot\hat{\boldsymbol{\omega}}_y^{n} - [\mathrm{Re}\,\mathbf{M}]\cdot\hat{\boldsymbol{h}}_g^{n+(k-1)/3} \tag{21}$$

The matrices $\mathbf{M}$ and $\mathbf{K}$ are the mass and stiffness matrices respectively, defined by:

$$\begin{aligned}
\mathbf{M}_{ij} &= \int B_j(y)\,B_i(y)\,\mathrm{d}y \\
\mathbf{K}_{ij} &= \int B_j''(y)\,B_i(y)\,\mathrm{d}y = \left[B_j'(y)\,B_i(y)\right]_0^{2h} - \int B_j'(y)\,B_i'(y)\,\mathrm{d}y \quad ,
\end{aligned} \tag{22}$$

which can be precalculated before starting the time integration. The modal equations are thus coupled in the direction y since the involved matrices of size $(N_y \times N_y)$ have a $(2k-1)$-banded structure. An efficient band-matrix solver can be employed for the inversion.

In the case of the constant mode ($k_x = 0, k_z = 0$), the Navier-Stokes equations in primitive variables

$$\partial_t u_i = -\partial_{x_i} p + H_i + \frac{1}{\mathrm{Re}} \nabla^2 u_i \,, \qquad \partial_{x_i} u_i = 0 \quad , \tag{23}$$

can be directly solved for the velocity components since the mean pressure gradient can be deduced from an integral balance across the channel. Let us denote the mean values by capital letters, i.e. $U(y) = u(k_x = 0, y, k_z = 0)$. One obtains for the streamwise gradient

$$\frac{\partial P}{\partial x} = \frac{\nu}{2h} \left[-\partial_y U(y = 0) + \partial_y U(y = 2h) \right] \quad , \tag{24}$$

while the other gradients are zero. Note that in our simulations, the mass flow rate is kept constant such that the wall friction and thus the pressure gradient are functions of time. The discretized equations for the streamwise and spanwise component can be written as follows:

$$\left.\begin{array}{rcl} \left[\mathbf{K} - \dfrac{\mathrm{Re}}{\alpha_k \Delta t} \mathbf{M}\right] \cdot \hat{\boldsymbol{U}}^{n+k/3} & = & \left[-\dfrac{\mathrm{Re}}{\alpha_k \Delta t} \mathbf{M}\right] \cdot \hat{\boldsymbol{U}}^{n} - [\mathrm{Re}\,\mathbf{M}] \cdot \hat{\boldsymbol{H}}_1^{n+(k-1)/3} \\ & & + [\mathrm{Re}\,\mathbf{M}] \cdot (\partial_x P)^{n+(k-1)/3} \\ \left[\mathbf{K} - \dfrac{\mathrm{Re}}{\alpha_k \Delta t} \mathbf{M}\right] \cdot \hat{\boldsymbol{W}}^{n+k/3} & = & \left[-\dfrac{\mathrm{Re}}{\alpha_k \Delta t} \mathbf{M}\right] \cdot \hat{\boldsymbol{W}}^{n} - [\mathrm{Re}\,\mathbf{M}] \cdot \hat{\boldsymbol{H}}_3^{n+(k-1)/3} \end{array}\right\} \tag{25}$$

3.3 Numerical implementation of boundary conditions

The discretized algebraic equations for the independent variables need to be solved subject to the following set of Neumann and Dirichlet boundary conditions – consequence of no-slip (5), impermeability (6), porosity (9) and continuity (3):

$$\left.\begin{array}{ll} \partial_y v(y = 2h) = 0 \,, & \partial_y v(y = 0) = 0 \,, \\ v(y = 2h) = 0 \quad , & v(y = 0) = -\dfrac{\mathrm{Re}}{C_\beta} p'(y = 0) \,, \\ \omega_y(y = 2h) = 0 \;\; , & \omega_y(y = 0) = 0 \,, \end{array}\right\} \tag{26}$$

The set of one-dimensional Helmholtz problems for vorticity ω_y (21) with homogeneous Dirichlet boundary conditions (26) can be solved by a simple condensation method (see appendix B.1).

The problem of solving the bi-Helmholtz problem (20) for velocity v consists in the fact that the four necessary boundary conditions are expressible only in terms of v itself and not φ. One thus has to resort to a linear combination of two solutions to the associated homogeneous problem and a particular solution in order to verify the sum of the boundary conditions exactly. Let us pose

$$\hat{v}^{n+k/3} = \hat{v}_p + c_1 \cdot \hat{v}_{h1} + c_2 \cdot \hat{v}_{h2} \quad , \tag{27}$$

and consequently

$$\hat{\varphi}^{n+k/3} = \hat{\varphi}_p + c_1 \cdot \hat{\varphi}_{h1} + c_2 \cdot \hat{\varphi}_{h2} \quad , \tag{28}$$

where the particular $\{\hat{\varphi}_p, \hat{v}_p\}$ and homogeneous $\{\hat{\varphi}_{h1}, \hat{\varphi}_{h2}, \hat{v}_{h1}, \hat{v}_{h2}\}$ parts are solutions of the following set of Helmholtz problems subject to homogeneous and non-homogeneous Dirichlet conditions:

$$\left.\begin{array}{lcl} \left[\mathbf{K} - (k_x^2 + k_z^2 + \dfrac{\mathrm{Re}}{\alpha_k \Delta t})\,\mathbf{M}\right] \cdot \hat{\varphi}_p & = & \left[-\dfrac{\mathrm{Re}}{\alpha_k \Delta t} \mathbf{M}\right] \cdot \hat{\varphi}^{n} - [\mathrm{Re}\,\mathbf{M}] \cdot \hat{\boldsymbol{h}}_v^{n+(k-1)/3} \\ \left[\mathbf{K} - (k_x^2 + k_z^2)\,\mathbf{M}\right] \cdot \hat{v}_p & = & \mathbf{M} \cdot \hat{\varphi}^{n+(k-1)/3} \\ \underline{\text{with}}: \quad \hat{\varphi}_p(y = 0) = 0 \,, \quad \hat{\varphi}_p(y = 2h) = 0 \,, & & \hat{v}_p(y = 0) = -\frac{\mathrm{Re}}{C_\beta} p' \,, \quad \hat{v}_p(y = 2h) = 0 \end{array}\right\} \tag{29}$$

$$\left.\begin{aligned}
&\left[\mathbf{K}-(k_x^2+k_z^2+\frac{\mathrm{Re}}{\alpha_k\Delta t})\,\mathbf{M}\right]\cdot\hat{\varphi}_{h1} && = \; 0\\
&\left[\mathbf{K}-(k_x^2+k_z^2)\,\mathbf{M}\right]\cdot\hat{\boldsymbol{v}}_{h1} && = \; \mathbf{M}\cdot\hat{\varphi}^{n+(k-1)/3}\\
&\underline{\text{with}}:\quad \hat{\varphi}_{h1}(y\!=\!0)=1\,,\quad \hat{\varphi}_{h1}(y\!=\!2h)=0\,, && \quad\hat{v}_{h1}(y\!=\!0)=0\,,\hat{v}_{h1}(y\!=\!2h)=0
\end{aligned}\right\}\tag{30}$$

$$\left.\begin{aligned}
\hat{\varphi}_{h2}(y) &= \hat{\varphi}_{h1}(2h-y)\\
\hat{\boldsymbol{v}}_{h2}(y) &= \hat{\boldsymbol{v}}_{h1}(2h-y)
\end{aligned}\right\}\tag{31}$$

The constant coefficients are determined such that the homogeneous Neumann condition on v is satisfied on both walls by the final solution, i.e. c_1 and c_2 are obtained via the following linear system:

$$\left.\begin{aligned}
0 &= \partial_y\,\hat{v}_p(y\!=\!0)+c_1\cdot\partial_y\,\hat{v}_{h1}(y\!=\!0)+c_2\cdot\partial_y\,\hat{v}_{h2}(y\!=\!0)\\
0 &= \partial_y\,\hat{v}_p(y\!=\!2h)+c_1\cdot\partial_y\,\hat{v}_{h1}(y\!=\!2h)+c_2\cdot\partial_y\,\hat{v}_{h2}(y\!=\!2h)
\end{aligned}\right\}\tag{32}$$

The final solution $\{\hat{v}^{n+k/3},\hat{\varphi}^{n+k/3}\}$ can then be calculated from relations (27) and (28).

The following remarks can be made about the above outlined solution procedure for the bi-Helmholtz problem:

- The method is of sixth order formal accuracy which has been verified on a variety of analytical functions.

- Since the problem is geometrically symmetric, the second homogeneous solution, with $\{\hat{\varphi}_{h2}(y\!=\!0)=1,\hat{\varphi}_{h2}(y\!=\!2h)=0\}$, is antisymmetric to the previous one with respect to the centerline of the channel. As indicated in (31), its computation can thus be spared.

- The Dirichlet boundary conditions are satisfied within machine accuracy. The compatibility of the Neumann condition with the collocation approach is ensured since the derivations in (32) are carried out by the formula (13) such that the final solution obeys this Neumann condition numerically (in the collocation sense) up to machine accuracy.

- The solutions to the one-dimensional homogeneous Helmholtz problem can be obtained analytically (see appendix B.2). However, the involved exponential functions lead to numerical overflow in practical computations such that the fully numerical approach (29)-(32) is preferred.

- Another alternative would be the computation of the above particular and homogeneous solutions with homogeneous Neumann boundary conditions for v (no condensation would be performed in that case, see appendix B.1) and subsequent imposition of the Dirichlet conditions by the following linear combination:

  $$\left.\begin{aligned}
  0 &= \hat{v}_p(y\!=\!0)+c_1\cdot\hat{v}_{h1}(y\!=\!0)+c_2\cdot\hat{v}_{h2}(y\!=\!0)\\
  -\frac{\mathrm{Re}}{C_\beta}\,p' &= \hat{v}_p(y\!=\!2h)+c_1\cdot\hat{v}_{h1}(y\!=\!2h)+c_2\cdot\hat{v}_{h2}(y\!=\!2h)
  \end{aligned}\right\}\tag{33}$$

  In a pure Galerkin approach this possibility might be preferable since the end-point derivatives do not have to be calculated explicitly. In our case, however, this method does not ensure satisfaction of Neumann conditions in the sense of the collocation derivatives (i.e. applying formula (32) to the solution would not yield machine zero at the end-points).

3.3.1 Determination of pressure fluctuations and the numerical transpiration velocity

The elliptic equation for pressure is obtained by taking the divergence of the momentum equation (23),

$$\nabla^2 p = \partial_{x_i} H_i \quad , \tag{34}$$

which can be solved by a similar routine as used for vorticity ω_y while taking advantage of the fact that the advection terms H_i of the right hand side have already been computed. However, boundary conditions are needed to accompany (34) and some care has to be taken as to ensure stability of the overall computation, since pressure in turn provides part of the boundary condition for the kinematic variables.

The wall-normal momentum equation written at the lower wall reads:

$$\partial_t v + \underbrace{v \cdot \partial_y v}_{\substack{=0 \\ \text{(continuity)}}} + \underbrace{u \cdot \partial_x v + w \cdot \partial_z v}_{\substack{=0 \\ \text{(no-slip)}}} + \partial_y p = \frac{\varphi}{\mathrm{Re}} \quad . \tag{35}$$

Eliminating velocity by the porosity relation (9) and using a first order approximation to the time derivative leads to:

$$-\frac{\mathrm{Re}}{C_\beta \, \alpha_k \Delta t} \left(p^{n+k/3} - p^{n+(k-1)/3} \right) + \partial_y p = \frac{\varphi}{\mathrm{Re}} \quad . \tag{36}$$

For stability, the spatial derivative of pressure needs to be discretized implicitly, while the rhs is taken at the previous time level, thus:

$$\partial_y p^{n+k/3} - \frac{\mathrm{Re}}{C_\beta \, \alpha_k \Delta t} p^{n+k/3} = \frac{\varphi^{n+(k-1)/3}}{\mathrm{Re}} - \frac{\mathrm{Re}}{C_\beta \, \alpha_k \Delta t} p^{n+(k-1)/3} \qquad (y=0) \, , \tag{37}$$

which constitutes a mixed Neumann-Dirichlet (Robin) boundary condition. At the same time, we simply have on the top wall:

$$\partial_y p^{n+k/3} = \frac{\varphi^{n+(k-1)/3}}{\mathrm{Re}} \qquad (y=2h) \, . \tag{38}$$

Imposing the above conditions necessitates again a superposition of particular and homogeneous solutions according to:

$$p^{n+k/3} = p_p + c_1 \cdot p_{h1} + c_2 \cdot p_{h2} \quad , \tag{39}$$

where the respective contributions are obtained from the solution of the following Helmholtz problems:

$$\left. \begin{aligned} \left[\mathbf{K} - (k_x^2 + k_z^2) \mathbf{M} \right] \cdot \hat{\boldsymbol{p}}_p \quad &= \quad -\mathbf{M} \cdot (\widehat{\partial_{x_i} \boldsymbol{H}})_i^{n+(k-1)/3} \\ \underline{\text{with}}: \quad \hat{p}_p(y=0) = 0 \, , \qquad &\hat{p}_p(y=2h) = 0 \end{aligned} \right\} \tag{40}$$

$$\left. \begin{aligned} \left[\mathbf{K} - (k_x^2 + k_z^2) \mathbf{M} \right] \cdot \hat{\boldsymbol{p}}_{h1} \quad &= \quad 0 \\ \underline{\text{with}}: \quad \hat{p}_{h1}(y=0) = 1 \, , \qquad &\hat{p}_{h1}(y=2h) = 0 \end{aligned} \right\} \tag{41}$$

$$\left. \hat{\boldsymbol{p}}_{h2}(y) \quad = \quad \hat{\boldsymbol{p}}_{h1}(2h - y) \quad \right\} \tag{42}$$

The following linear system then defines the coefficients c_1, c_2:

$$\left.\begin{aligned}
&\partial_y \hat{p}_p(y=0) + c_1 \cdot \partial_y \hat{p}_{h1}(y=0) + c_2 \cdot \partial_y \hat{p}_{h2}(y=0) \\
&-\frac{\mathrm{Re}}{C_\beta \Delta t \alpha_k}\left(\underbrace{\hat{p}_p(y=0)}_{=0} + c_1 \cdot \hat{p}_{h1}(y=0) + c_2 \cdot \hat{p}_{h2}(y=0)\right) \quad = \\
&\qquad\qquad\qquad\qquad \frac{\hat{\varphi}^{n+(k-1)/3}(y=0)}{\mathrm{Re}} - \frac{\mathrm{Re}}{C_\beta\, \alpha_k \Delta t}\, \hat{p}^{n+(k-1)/3}(y=0) \\
&\partial_y \hat{p}_p(y=2h) + c_1 \cdot \partial_y \hat{p}_{h1}(y=2h) + c_2 \cdot \partial_y \hat{p}_{h2}(y=2h) \quad = \quad \frac{\hat{\varphi}^{n+(k-1)/3}(y=2h)}{\mathrm{Re}}
\end{aligned}\right\} \tag{43}$$

which let us obtain the actual pressure field via (39). Note that this pressure does not include the mean pressure which is varying linearly in the streamwise direction.

Once the pressure fluctuations at the actual time level $(n + k/3)$ have been calculated, these can be used as the lower wall boundary condition for the velocity calculation, i.e. $\hat{v}^{n+k/3}(0) = -\mathrm{Re}/C_\beta\, \hat{p}^{n+k/3}(0)$. We remark that this numerical implementation is consistent with both limits of Darcy's law:

- impermeable case:

$$\lim_{C_\beta \to \infty} (v^{n+k/3}(0)) = 0\,, \qquad \lim_{C_\beta \to \infty} (\partial_y p^{n+k/3}(0)) = \frac{\phi^{n+(k-1)/3}}{\mathrm{Re}}\,.$$

- perfectly permeable case:

$$\lim_{C_\beta \to 0} (p^{n+k/3}(0)) = p^{n+(k-1)/3}(0)\,, \qquad \lim_{C_\beta \to 0} (v^{n+k/3}(0)) = v^{n+(k-1)/3}(0)\,.$$

4 Results

4.1 Physical parameters of the simulations

Reynolds number. The Reynolds number of the present simulations – based on channel half width h and maximum mean velocity U_0 – takes a value of $\mathrm{Re} = 3250$, comparable to the study of Kim *et al.* [19]. This value leads to a friction-velocity-based Reynolds number $\mathrm{Re}_\tau \approx 180$ in the case of a channel with impermeable walls. Since our simulations are performed at constant mass flux, the bulk velocity $U_b = \int_0^{2h} u\mathrm{d}y/(2h)$ is actually the characteristic outer flow velocity. However, U_0 varies little (cf. table 1) and we will continue using it as a scale.

Dimension. For the initial runs *case 8* and *case 11* the box size had been chosen as $L_x = 2.69h$ and $L_z = 1.59h$ (table 1), corresponding to roughly 530 and 320 wall units respectively. This extent is about three times the size of the minimal flow unit (MFU) at this Reynolds number in spanwise direction and only slightly larger than the MFU in streamwise direction [16]. Although being sufficiently large to sustain turbulence at the chosen Reynolds number, the velocities are not uncorrelated within the box, especially in the streamwise direction. In order to obtain meaningful two-point auto-correlations we performed subsequent computations (*cases 15* and *16*) using a much larger box of size $L_x = 2.6\pi h$ and $L_z = \pi h$ (approximately an extent of 1700 and 670 wall units respectively).

Porosity. The presence of a porous wall has two direct consequences for the numerical simulation of a turbulent flow: (i) non-zero wall-normal velocities create a severe restriction on the allowable time step since the computational grid is fine near the boundary; (ii) as seen below, small scales are created by the action of the porous wall, increasing the spatial resolution requirement. As a consequence of these two facts, simulations become increasingly expensive in terms of storage and computational effort as porosity is increased, i.e. for lower values of C_β. Obviously the choice of the porosity parameter is in practice limited by the available facilities. In the present study we have focused on the pair of values $C_\beta = \{5000, 4000\}$. At this level of porosity, the *rms* value of the transpiration velocity is of the order of one tenth of the friction velocity u_τ and the effect on wall shear is appreciable. Important changes in the flow structure have been observed. Moreover, an accompanying linear stability analysis indicates that the chosen porosity values belong to the unstable regime [15].

4.2 Numerical parameters

Resolution. The number of Fourier modes and b-splines used in the different runs are shown in table 1, reaching up to $256 \times 192 \times 192$ for *case 15* and *16*. Also included in the table are the stream- and spanwise "grid" spacing in wall units based on the porous wall shear velocity. As mentioned above, the resolution had to be increased substantially at the higher value of porosity.

In the wall-normal direction, where hyperbolic tangent stretching is employed (appendix A.1.6), the first grid point is situated at $y^+ = 0.24$ ($y^+ = 0.2$ in *case 15 & 16*) and the maximum spacing at the centerline of the channel attains 2.6 wall units (2.2 respectively). The one-dimensional energy spectra discussed below (section 4.5) indicate the adequacy of this resolution, at least in the wall-parallel directions.

Also included in table 1 are the details of a reference calculation using a fully spectral (Fourier-Chebychev) method [17] with impermeable walls. That data will be used in the following for the purpose of comparison.

Time step. The time step is globally adjusted such that the maximum advection CFL number does not exceed 0.5. This criterion leads to an average time step as low as $\Delta t\, U_0/h \approx 2 \cdot 10^{-3}$ in

run	L_x/h	L_z/h	N_x	N_y	N_z	Δx^+	Δz^+	Δy^+_{min}	Δy^+_{max}	$\Delta t U_0/h$	C_β	U_0/U_b
case $1^\dagger$	9.42	3.14	192	97	128	8.8	4.4	.10	6.0	1e-2	∞	1.19
case 8	2.69	1.59	48	160	64	17.5	7.7	.24	2.6	4.5e-3	5000	1.15
case 11	2.69	1.59	128	160	96	6.5	5.2	.24	2.6	4e-3	4000	1.17
case 15	8.17	3.14	256	192	192	9.6	5.0	.20	2.2	2e-3	4000	1.17
case 16	8.17	3.14	256	192	192	9.6	5.0	.20	2.2	6e-3	∞	1.16

Table 1: Parameters of the different runs realized, concerning the box size, the resolution, average time step, the Darcy coefficient of porosity and maximum mean streamwise velocity. The stream- and spanwise grid spacing corresponds to the number of modes after dealiasing. The reference case $1^\dagger$ has been realized using Chebychev polynomials in the wall-normal direction [17].

run *15*.

Initial fields. In cases *8,11,15,16* instantaneous equilibrium flow fields from a fully spectral simulation [17] of channel flow over impermeable walls have been used as the initial conditions. Due to the different types of spatial approximations of the flow variables and the initial interpolation between the two distinct grids, artificial perturbations are introduced. The procedure involves an initial Chebychev-to-spline interpolation and a fill-up (with a value of zero) of high-wavenumber Fourier modes. Moreover, switching-on wall porosity at a given time in cases *8,11,15* gives rise to further transient behavior. We have taken special care as to allow for a sufficient relaxation period before accumulating the statistical quantities. For *case 15* this transient is shown in figure 4 in terms of the time evolution of wall friction. First the flow relaxes from the spatial interpolation during approximately 22 outer flow time units ($t\,U_0/h$). Then we turn on the porosity of the lower wall and let the flow develop its characteristic discrepancy in wall friction between the two walls (see discussion below, §4.3) during 30 time units. Note that the wall friction curve corresponding to the top wall exhibits several kinks during the transient phase. These correspond to a numerical artifact that we have eliminated hereafter: when restarting a run from a previous calculation, the first Runge-Kutta sub-step of the new run was originally performed using the impermeability condition on both walls because pressure values of the previous time step had not been stored along with (ϕ, ω_y)-data.

4.3 Wall shear stress evolution

The mean (i.e. (x,z)-plane averaged) spanwise vorticity component in the wall plane is directly linked to the wall shear stress, $\tau_w = \nu\,\overline{\omega}_z(y_w)$. Figures 5 to 7 show the temporal evolution of $\overline{\omega}_z(y_w)\,h/U_0 = \mathrm{Re}\cdot c_f/2$ over several hundred core flow time units, opposing both walls. It can be seen that in simulations involving one porous wall the shear rate is substantially higher on average on the porous surface than it is on the opposite (impermeable) wall. The difference in wall friction between both walls amounts to 12% in case 8 and to 32.5% in case 15. Note that this difference only measures 25% in *case 11* although the level of porosity has the same value as in *case 15*. This fact indicates that the size of the computational domain matters when determining the drag increase for a given porosity. We will further address this point in §5.

Instantaneously, the hierarchy between the two wall stresses can be reversed since the (x-z)-plane averaged values are affected by individual events that take place in the finite box. In fact, cyclic variations of the wall shear evolution around the temporal mean value can be observed, being visibly of shorter period on the porous wall. This is true even when time is expressed in both cases in local wall units $t\,u_\tau^2/\nu$. Because of the larger instantaneous sample, respective curves of *case 15* and *16* are substantially smoother. When comparing statistical quantities we will in the following concentrate on these two cases.

The finding of an increase in wall friction when the impermeability constraint is relaxed is consistent with the results of Wagner and Friedrich [34] of direct simulation of turbulent flow in pipes with perfectly permeable walls. In their simulations, a sixfold increase in wall friction was noted at a bulk Reynolds number (based on pipe diameter and bulk velocity) of 5500. Partial permeability – which was implemented by a boundary condition not involving pressure – also leads to a noticeable rise in wall friction in their work. It thus seems that the degree of permeability of a boundary has a strong amplifying influence on the turbulence activity of the adjacent flow. Previously, the mechanism by which this is achieved had not yet been fully understood. Here we will attempt to elucidate the situation further by discussing the details of the changes that take place in the near-wall structure of the flow over a porous wall with the aid of one- and two-point statistics.

4.4 Wall-normal profiles of various one-point statistical quantities

Tangential stress. Figure 8 shows profiles of the total tangential stress $\tau_{xy} = \nu\partial_y(U) - \overline{u'v'}$. The linearity of the curves indicates that the second order statistics have converged sufficiently since one can see from a stress-balance of a cross section that the stress varies linearly with wall-distance at equilibrium. The fact that the zeroes of the total stress are above the centerline $y = h$ in the case of one porous wall demonstrates the non-symmetric character of the problem.

Mean velocity. The obtained velocity profiles in global coordinates are shown in figure 9. Porosity of the lower wall is seen to progressively shift the maximum of the profiles towards the top wall due to the difference in wall friction. More fluid passes through the upper half of the channel adjacent to the (relative) low-drag wall.

Plotted in wall coordinates, the velocity distributions of all cases are found to follow a logarithmic law with $\kappa = .4$ over the range of $y^+ \approx 30 \dots 150$. However, the intercept decreases with the level of porosity which is a direct consequence of the corresponding differences in wall friction values observed above.

Velocity fluctuations. Figure 10 shows profiles of turbulent kinetic energy (TKE). When normalized with the maximum kinetic energy of the mean flow, this quantity is increased slightly across the whole section in the case of one porous wall, taking particularly high levels near that lower wall. Relative to the energy of the friction velocity, porosity only increases the TKE very close to the wall ($y^+ < 12$) and towards the centerline ($y^+ > 40$). The fact that the increase in turbulence intensity does not scale with u_τ indicates that the dynamics of the flow in the wall region changes somehow due to porosity.

Figure 11 shows *rms* values of the individual components of fluctuating velocity in wall units. In an intermediate region, i.e. $10 < y^+ < 60$, the streamwise fluctuations are reduced near a porous wall and increased elsewhere. At the meantime, the wall-normal and spanwise components are increased over the whole section. Let us further stress this point by considering the components of the tensor of anisotropy of the Reynolds stress $b_{ij} = \overline{u'_i u'_j}/\overline{u'_k u'_k} - \delta_{ij}/3$ (figure 12). It can be seen that the anisotropy of the normal components is reduced in the porous case except for the viscous sublayer, where the tensor approaches the state of one-dimensional turbulence in the wall-normal direction which corresponds to $b_{11} = b_{33} = -1/3$, $b_{22} = 2/3$ and $b_{12} = 0$ (note that b_{ij} is not defined at the wall $y = 0$ in the impermeable case). Reduced anisotropy signifies a reduction of the intercomponental energy transfer from the wall-normal to the wall-parallel motion that usually takes place when approaching a solid boundary. The tangential anisotropy b_{12} increases towards the porous wall showing that the turbulent stress is enhanced proportionally more than the turbulence intensity.

Vorticity fluctuations. The fluctuations of all the components of the vorticity are higher in the channel half adjacent to the porous wall when normalized with maximum mean flow velocity and channel half width (not shown). In the following we will consider vorticity expressed in wall units, i.e. $\omega_i'^+ = \omega_i' \nu / u_\tau^2$.

The *rms* values of streamwise vorticity $\omega_x'^+$are found to be enhanced near the porous wall up to the center of the channel (figure 13). Moreover, the location of the second maximum y_c^+ of this quantity is situated several wall units closer to the wall in *case 15* as compared to the impermeable reference case ($y_c^+ = 19$ as compared to $y_c^+ = 22.5$). Since this maximum is commonly associated with the average location of streamwise vortical structures [19], our result implies that porosity allows those vortices to approach the boundary more closely in the mean than an impermeable wall and that the vortices have a higher intensity in wall units.

Wall-normal vorticity $\omega_y'^+$ (figure 14), on the other hand, is found to be reduced near a porous wall – especially around the location of its maximum ($y^+ \approx 15 \ldots 20$). Since ω_y is a good (indirect) measure of the intensity of high- and low-velocity streaks, we conclude that streaks are *relatively* weak near a porous wall. We need to discuss these observations in the light of the regeneration cycle of turbulence (see e.g. [8, 31, 17]). Both mentioned types of coherent structures – streamwise vortices and streaks – are intimitely linked to the sustenance of near-wall turbulence: the vortices generate streaks by advection in the presence of mean wall-normal shear while the streaks give rise to new vortices through an instability mechanism. If one accepts the friction velocity u_τ as the significant scale for this cycle then the above observation of opposite effects of porosity on $\omega_x'^+$ (vortices) and $\omega_y'^+$ (streaks) implies that we actually see a new mechanism at work. If the turbulence cycle were simply accelerated, the contrary reaction of $\omega_x'^+$ and $\omega_y'^+$ to wall-porosity would probably not be observed.

The spanwise vorticity fluctuations $\omega_z'^+$ (figure 15) are lower in the porous case except in the viscous sublayer, where, on the contrary, a large increase is noted. Above all, the wall is approached with a large gradient, whereas $\partial(\omega_z)/\partial y$ is nearly zero at an impermeable wall.

Let us now examine the formation of streaks from streamwise vortices. This process corresponds to the lifting of low-speed fluid (downwash of high-speed fluid) through the wall-normal velocity field of a streamwise vortex. In other words, the advection term $v' \partial U / \partial y$ creates streamwise velocity fluctuations u'. Figure 16 shows profiles of wall-normal velocity fluctuations v' normalized by the vortex intensity ω_{x_c} and location y_c corresponding to the second maximum of figure 13. The ratio $v'/(\omega_{x_c} y_c)$ can be understood as a measure of the wall-normal vorticity that is induced by a streamwise vortex of given location and strength. It can be seen that this quantity is considerably higher near a porous wall than it is in the impermeable case. A qualitative explanation of the effect can be obtained by considering the potential flow induced by a point vortex above the two types of walls (see appendix D). In the approximation of small porosity it is found that the Darcy condition (9) corresponds to an additional (complex) potential that leads to an increase in the *rms* value of induced wall-normal velocity.

Higher induced v' leads to an increased streak intensity which corresponds to a "boost" in turbulence activity. This is the first part of the effects that porosity exerces upon the adjacent flow. However, as mentioned before, we expect a new mechanism to interfere with the basic wall cycle. This point will become more clear in §4.6-4.8.

4.5 One-dimensional energy spectra

Energy spectra of velocity and pressure in the two periodic directions are shown in figures 17 and 18 (large box of *cases 15* and *16*). These spectra indicate that in the respective runs the flow field was indeed adequately resolved since the energy density is dropping off over several decades at high wavenumbers.

The comparison between corresponding spectra near the porous wall and the impermeable wall shows the creation of smaller scales by the action of the wall transpiration. At a given (normalized) energy density, the associated wavenumber is visibly higher in the case of the porous wall. This observation is valid for all velocity components and pressure. However, the phenomenon of length scale reduction is more pronounced in the streamwise direction than in the spanwise direction.

4.6 Two-point autocorrelations

The above statistical information on the energy spectra can be used to compute two-point autocorrelations of the fluctuations of velocity and pressure (see appendix C).

In order to evaluate the sufficiency of the dimensions of our domain of integration, we consider two-point correlations of the completely impermeable *case 16* close to the wall and near the center of the channel (figures 19 and 20). The signals are decorrelated for separations of one half of the domain size in both stream- and spanwise directions except for pressure and streamwise velocity which maintain non-negligible correlation values at the largest spanwise separation near the centerline ($y^+ = 143$). The present decorrelation is of similar quality as that of previous studies, e.g. Kim *et al.* [19] and Kim [18]. Note that large streamwise structures of the order of 10 boundary layer thicknesses exist in the logarithmic region of wall-bounded flows [13, 20], which are not captured by the limited domain of most current and previous numerical simulations.

Figure 21 shows autocorrelations of streamwise velocity for spanwise separations. Above the impermeable wall of *case 15*, curves behave like in the fully impermeable *case 16* (not shown), rapidly dropping to negative values and then levelling off towards zero at distances greater than about 200 wall units. Near the porous wall, however, high positive spanwise correlations persist across the whole domain. Here the value of the "plateau", i.e. R_{uu} at high z^+, decreases with increasing wall-distance. This decrease of the spanwise correlation R_{uu} can be observed in figure 22 where the spanwise averages of the respective curves of figure 21 are shown as a function of wall-distance. At $y^+ = 100$ this high correlation has dropped to a value similar to that of the fully impermeable case. The above result clearly indicates a spanwise organization of the flow due to wall-porosity. To a lesser extent a corresponding spanwise organization is also found to hold for the wall-normal velocity as can be seen in figure 23 where again the mean spanwise correlation is plotted. The spanwise velocity, however, does not exhibit any unusually high spanwise correlations (figure 24).

Koumoutsakos [21] reported a strong spanwise organization of turbulent channel flow fluctuations when applying active drag-reduction control at the boundary. In his case – which is distinct because a discrete array of actuators was simulated and vorticity flux was the control quantity – alternating roller-like structures were formed.

Let us further examine autocorrelations of pressure (figure 25). For large spanwise separations, unusually high positive values ($\approx 0.3 \ldots 0.5$) are recorded near *both* walls of *case 15*. Pressure, obeying an elliptic equation, is visibly affected by the porosity of the lower wall throughout the whole domain. In the streamwise direction, instead of the usual rapid decorrelation, pressure signals are anti-correlated for separations greater than about 400 wall units near *both* walls of *case 15*. The maximum anti-correlation is attained at a separation of half the domain length. High positive spanwise correlations and high negative streamwise correlations at large separations are indeed indications of large coherent alternating structures.

Pure "rollers" correspond to motion in the (x, y)-plane. We will collect further evidence of their existence by extracting the mode that is constant in the spanwise direction ($k_z = 0$) from the complete fluctuation data. Figure 26 demonstrates for the wall-normal velocity at $y^+ = 70$ that – while the full fluctuation data shows no unusual behaviour – its two-dimensional mode exhibits an anti-correlation very similar to that of pressure. The anti-correlated behaviour of the two-dimensional mode of *case 15* is very distinct from that of the impermeable *case 16* where – as can be seen in figure 27 – a rapid decorrelation is obtained for $x^+ \geq 100$. Again a similar, yet much stronger, negative correlation of two-dimensional mode fluctuations of streamwise velocity is observed in *case 15* (figure 28). Contrarily, the spanwise velocity exhibits a rapid streamwise decorrelation (separations above 100 wall units) in *both* cases.

All the above facts are consistent with the existence of large-scale, spanwise-coherent, roller-like structures in the flow over a porous wall. However, we cannot offer a strict proof that these structures are indeed what we have called "rollers". In the following sections we will identify these structures in visualizations of instantaneous flow fields as well as attempt to measure and describe their impact on the regeneration cycle of turbulence.

To conclude this section, we consider the impact of porosity on the spanwise spacing of streaks. The minimum of $R_{uu}(z)$ corresponds to about one half of the average spanwise spacing between high- and low-speed streaks [19] (figure 30). Near an impermeable wall (*case 16*) streaks are separated by about 100 wall units. Above the porous wall of *case 15*, streak spacing is found to increase to a value of approximately 150 (using *local* wall units in all cases), while the value near the opposite wall is only slightly increased. In pipe flow at comparable Reynolds number, Wagner and Friedrich [34] found that perfect permeability of the wall causes a doubling of the usual streak spacing. However, these authors did not give an explanation for the increase in streak spacing due to wall-permeability. We will further discuss this point in §4.8.

4.7 Visualization of instantaneous structural related quantities

Structure of the streaks. We now consider visualizations of the wall-normal vorticity fluctuations $\omega_y'^+$ at individual instants of simulations *15* and *16* (large box, see figures 31-32). These frames are representative of the general flow evolution.

In the buffer layer of the impermeable wall of *case 16*, the isosurfaces of ω_y' behave according to the observations of previous authors [17]. They form elongated structures which are nearly parallel to the mean flow direction x and have a large streamwise coherence. Typically, five pairs of negative- and positive-valued structures, i.e. five high- and five low-speed streaks, are found adjacent to each other across the spanwise extent of the current box. One can also distinguish a spanwise, sine-like waviness of the isosurfaces whose streamwise wavelength measures several hundred wall units.

Considering the bottom half of the channel which borders on the porous wall (*case 15*), we still encounter streaky structures similar to the ones mentioned previously. However, regions of "normal" activity are interrupted by intervals where we find more disordered structures (e.g. $600 < x^+ < 800$ in figure 31) and by zones where the flow is more quiescent (x^+ around 1500 in figure 31). These "intermittent" zones extend across the whole width of the domain. We can conjecture that the spanwise-coherent, roller-like structures are responsible for the observed phenomenon. The mechanism by which "rollers" affect the streaks will be examined in more detail in section §4.8.

In the present framework, stability analysis can be a useful tool. A linear stability analysis of a three-dimensional base flow including a model for streaks has been performed [15, part II]. It was found that porosity does not affect the basic *sinous* streak instability in the range of parameters typical for experiments. On the other hand, wall porosity does destabilize *varicose* type perturbations which are usually stable. The eigenfunctions of the most unstable modes have indeed the shape of nearly two-dimensional "rollers". The calculations in [15, part II] indicate that both values of porosity chosen in the present simulation ($C_\beta = \{4000, 5000\}$ at the current Reynolds number) are supercritical. A detailed comparison of DNS data with results from linear stability analysis is not the subject of the present report and will be presented elsewhere.

Wall pressure contours. The zero-valued contours of pressure fluctuations in the wall planes of several instantaneous flow fields are shown in figures 33 to 35. Again spanwise coherent patterns are visible on the porous wall of *case 15* and also on the opposite, impermeable wall of *case 15.* These patterns correspond to the traces of the large scale alternating "rollers". In *case 16* the contours have an irregular shape with no sign of such spanwise coherence.

Two-dimensional motion in the (x, y)-plane. We have extracted the two-dimensional ($k_z = 0$) mode of the fluctuations of several instantaneous "snapshots" of our simulations. Figure 36 shows the stream function Ψ (where $\Psi_{,x} = v'_{2D}$ and $\Psi_{,y} = -u'_{2D}$) calculated with the two-dimensional data of *case 15*. Large coherent motion in the (x, y)-plane is indeed observed, having roughly the shape of alternating "rollers" biased towards the bottom (porous) wall. Their wavelength – estimated according to the "eyeball norm" – measures about the length of the computational box, i.e. $8h$. Visualizations of "snapshots" of *case 16* (not shown) do not reveal such structures.

Contour lines of pressure fluctuations of the (x, y)-mode at instants corresponding to the previous data are shown in figure 37. Again large zones of similar values are visible. It can be observed that – while higher gradients exist near the porous wall – the coherence of these zones extends up to the opposite (impermeable) wall. For this reason two-point correlations are affected by porosity on *both* sides of the channel (cf. §4.6).

4.8 Effects of spanwise-oriented "rollers"

Intensity of "rollers". In the previous sections (§4.6-4.7) large-scale, spanwise-oriented, roller-like coherent structures have been identified in the case of a porous wall through two-point correlations and selected "snapshots" of the flow. We have also mentioned that the origin of those structures has been found to be a quasi-two-dimensional instability of the mean flow profile. At this point we would like to know the intensity of the two-dimensional motion in the (x, y)-plane. In figure 38 we have plotted the kinetic energy contained in that motion as a function of wall distance. When this quantity is normalized with mean flow kinetic energy, a concentration very close to the porous wall is observed. Furthermore, a very large amplification with respect to the impermeable case can be noted throughout the channel. Relative to the total turbulent kinetic energy (TKE) the two-dimensional fluctuation energy has a second local maximum in the center of the channel because TKE has a minimum there. The two-dimensional contribution to TKE reaches up to 30% in *case 15*. Note that the concentration of two-dimensional energy near the porous wall is not contradictory to the extent of large structures across the whole channel height (cf. §4.7). Figure 39 shows the kinetic energy corresponding to the flowfield of figures 36(e) and 37(e) and high values are clearly limited to a zone close to the lower wall. The two-dimensional contribution to the *rms* value of the fluctuations of each velocity component is shown in figure 40. Only the profiles of the streamwise and the wall-normal velocity component are significantly increased by porosity. The two-dimensional part of spanwise velocity is nearly unchanged. The motion in the (x, y)-plane ("rollers") does contribute to the mentioned increase of the *rms* intensity of wall-normal velocity fluctuations in the porous case (cf. §4.4 and figure 16). However, the two-dimensional contribution only accounts for a (small) part of this phenomenon (cf. figure 55 for the curves not including this contribution) and the previous argument involving our point vortex model remains valid.

Streak extinction. Now that we have established quantitatively the high intensity of spanwise-oriented structures near a porous wall, we will discuss their impact on the turbulence regeneration cycle. Since streaks have a large streamwise coherence (approximately 1000 wall units [14]) and an orientation perpendicular to the axis of the roller-like vortices, one can imagine that some type of interference takes place. As shown schematically in figure 2, we expect the rollers to affect the streaks by their vertical motion. In order to verify this hypothesis we consider the joint probability density (JPD) of the following two variables:

(i) two-dimensional mode of the wall-normal velocity fluctuations

$$v'_{2D}(x, y, t) = \sum_{k=1}^{n_z} v(x, y, z_k, t)/n_z \qquad (44)$$

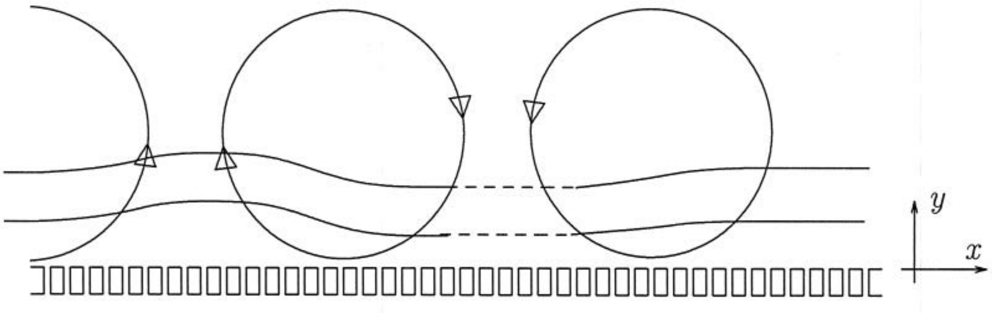

Figure 2: Schematic of the interference between streamwise orientated velocity streaks and spanwise-orientated roller-like structures near a porous wall.

⟶ a measure of the vertical motion of the "rollers";

(ii) spanwise standard deviation of streamwise velocity

$$\sigma_z(u) = \left(\sum_{k=1}^{n_z} (u(x,y,z,t) - \overline{u}(x,y,t))^2 / n_z \right)^{1/2} \tag{45}$$

⟶ a measure of streak intensity across the span.

Histograms of the JPD have been accumulated over 10 (6) instantaneous decorrelated flow fields for *case 15* (*case 16*). Figure 41 shows contour lines of these histograms as well as a least-squares fit of a straight line with each dataset (linear regression) at a wall-distance of the order of the mean streamwise vortex height ($20 \le y^+ \le 30$). In the fully impermeable *case 16* the JPD is approximately symmetric with respect to the horizontal axis. Moreover, low or high streak intensity does not correlate with high absolute values of wall-normal velocity. In *case 15*, on the other hand, the linear regression is tilted by about 12°. Low streak intensity is found to correlate with negative v'_{2D}. In other words, down-wash events cut the streaks. High streak intensity, on the contrary, does not correlate with either positive or negative wall-normal fluctuations in *case 15*. This means that streaks are strongest when the rollers are not present or when they are not inducing wall-normal velocities. At the same time, the strongest positive and negative wall-normal velocities correlate with medium streak intensities.

Streamwise streak coherence. As a consequence of the described "cut-off" effect, streaks are expected to be of shorter streamwise extent in the mean. We have already observed this feature in instantaneous visualizations of ω'_y (cf. §4.7). Let us now check it quantitatively. Since the presence of the "rollers" perturbs the streamwise autocorrelations (cf. §4.7), we consider two-point correlations of the modes of streamwise velocity for which the spanwise wavenumber is strictly positive ($k_z > 0$). This excludes two-dimensional motion in the (x, y)-plane. Figure 42 shows only a slight reduction of the correlation coefficient for large separations above the porous wall and a more clear reduction for wall-distances greater than 70 wall units.

Streak height. Let us address the question whether the streak height is influenced by the cut-off events. We have accumulated histograms of the JPD between

(i) the wall-normal *rms* value of the spanwise standard deviation of streamwise velocity (45),

$$\overline{(\sigma_z(u))}_y = \left(\frac{1}{y_l} \int_0^{y_l} (\sigma_z(u))^2 \mathrm{d}y \right)^{1/2} \tag{46}$$

⟶ an integral measure of streak intensity in the wall region $0 \le y \le y_l$.

(ii) the wall-normal distance of the maximum of the spanwise averaged streak intensity:

$$y_m \qquad / \qquad \sigma_z(u)(x, y_m) = \max_{i=1}^{n_y} \left(\sigma_z(u)(x, y_i)\right) \tag{47}$$

⟶ a measure of streak height.

The upper limit of the integration y_l has been set to 50 wall units. The flow fields used for the statistics are identical to those of the previous JPD. The histograms in figure 43 – although being noisy – show above all that the streak height varies much more in the porous *case 15* than than in the impermeable *case 16* (the standard deviation of y_m measures 8.6 and 4.9 respectively). Moreover, low streak intensity $\overline{\sigma_z(u)}_y$ effectively correlates with low streak height in *case 15* only. We can conclude from the data that what we have previously called a “cut-off” event corresponds to “rollers” squashing streaks against the wall where they lose intensity because of viscosity.

Influence on friction. Figure 44 shows spanwise-averaged skin friction as a function of x at a particular instant of simulation *15*. Also shown is the corresponding streamfunction of the $k_z = 0$ modes of the fluctuating velocity. It is observed that below the large counterclockwise rotating structure an important increase in wall friction occurs (more than twice the box-average value). On the other hand, below the clockwise rotating structure in the center of the domain the flow is driven close to separation (in fact, in very localized regions an instantaneous flow reversal has been observed).

The streak/roller cycle. The observations made in this section lead to the following picture of the interaction mechanism. Large-scale, spanwise-coherent, alternating vortices successively induce upward- and downward-directed motion in the wall-layer above the porous wall. In the down-wash region, streaks are squashed against the wall, i.e. weakened or extinguished, which appears as a spanwise-organized zone of low-intensity in visualizations of vortical structures (as figure 31 and 45). Further downstream, new streaks are formed through the usual regeneration cycle between streaks and streamwise vortices. Since the large-scale downward (upward) motion brings high-speed (low-speed) fluid towards (away from) the wall, cyclic variations of local friction are induced. The consequences of the presence of “rollers” are somewhat similar to the flow over a wavy wall (spanwise averaged wall-transpiration velocity has indeed a sinusoidal shape below the large structures, cf. figure 45). One important point of the streak/roller cycle is the phase velocity at which the “rollers” are moving with respect to the frame. Stability analysis indicates a value around $10\,u_\tau$ [15]. An estimation using streamwise space-time correlations of the $(k_z = 0)$-modes of streamwise velocity of *case 11* (small box, high porosity) at a wall-distance of $y^+ = 30$ gives a value of $12.6\,u_\tau$. This range of values corresponds roughly to the speed at which structures in the buffer layer (streaks, streamwise vortices) move [16].

Spanwise streak spacing. As observed in §4.6, the spanwise streak spacing is 50 % higher near the porous wall of *case 15* than its usual value. Considering the described “intermittent” behavior of streak activity along the streamwise direction, one is tempted to hold the presence of “rollers” responsible for the increase in mean spanwise streak spacing. If the streak activity is regularly interrupted by nearly quiescent, spanwise-coherent zones then the statistical measure of spanwise streak spacing will increase.

5 Summary and conclusions

We have investigated fully developed turbulent channel flow over a porous surface. A new numerical algorithm has been constructed and direct numerical simulations have been performed at different porosity levels and in boxes of different sizes.

We have analyzed one-point and two-point statistical data as well as instantaneous visualizations of various quantities. Results have been interpreted with respect to the regeneration cycle of near-wall turbulence. Our main observations can be summarized as follows:

- Skin friction increases considerably on a porous wall – we have recorded up to 30% increase.
- The logarithmic law of velocity is maintained, only the intercept decreases with porosity.
- Turbulence activity is enhanced near the porous wall and – to a lesser extent – all the way across the channel.
- Near a porous surface, streamwise vortices are amplified and located closer to the wall on average. Streak intensity in wall units ($\omega_y'^{+}$) is reduced in the same region.
- Vertical velocity fluctuations – if normalized with the *rms* value of the intensity of streamwise vortices and their average wall-distance – is increased in the zone adjacent to the porous wall with respect to normal levels. By considering potential flow induced by point vortices near a porous wall, one can qualitatively explain this phenomenon. As a consequence, streak formation by advection is increased in *absolute* terms.
- Unusually high spanwise auto-correlations of velocity are observed near the porous surface. In the case of pressure, these extend across the whole channel height. Alternating, roller-like structures with spanwise orientation are detected in "snapshots" of various fields, manifesting themselves also as high streamwise anti-correlations of pressure, streamwise and wall-normal velocity at large separations. The fluctuation energy contained in the two-dimensional motion in the (wall-normal/streamwise)-plane takes considerable values, up to 30% of total turbulent kinetic energy. Statistically, vertical motion directed *towards* the wall correlates with low streak intensity, i.e. the "rollers" are squashing the streaks during their down-wash. It has also been found that these "rollers" correlate highly with local streamwise skin friction variation and with a kind of intermittent behavior of streaks along that direction. The situation has been compared qualitatively with motion over a wavy wall.

We have thus identified two mechanisms through which turbulent flow is affected by a porous surface: (i) increased streak formation due to higher vortex-induced wall-normal velocities; (ii) cyclic lift-up and wash-down of streaks through spanwise-coherent, large vortices which owe their presence to a Kelvin-Helmholtz-type instability. Figure 3 shows schematically which parts of the near-wall regeneration cycle of turbulence are concerned by these effects. Mechanism (i) directly leads to an acceleration of the turbulence cycle. Mechanism (ii) leads to strong cyclic variations of local skin-friction. At the present time we have not fully understood the consequences for the mean drag, but we believe that the streak/roller cycle is the dominant mechanism responsible for overall drag increase.

It is, however, difficult to determine unambiguously the exact amount of the porosity-induced drag increase with the aid of an experimental configuration such as the present one. The reason lies in the small value of the lower neutral streamwise wavenumber of the roller-structures which – obtained from linear stability analysis [15] – corresponds to a wavelength of the order of $120h$. Since for domain-size-independent results a simulation should at least allow for structures of this size to be taken into account, the computational requirements become prohibitive. In this respect, the present simulations correspond to cases where the maximum size of "rollers" is constrained *implicitly* by the computational box. In a physical experiment, on the other hand, the present

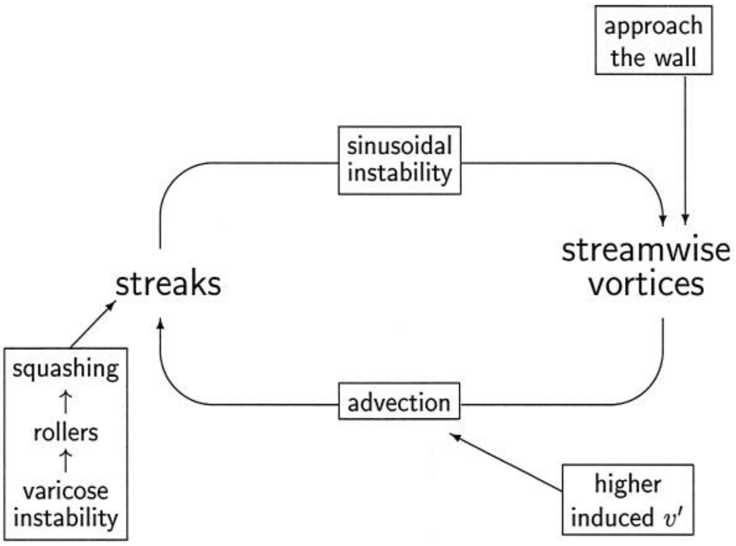

Figure 3: Schematic of the influence of wall porosity on the different ingredients of the near-wall turbulence regeneration cycle.

boundary condition would probably be realized by means of a regular-spaced streamwise partitioning of the plenum chamber (cf. figure 1) which allows for the pressure in each such compartment to adjust itself to the local mean pressure in the channel and thereby guaranteeing approximately the requested linear variation. Such compartments would then constrain the streamwise correlation of fluctuating wall-transpiration. Consequently, roller-like structures above the wall would probably not exceed the size of one such compartment. Numerically, one can simulate this behavior by *explicitly* filtering the induced wall-transpiration e.g. by a spectral cut-off below a minimum streamwise wavenumber. This type of experiment is currently performed and will be reported at a later point. Another implication of the present results is the possibility of an artificial wall condition which could have similar effects as "natural" porosity. One could impose a periodic transpiration velocity, moving at a phase speed equal to the one of the streaks.

References

[1] M. Abramowitz and I.A. Stegun. *Handbook of mathematical functions.* Dover, 1964.

[2] G.K. Batchelor. *An introduction to fluid dynamics.* Cambridge University Press, 1967.

[3] C. Canuto, M.Y. Hussaini, A. Quarteroni, and T.A. Zang. *Spectral methods in fluid dynamics.* Springer, 1988.

[4] H. Choi, P. Moin, and J. Kim. Active turbulence control for drag reduction in wall-bounded flows. *J. Fluid Mech.*, 262:75–110, 1994.

[5] E. Coustols and A.M. Savill. Turbulent skin-friction drag reduction by active and passive means: Part I. Technical Report 786, AGARD, 1992.

[6] C. de Boor. *A practical Guide to Splines.* Springer, 1978.

[7] M.A. Gillan. Computational analysis of buffet alleviation in viscous transonic flow over a porous airfoil. *AIAA J.*, 33(4):769–773, 1995.

[8] J.M. Hamilton, J. Kim, and F. Waleffe. Regeneration mechanisms of near-wall turbulence structures. *J. Fluid Mech.*, 287:317–348, 1995.

[9] C.G. Hirsch. *Numerical computation of internal and external flows.* J. Wiley, 1990.

[10] E.N. Houstis, E.A. Vavalis, and J.R. Rice. Convergence of $\mathcal{O}(h^4)$ cubic spline collocation methods for elliptic partial differential equations. *SIAM J. Numer. Anal.*, 25:55–74, 1988.

[11] J.C. Hunt and J.M. Graham. Free-stream turbulence near plane boundaries. *J. Fluid Mech.*, 84(2):209–235, 1978.

[12] J. Jiménez. On the structure and control of near wall turbulence. *Phys. Fluids*, 6(2):944–953, 1994.

[13] J. Jiménez. The largest scales of turbulent wall flows. *CTR Res. Briefs*, 1998.

[14] J. Jiménez. Turbulence. In *Developments in Fluid Mechanics: A Collection for the Milennium.* Cambridge U. Press, to appear.

[15] J. Jiménez, G. Kawahara, A. Pinelli, and M. Uhlmann. Linear stability analysis of turbulent channel flow including porous walls. Technical Note ETSIA MF-9811, School of Aeronautics, Universidad Politécnica Madrid, Spain, 1998.

[16] J. Jiménez and P. Moin. The minimal flow unit in near-wall turbulence. *J. Fluid Mech.*, 225:213–240, 1991.

[17] J. Jiménez and A. Pinelli. The autonomous cycle of near-wall turbulence. *J. Fluid Mech.*, 389:335–359, 1999.

[18] J. Kim. On the structure of pressure fluctuations in simulated channel flow. *J. Fluid Mech.*, 205:421–451, 1989.

[19] J. Kim, P. Moin, and R. Moser. Turbulence statistics in a fully developed channel flow at low Reynolds number. *J. Fluid Mech.*, 177:133–166, 1987.

[20] K.C. Kim and R.J. Adrian. Very large-scale motion in the outer layer. *Phys. Fluids*, 11(2):417–422, 1999.

[21] P. Koumoutsakos. Vorticity flux control for a turbulent channel flow. *Phys. Fluids*, 11(2):248–250, 1999.

[22] P. Koumoutsakos, T.R. Bewley, E.P. Hammond, and P. Moin. Feedback algorithms for turbulence control – some recent developments. AIAA paper no. 97-2008, 1997.

[23] S.K. Lele. Compact finite difference schemes with spectral-like resolution. *J. Comp. Physics*, 103:16–42, 1992.

[24] P. Lombardi, V. De Angelis, and S. Banerjee. The effect of boundary conditions and shear rate on streak formation and breakdown in turbulent channel flows. *Phys. Fluids*, 8(6):1643–1665, 1996.

[25] T.R. Lucas. Error bounds for interpolating cubic splines under various end conditions. *SIAM J. Numer. Anal.*, 11:569–585, 1974.

[26] K. Mahesh. A family of high order finite difference schemes with good spectral resolution. CTR Manuscript 162, Stanford University, USA, 1996.

[27] B. Perot and P. Moin. Shear-free turbulent boundary layers. Part 1. Physical insights into near-wall turbulence. *J. Fluid Mech.*, 295:199–227, 1995.

[28] W.H. Press, S.A. Teukolsky, W.H. Vetterling, and B.P. Flannery. *Numerical recipes in Fortran 77.* Cambridge U. Press, second edition, 1986.

[29] M. Rashidi and S. Banerjee. The effect of boundary conditions and shear rate on streak formation and breakdown in turbulent channel flows. *Phys. Fluids A*, 2(10):1827–1838, 1990.

[30] H. Schlichting. *Boundary-Layer Theory.* McGraw-Hill, seventh edition, 1979.

[31] W. Schoppa and F. Hussain. Formation of near-wall streamwise vortices by streak instability. AIAA paper no. 98-3000, 1998.

[32] L.L. Schumaker. *Spline functions: basic theory.* J. Wiley, 1981.

[33] C. Wagner and R. Friedrich. On the turbulence structure in solid and permeable pipes. TSF 11, Grenoble, France, 1997.

[34] C. Wagner and R. Friedrich. On the turbulence structure in solid and permeable pipes. *Int. J. Heat & Fluid Flow*, 19(5):459–469, 1998.

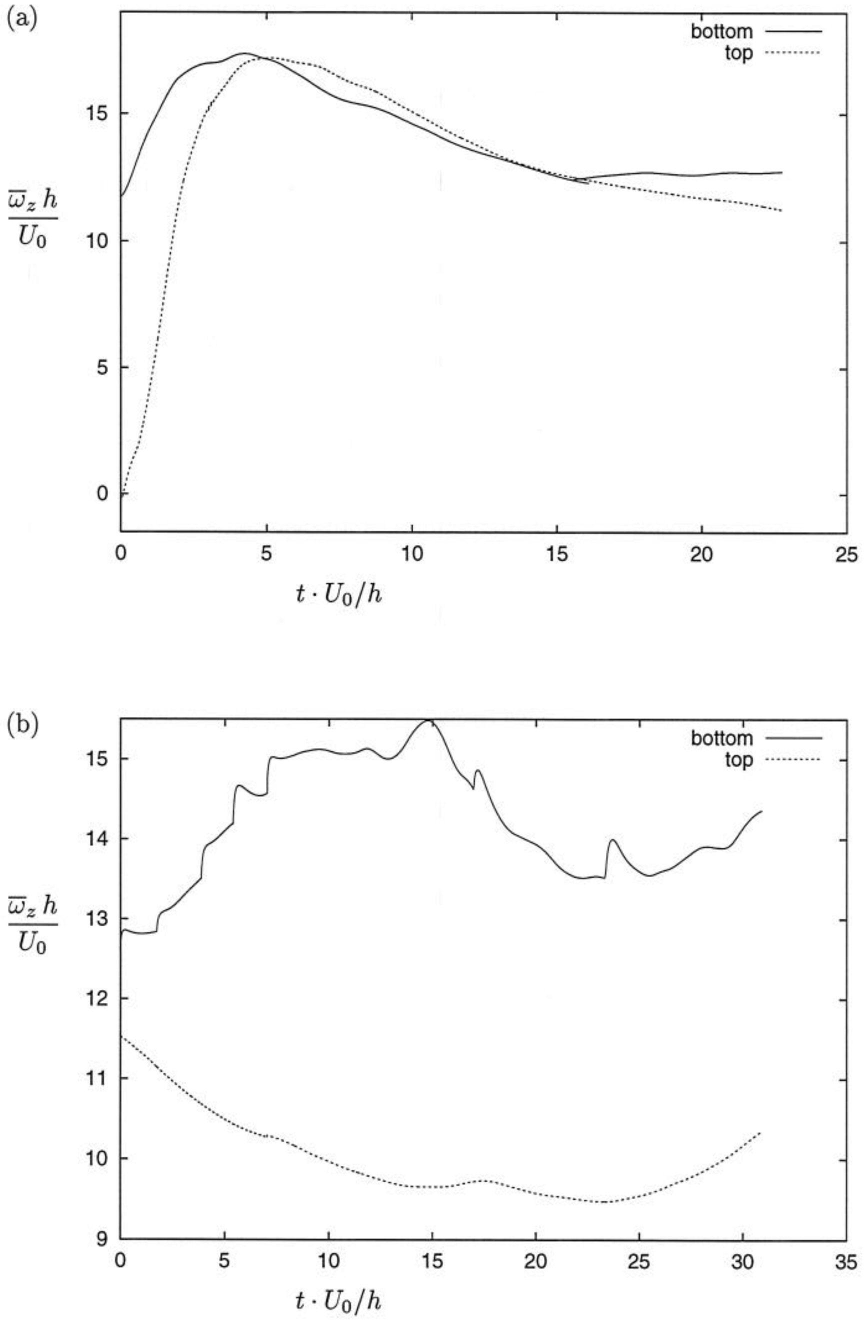

Figure 4: Time variation of the plane-averaged wall friction on the two walls during the initial transient of run *case 15*. (a) both walls are impermeable and relax from initial interpolation; (b) porosity is now turned on at the bottom wall. Observed kinks in (b) are due to the numerical artifact discussed in §4.2

(a)

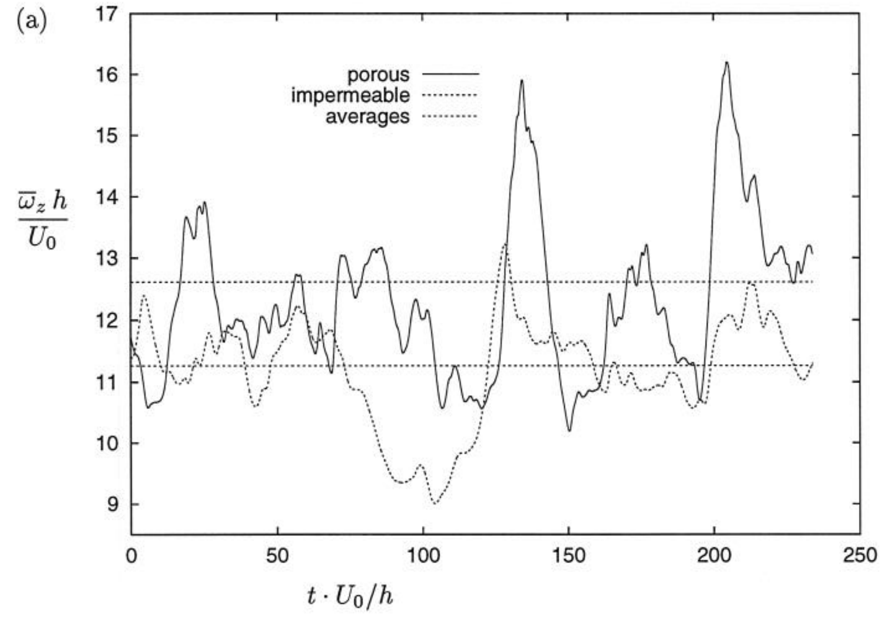

(b)

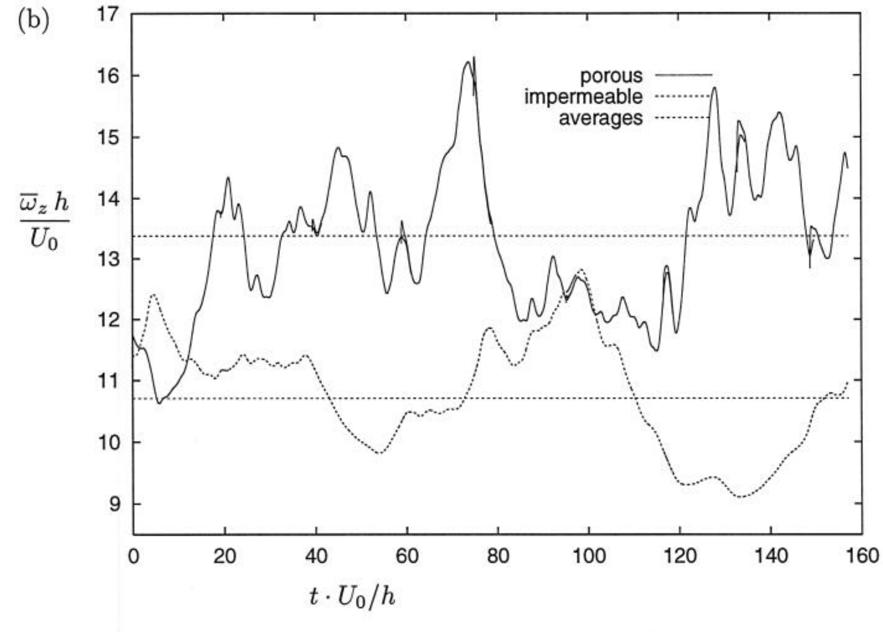

Figure 5: Time variation of the plane-averaged wall friction on the lower (porous) and upper (impermeable) wall. (a) run *case 8* (small box, low porosity); (b) run *case 11* (small box, high porosity). The horizontal lines indicate the respective time-averaged values for each wall. The difference between top and bottom wall amounts to 12% in *case 8* and to 25% in *case 11.*

(a)

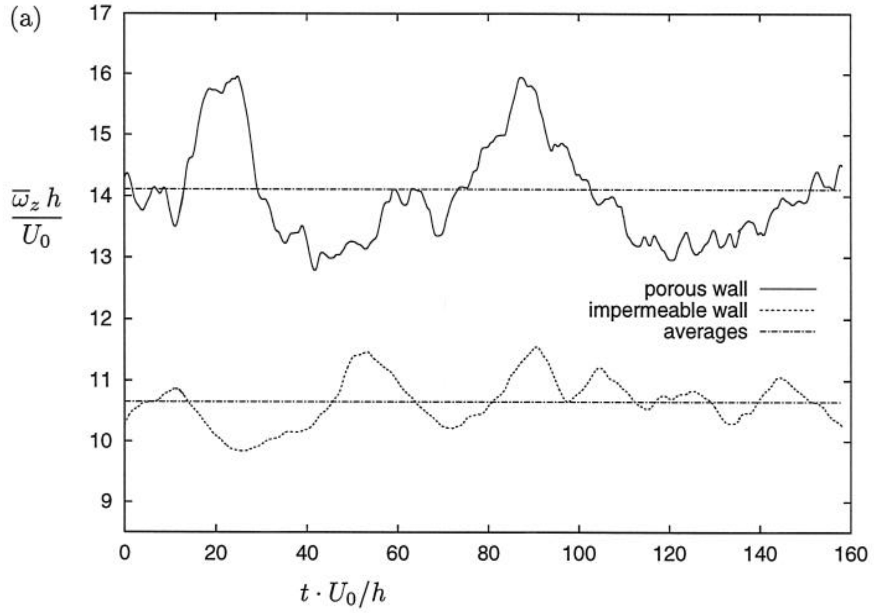

(b)

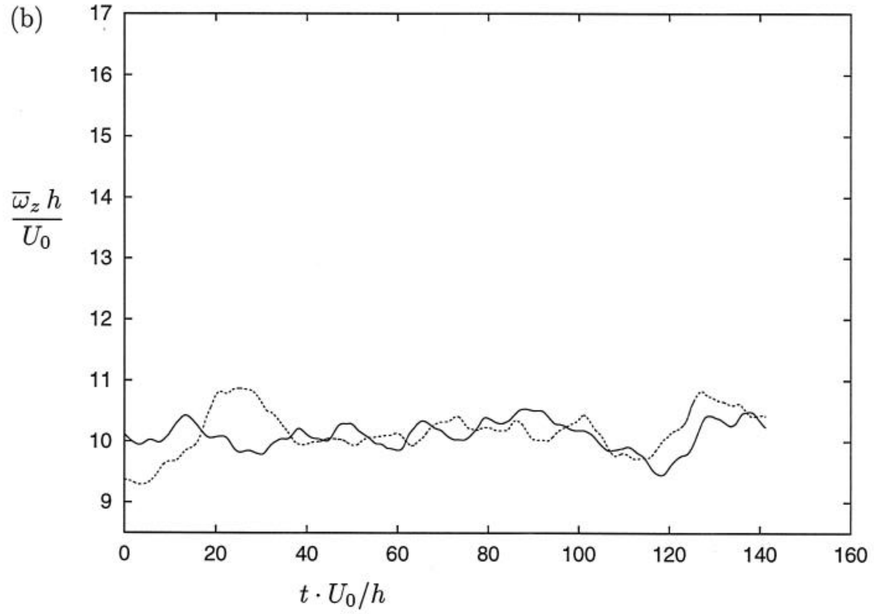

Figure 6: Time variation of the plane-averaged wall friction on the both walls: (a) run *case 15* (large box, high porosity); (b) run *case 16* (large box, impermeable). The horizontal lines in (a) indicate the respective time-averaged values for each wall. The difference between top and bottom wall amounts to 32.5% in *case 15*.

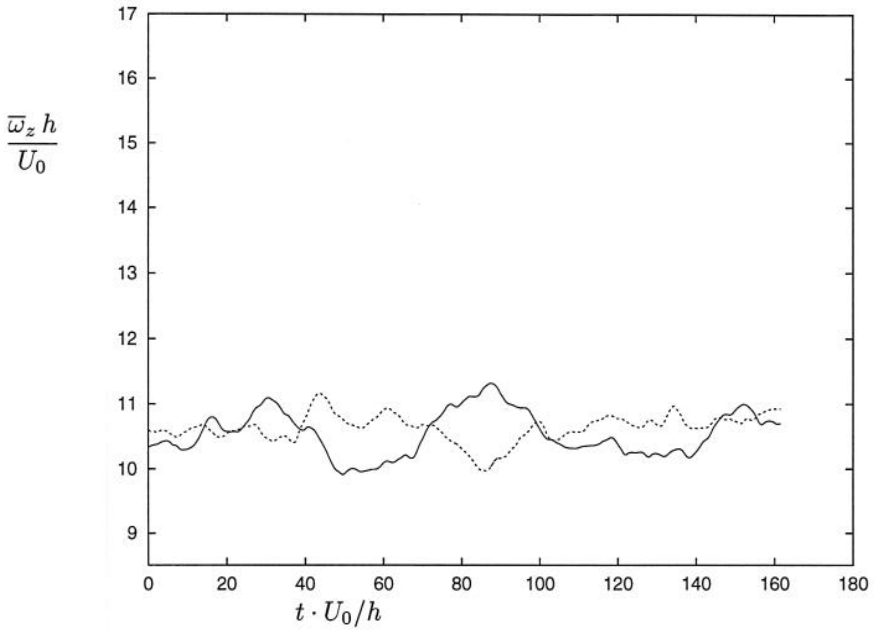

Figure 7: Time variation of the plane-averaged wall friction on the top and bottom wall of the reference *case 1* obtained by a fully spectral method. Note that the initial condition is not equal to the one used in the other cases.

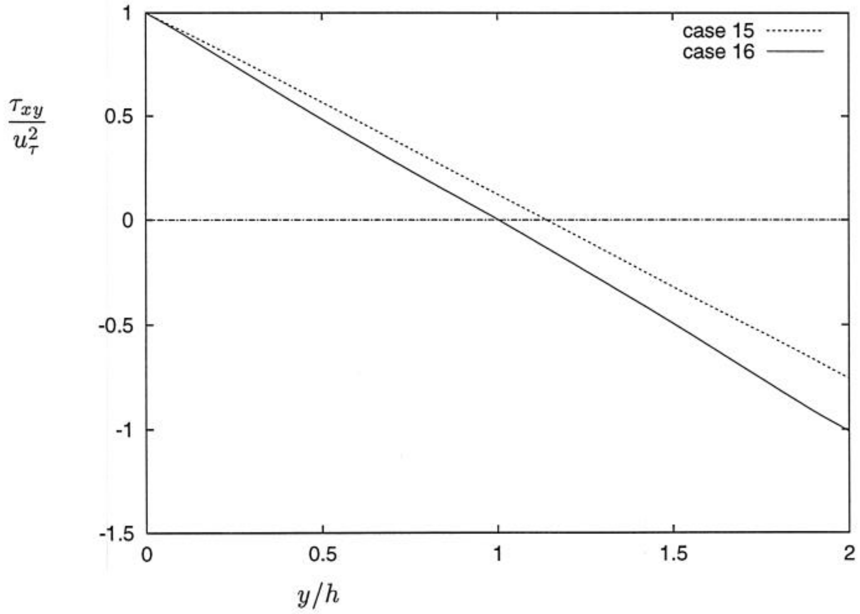

Figure 8: Variation of total tangential stress $\tau_{xy} = \nu \partial_y(U) - \overline{u'v'}$ over the channel cross-section indicating convergence of the second order statistics.

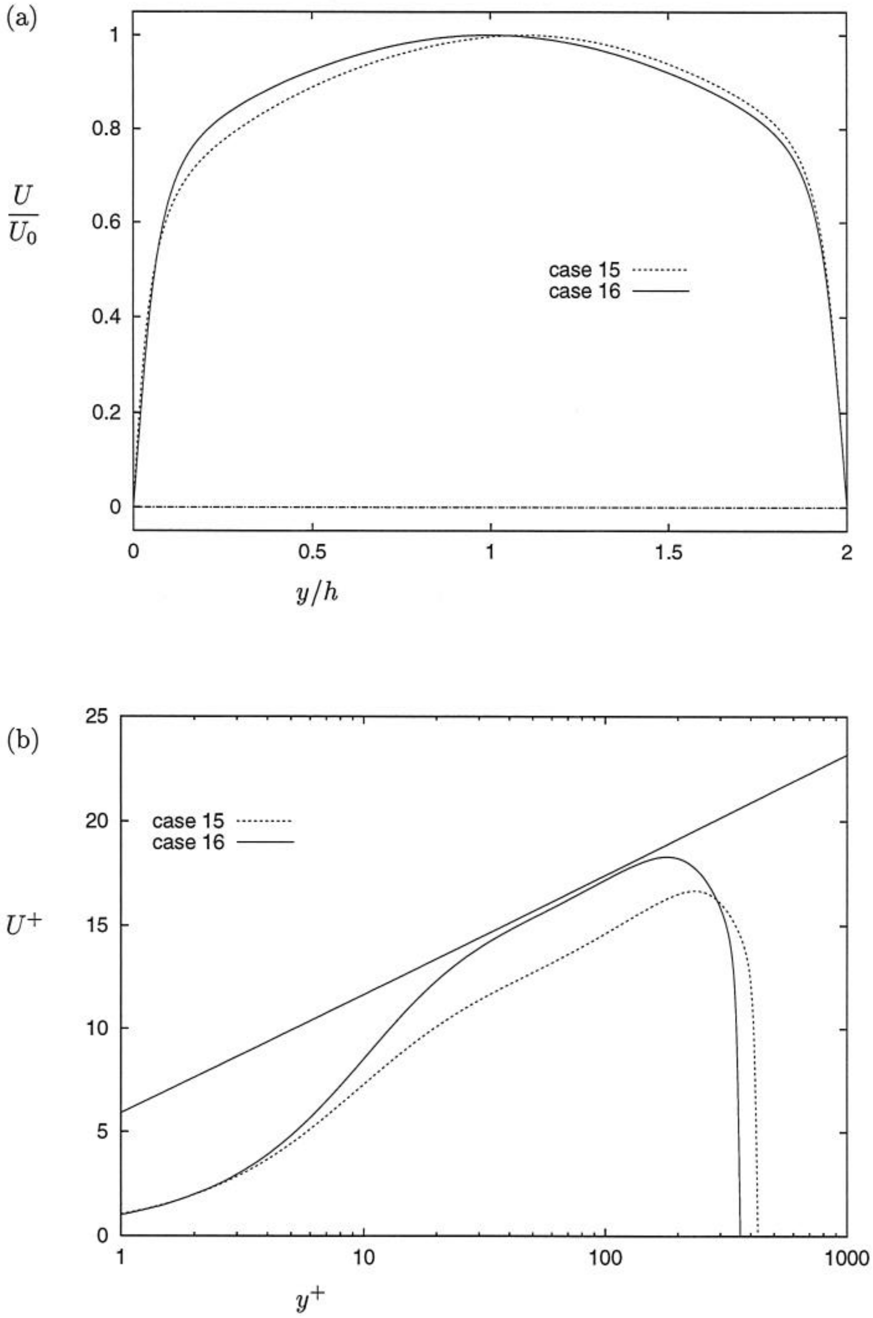

Figure 9: Mean velocity profiles of *case 15* and *case 16*. (a) profiles normalized by maximum velocity and (b) log-linear plot with normalization by the respective friction velocity. The straight line in (b) is given by $U^+ = 2.5\log(y^+) + 5.9$.

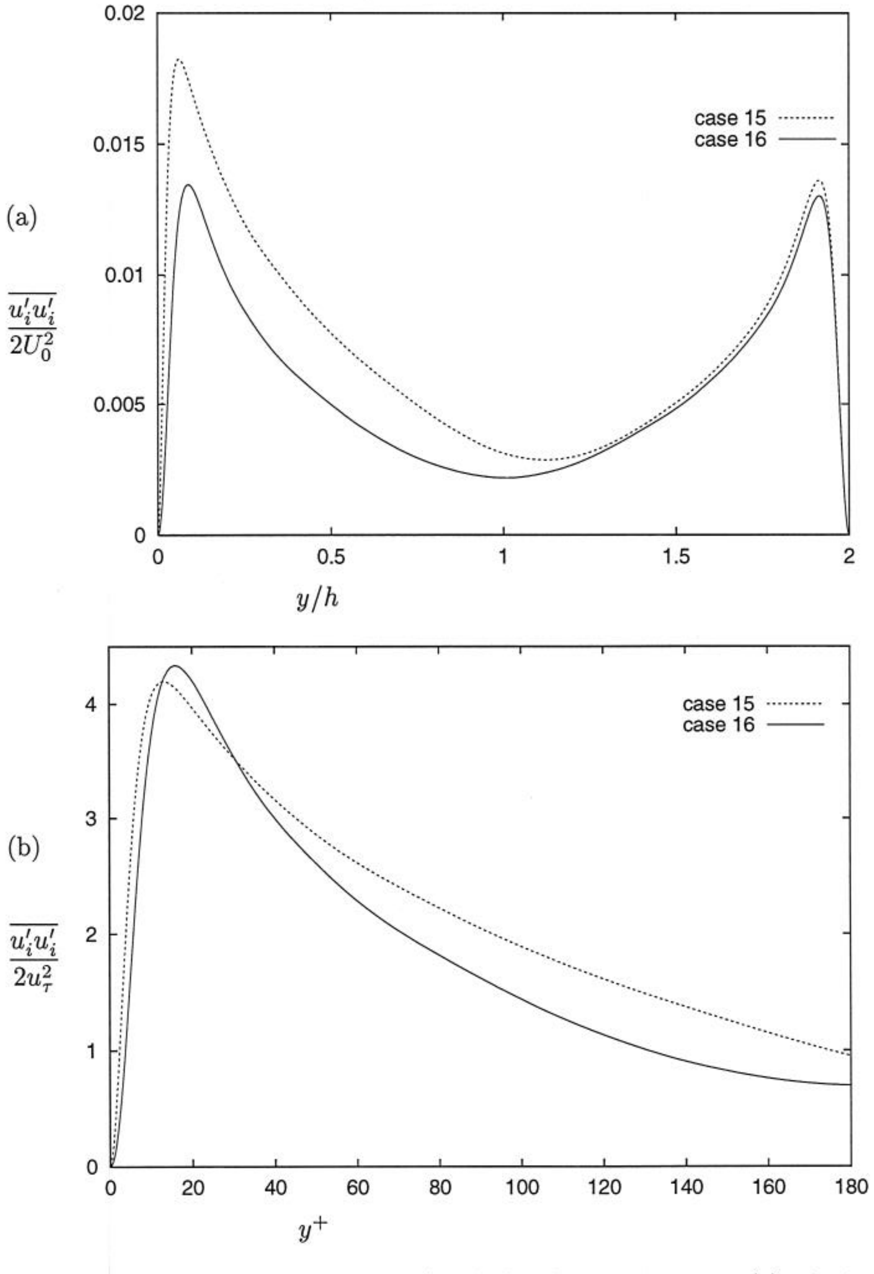

Figure 10: Wall-normal variation of turbulent kinetic energy. (a) relative to maximum mean kinetic energy, plotted across the whole channel; (b) relative to friction energy and plotted in the lower half only.

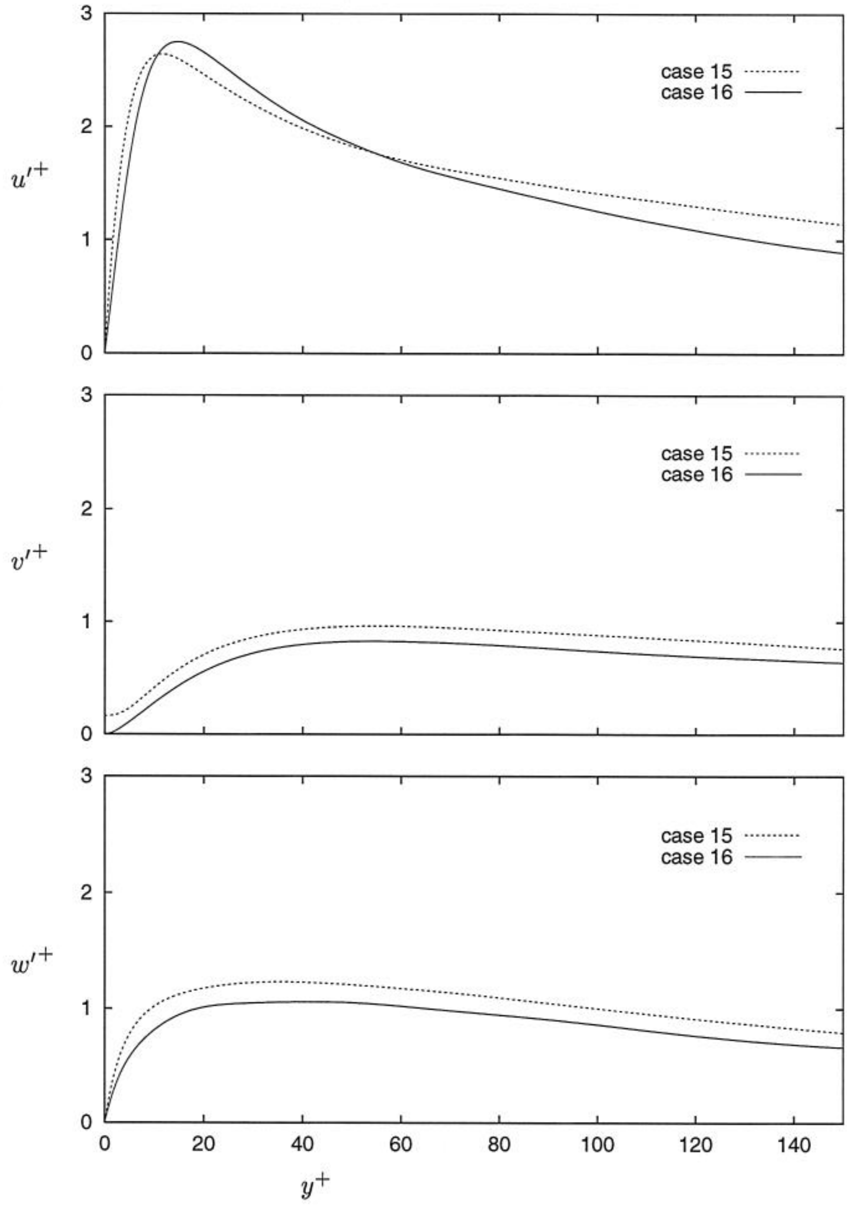

Figure 11: Profiles of *rms* values of fluctuating velocity components u'_i. Values are in wall units, based upon the friction velocity u_τ of each respective case.

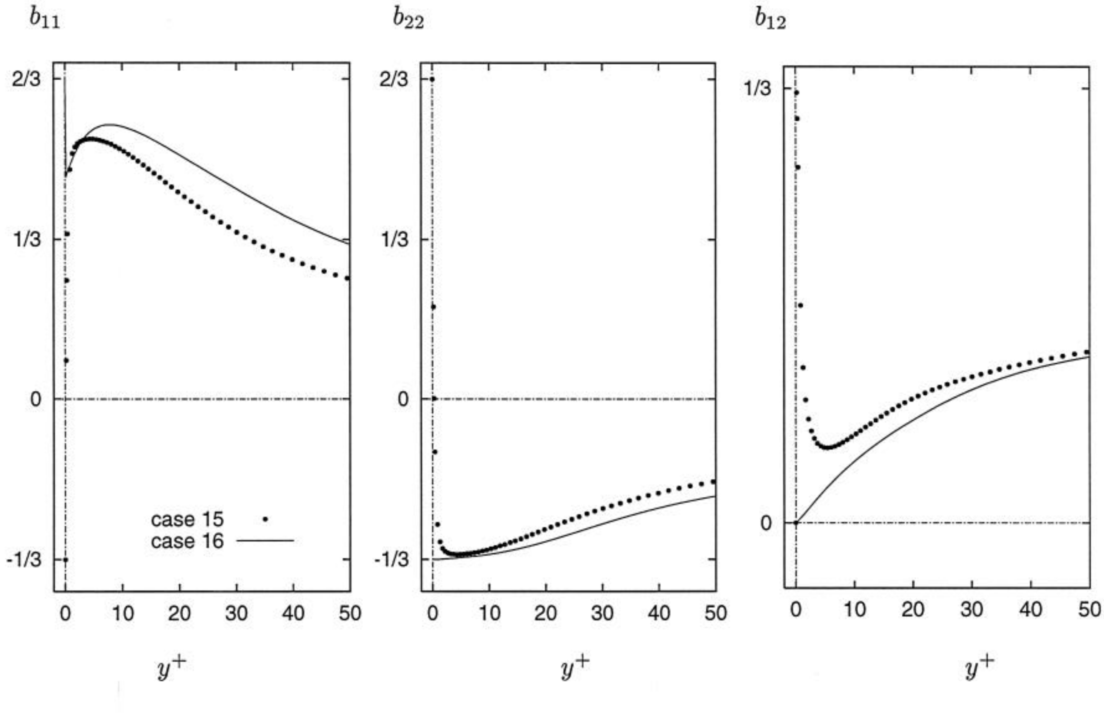

Figure 12: Near-wall behaviour of the anisotropy of the Reynolds stress $b_{ij} = \overline{u_i'u_j'}/\overline{u_k'u_k'} - \delta_{ij}/3$.

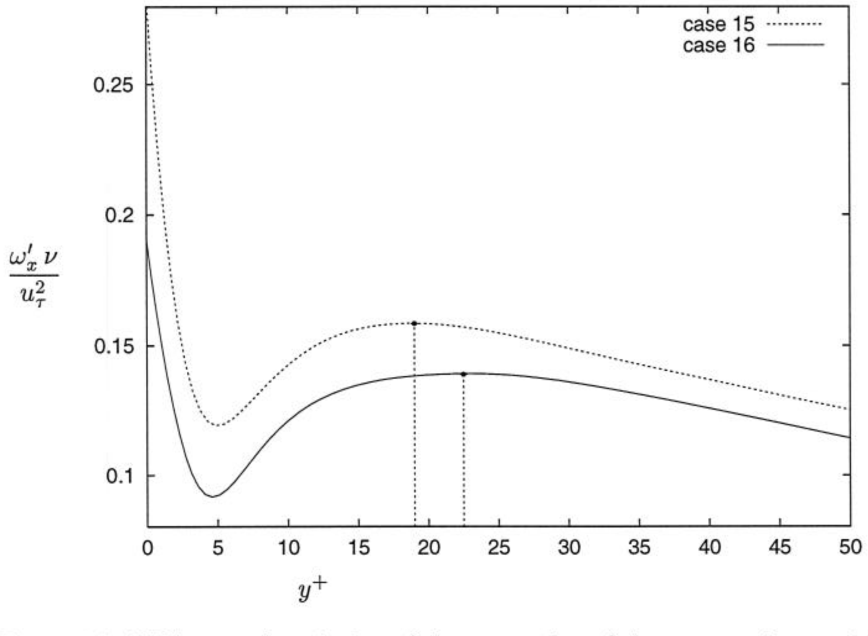

Figure 13: Wall-normal variation of the *rms* value of the streamwise vorticity fluctuations. The position of the respective second maximum is indicated by the vertical bars atached to the symbols. The wall units are based on the respective friction velocities u_τ of each run.

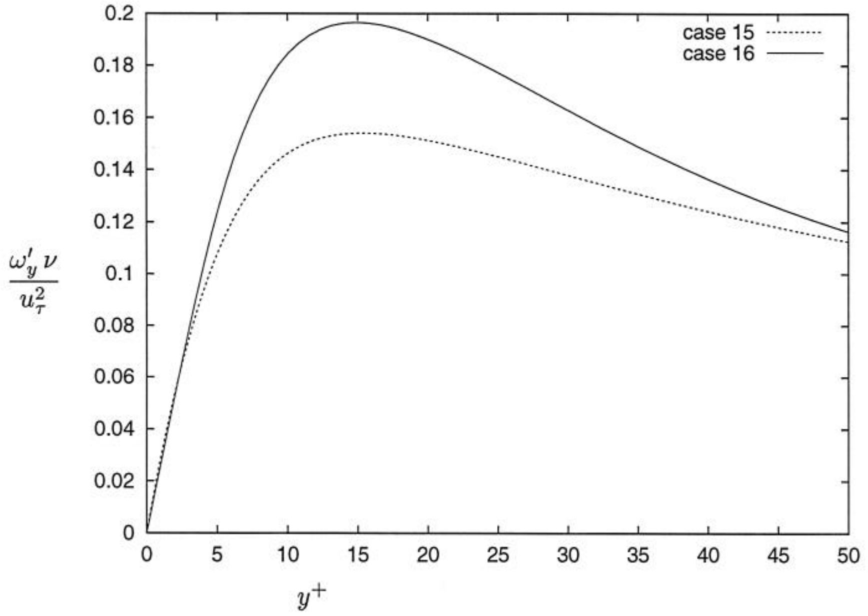

Figure 14: Wall-normal variation of the *rms* value of the wall-normal vorticity fluctuations. The wall units are based on the respective friction velocities u_τ of each run.

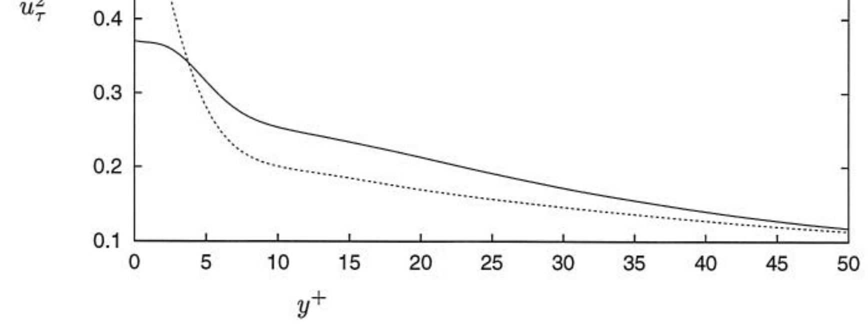

Figure 15: Wall-normal variation of the *rms* value of the spanwise vorticity fluctuations. The wall units are based on the respective friction velocities u_τ of each run.

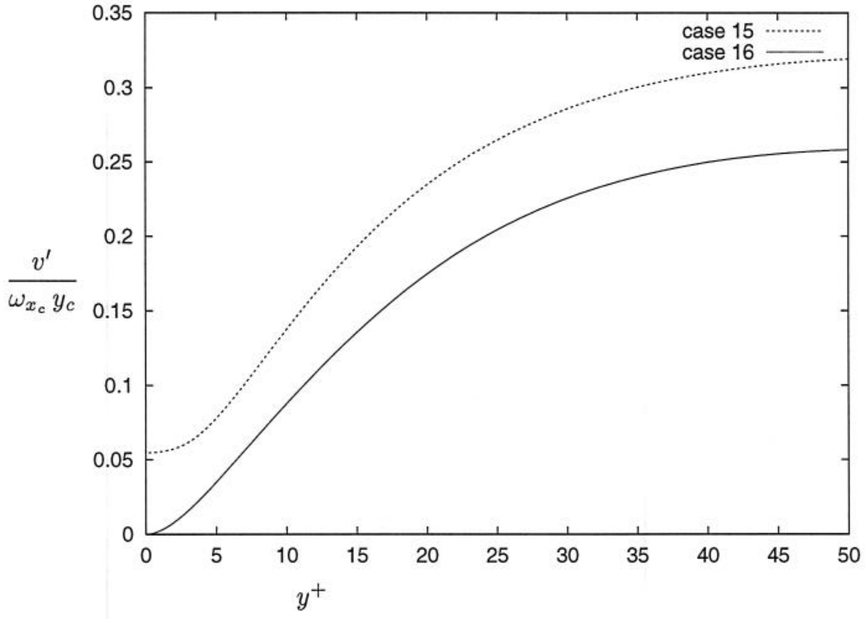

Figure 16: Ratio of wall-normal velocity fluctuation v' and streamwise vorticity ω_{x_c} and height y_c, where the subscript $()_c$ corresponds to the second maximum of figure 13.

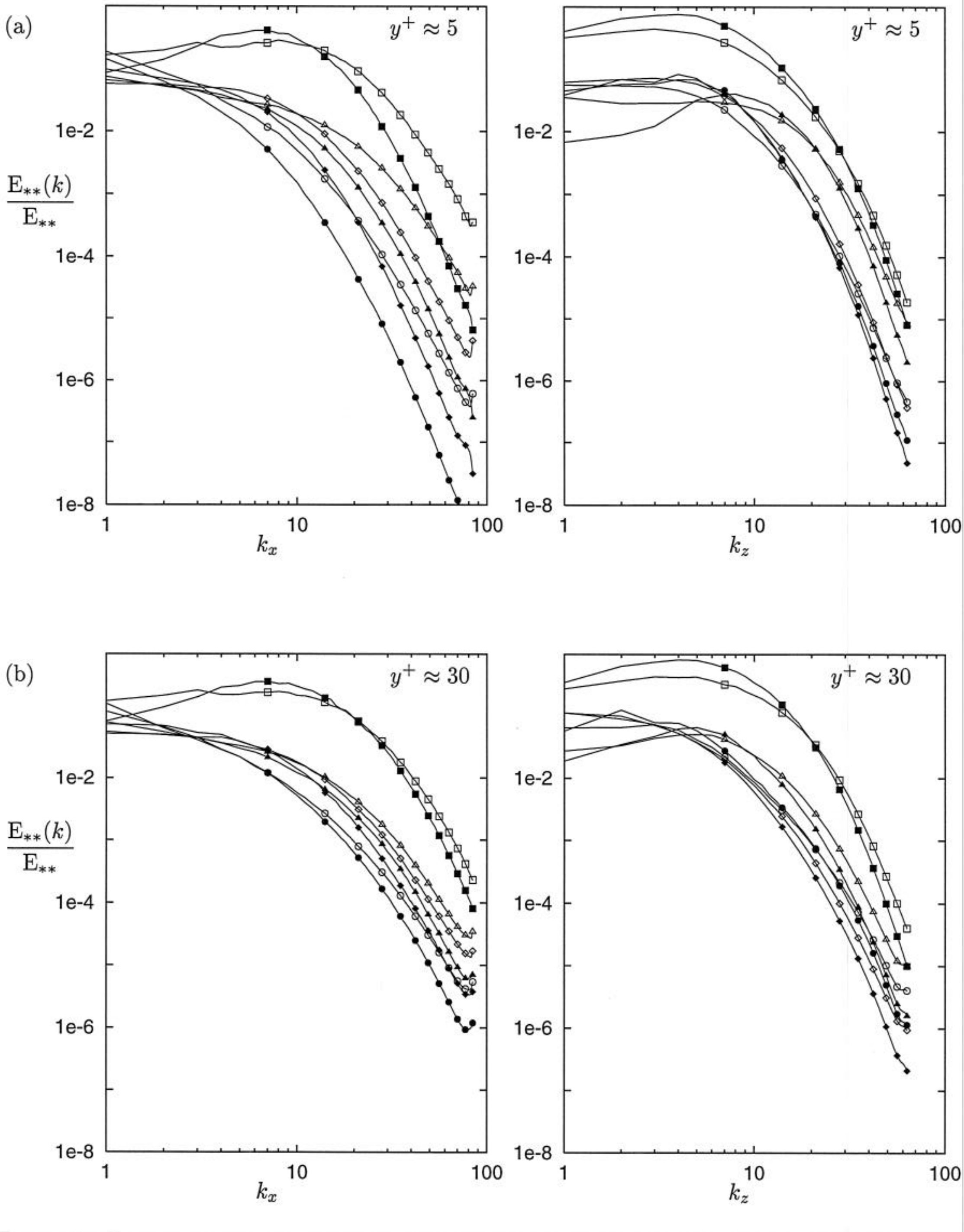

Figure 17: Time-averaged, one-dimensional energy spectra in stream- and spanwise direction. The spectra are normalized by the total energy of the respective component. Open symbols correspond to curves of the porous wall (*case 15*), closed symbols to the impermeable case (*case 16*). □ – streamwise velocity E_{uu}; ○ – wall-normal velocity E_{vv}; △ – spanwise velocity E_{ww}; ◇ – pressure E_{pp}.

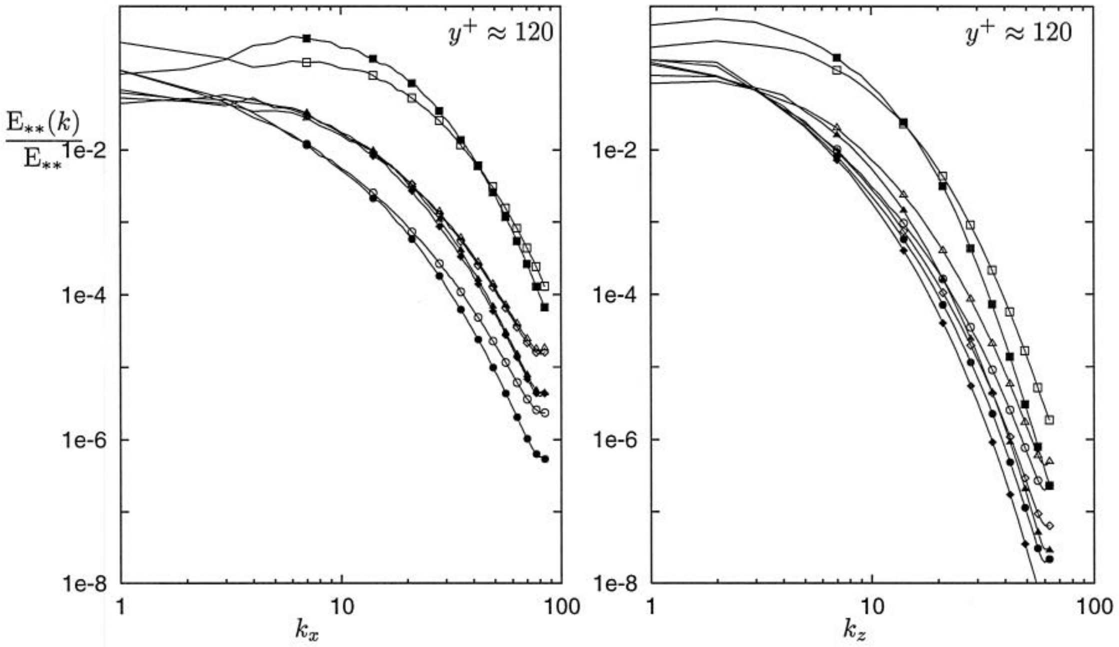

Figure 18: Time-averaged, normalized, one-dimensional energy spectra. Caption as in figure 17.

(a) $y^+ = 5.6$

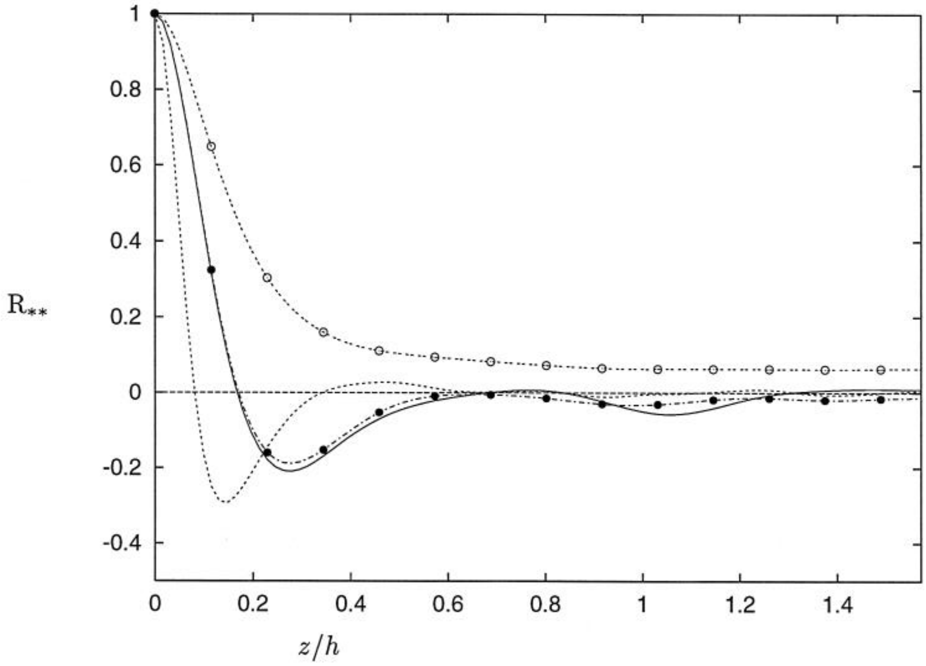

(b) $y^+ = 143$

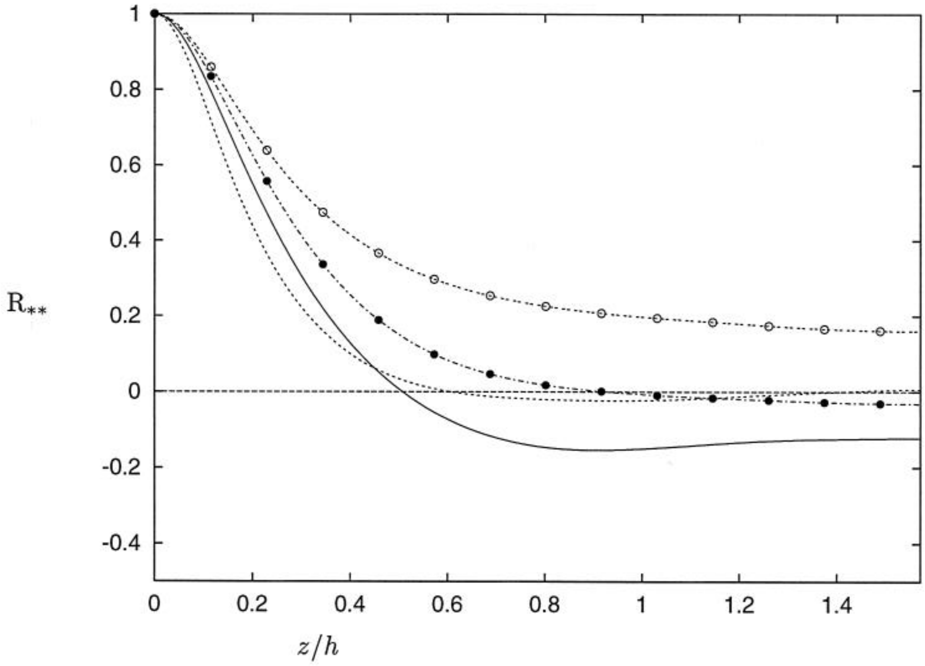

Figure 19: Time-averaged two-point autocorrelations of velocity and pressure of *case 16* at two different wall-distances and spanwise separations. — R_{uu}; - - R_{vv}; • R_{ww}; ∘ R_{pp}.

(a) $y^+ = 5.6$

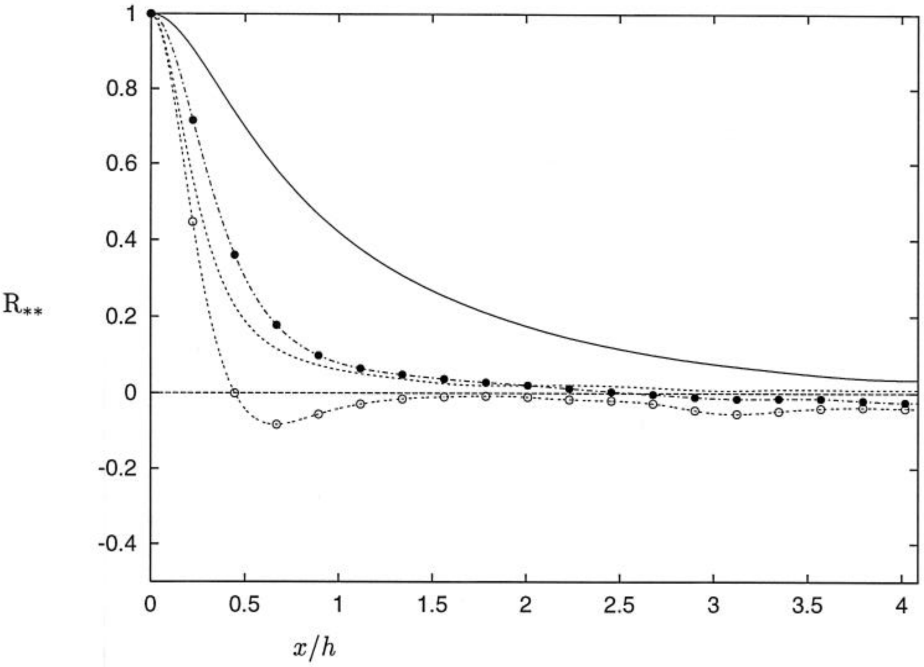

(b) $y^+ = 143$

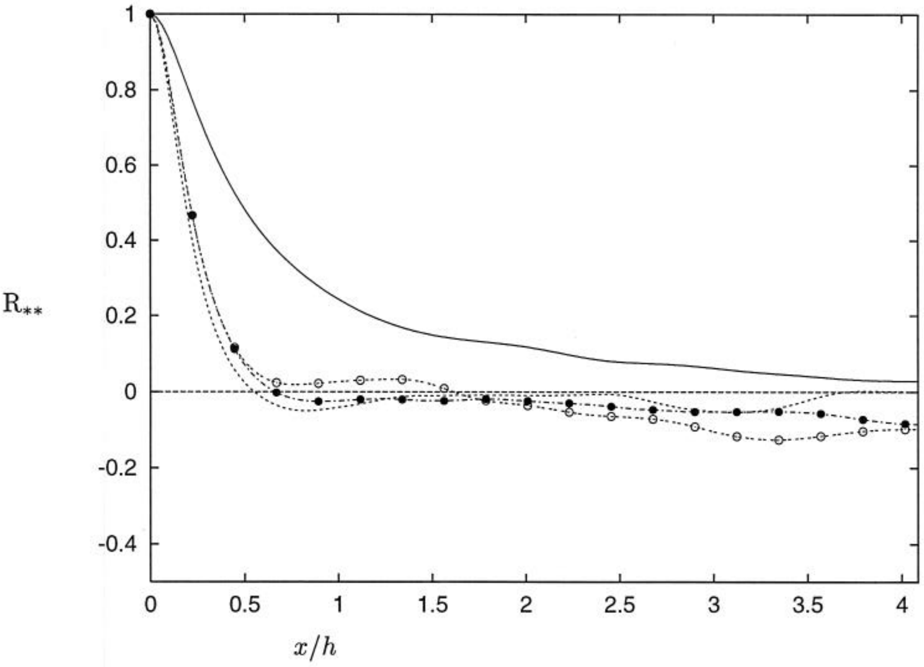

Figure 20: Time-averaged two-point autocorrelations of velocity and pressure of *case 16* at two different wall-distances and streamwise separations. — R_{uu}; - - R_{vv}; • R_{ww}; ∘ R_{pp}.

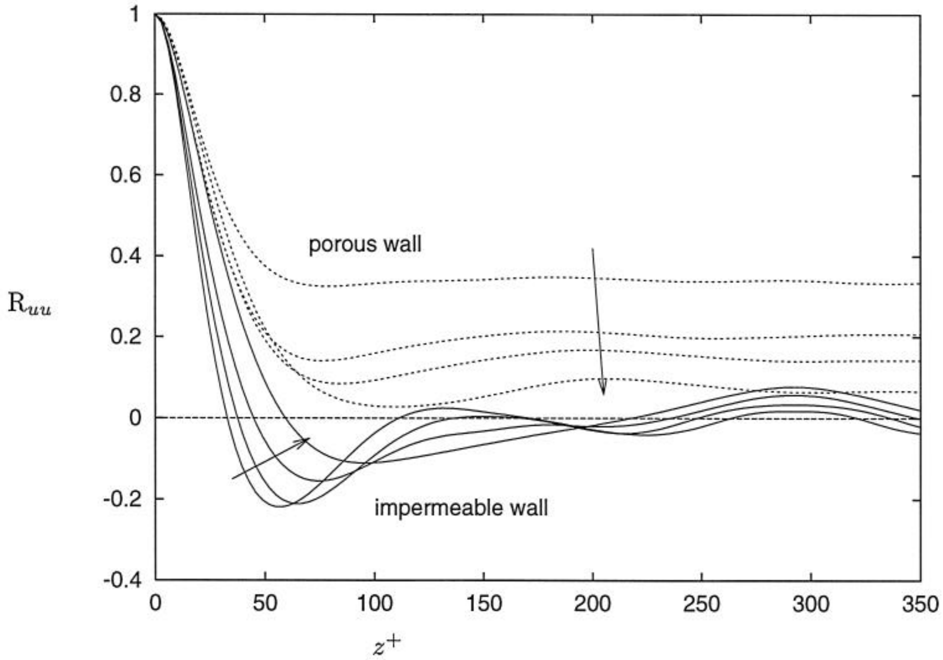

Figure 21: Time-averaged two-point autocorrelations of streamwise velocity of *case 15* at different wall-distances $y^+ = \{5, 17, 30, 50\}$ above the bottom (porous) and the top (impermeable) wall. Arrows indicate increasing wall distance. Note that wall units are local to each wall.

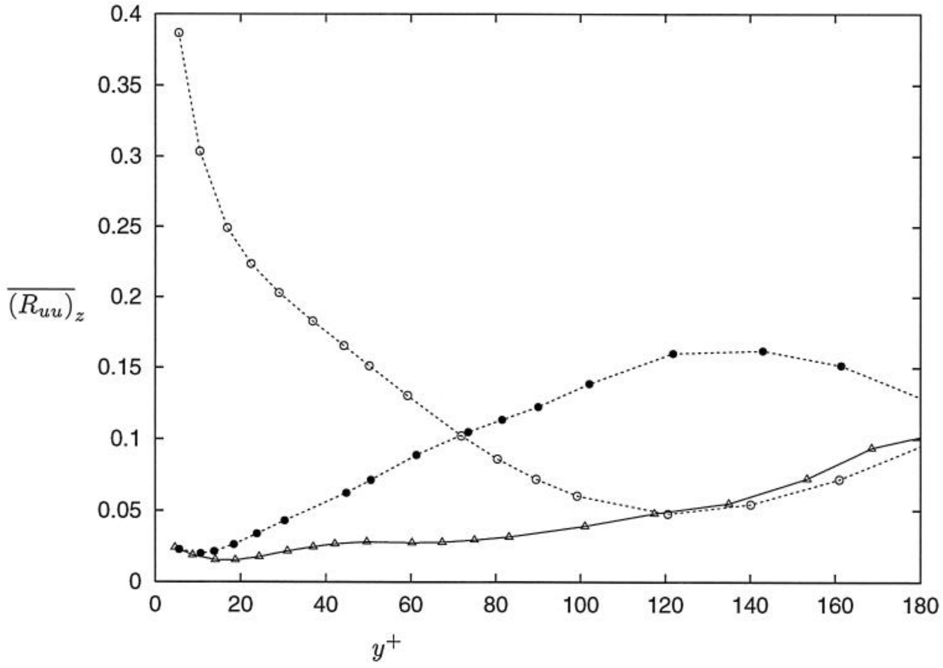

Figure 22: Mean value over box-width of autocorrelation of streamwise velocity for spanwise separations as a function of wall-distance. ○ – bottom (porous) wall of *case 15*; • – top (impermeable) wall of *case 15*; △ – impermeable *case 16*.

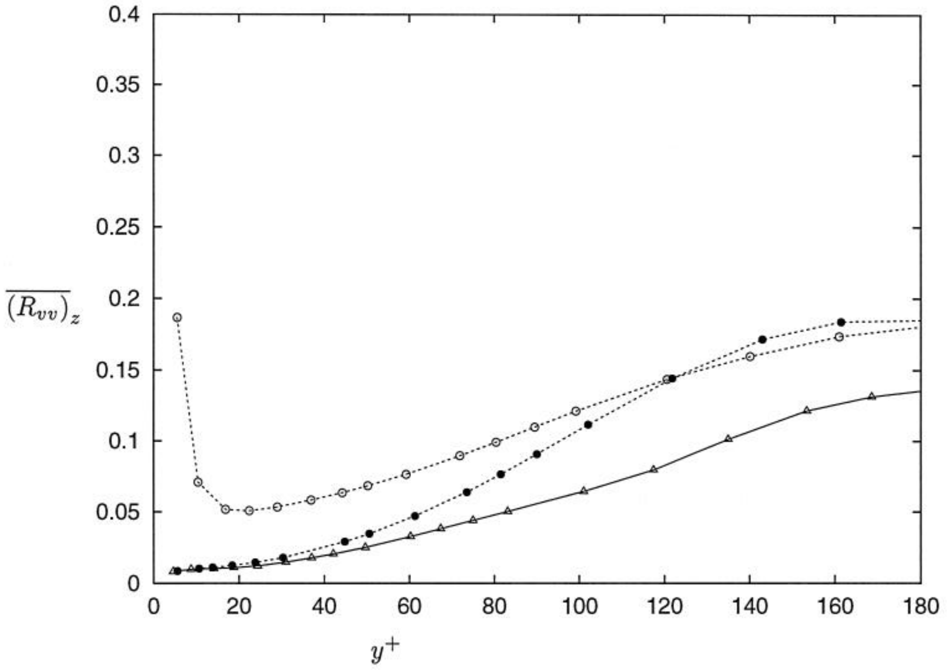

Figure 23: Mean value over box-width of autocorrelation of wall-normal velocity for spanwise separations as a function of wall-distance. ∘ – bottom (porous) wall of *case 15*; • – top (impermeable) wall of *case 15*; △ – impermeable *case 16*.

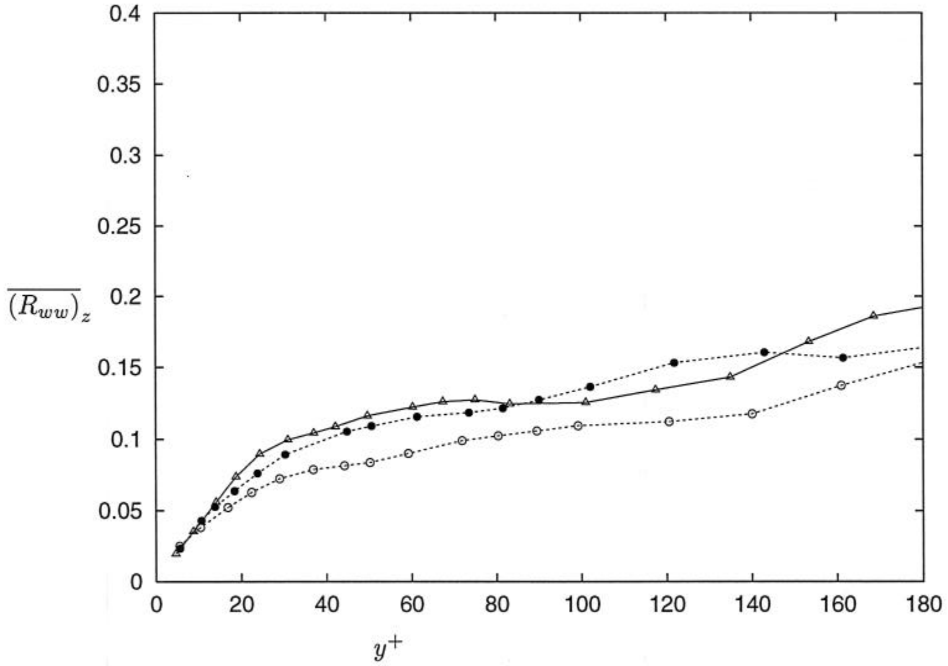

Figure 24: Mean value over box-width of autocorrelation of streamwise velocity for spanwise separations as a function of wall-distance. ∘ – bottom (porous) wall of *case 15*; • – top (impermeable) wall of *case 15*; △ – impermeable *case 16*.

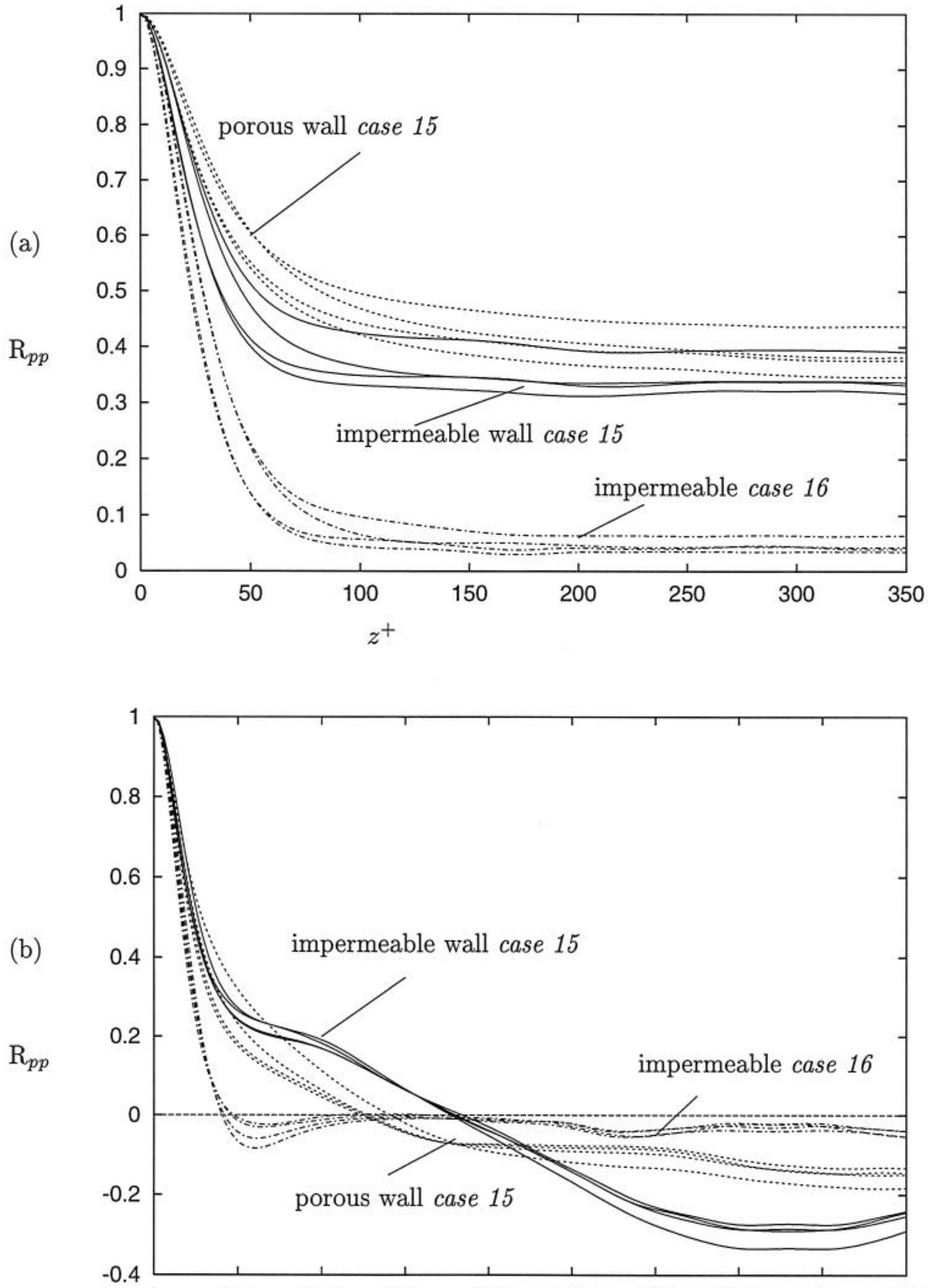

Figure 25: Time-averaged two-point autocorrelations of pressure at different wall-distances $y^+ = \{5, 17, 30, 50\}$ above the porous wall of *case 15*, the impermeable wall of *case 15* and the impermeable wall of *case 16*. (a) spanwise separation; (b) streamwise separation. Wall units are local to each wall.

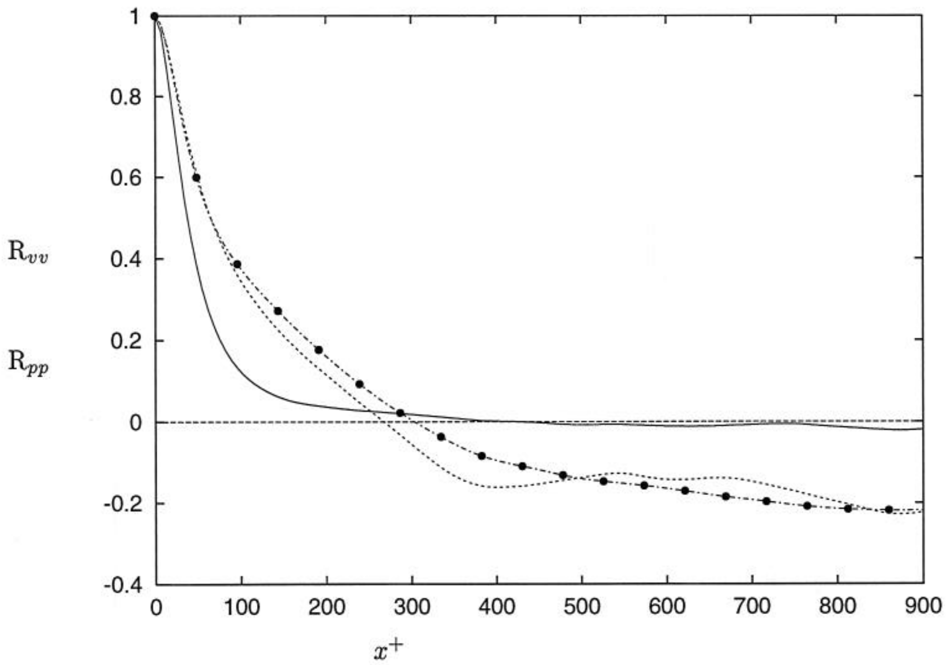

Figure 26: Time-averaged two-point autocorrelations of full wall-normal velocity (continous line —), its two-dimensional mode in x, y-plane (discontinous line - -) and of full pressure (symbol •) at $y^+ = 70$ above the porous wall of *case 15*.

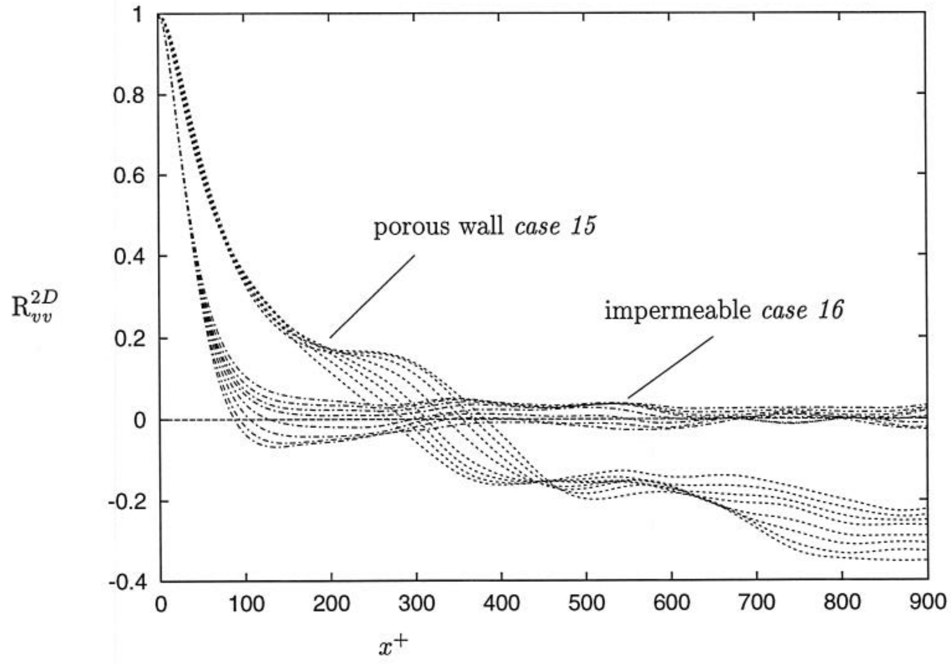

Figure 27: Time-averaged two-point autocorrelations of the two-dimensional mode (x, y-plane) of wall-normal velocity at different wall-distances in the interval $70 \leq y^+ \leq 180$ above the porous wall of *case 15* and the impermeable wall of *case 16*.

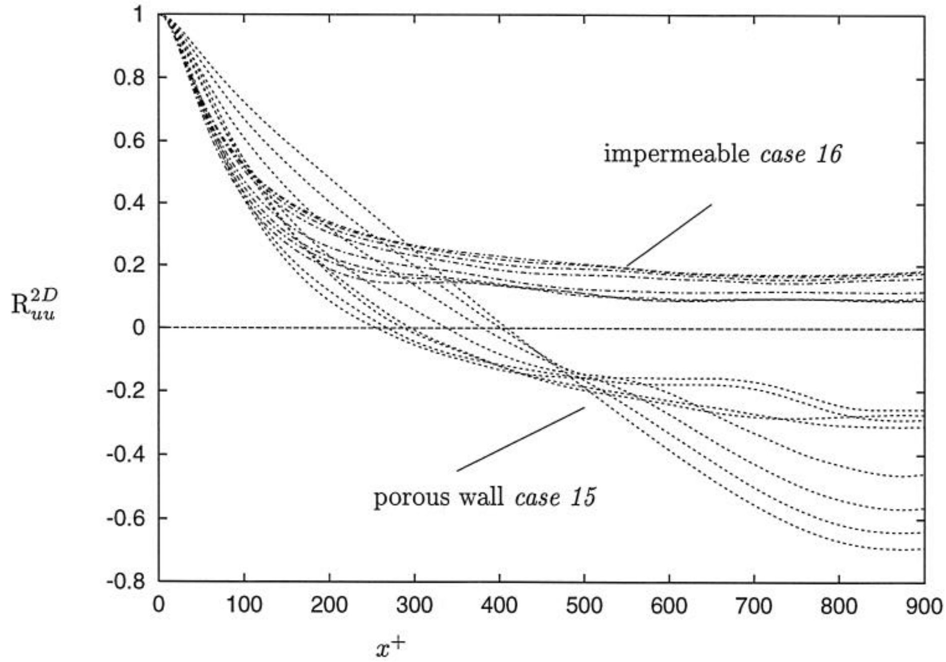

Figure 28: Time-averaged two-point autocorrelations of the two-dimensional mode (x, y-plane) of streamwise velocity at different wall-distances in the interval $70 \leq y^+ \leq 180$ above the porous wall of *case 15* and the impermeable wall of *case 16*. Note that the scale of the ordinate is different from figures 27 and 29.

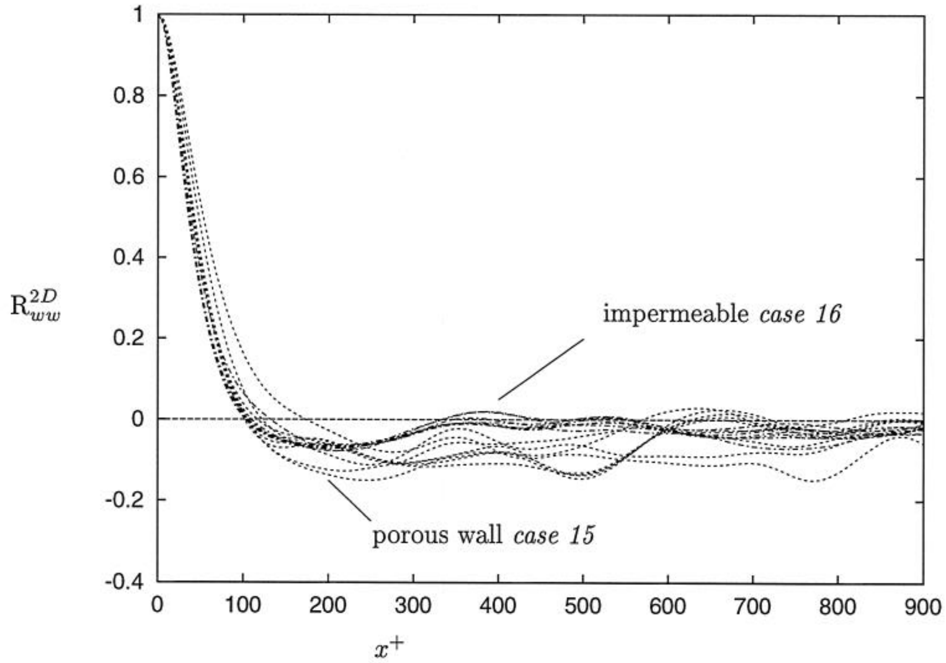

Figure 29: Time-averaged two-point autocorrelations of the two-dimensional mode (x, y-plane) of spanwise velocity at different wall-distances in the interval $70 \leq y^+ \leq 180$ above the porous wall of *case 15* and the impermeable wall of *case 16*.

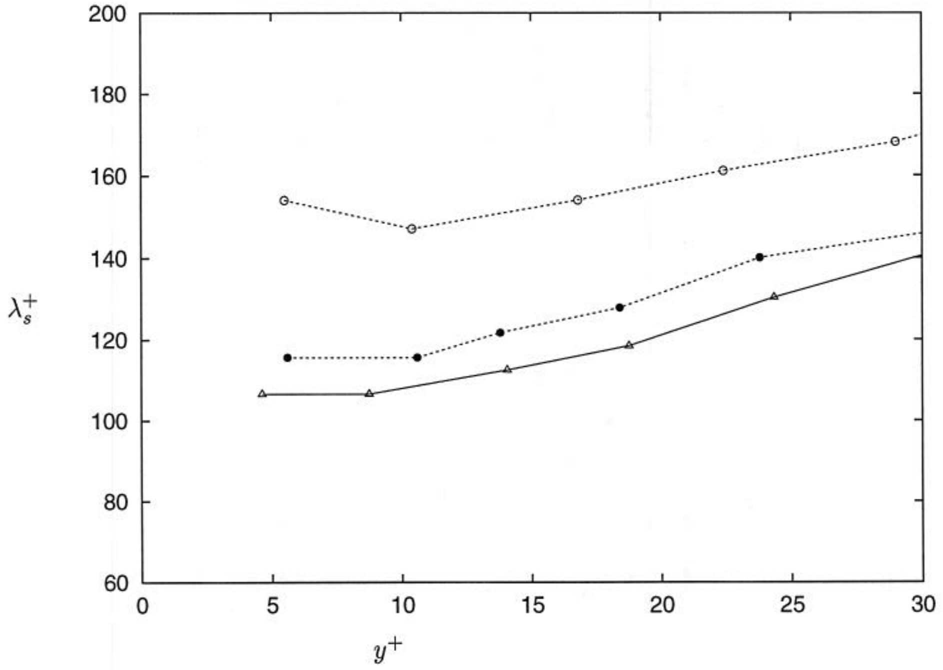

Figure 30: Spanwise spacing of streaks λ_s^+ (approximated by taking twice the spanwise separation at the minimum of R_{uu}) as a function of wall-distance. ∘ – bottom (porous) wall of *case 15*; • – top (impermeable) wall of *case 15*; $\triangle$ – impermeable *case 16*.

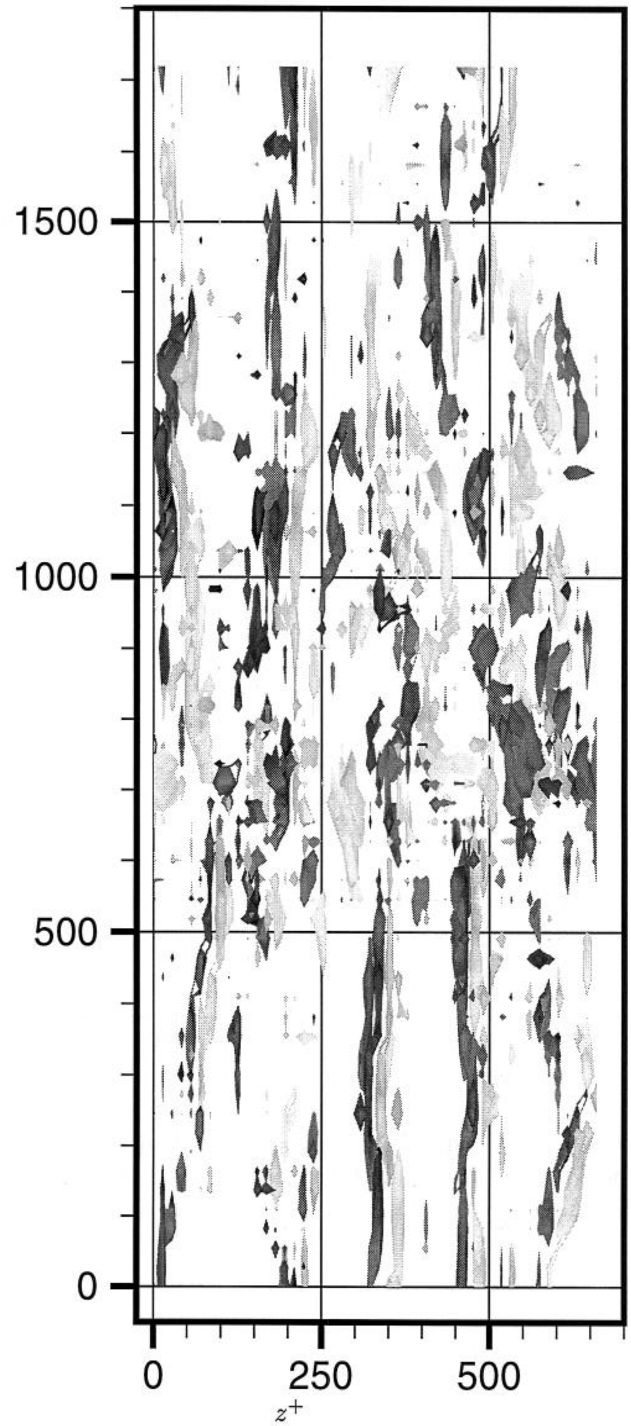

Figure 31: Isosurfaces of fluctuating vorticity $\omega_y' \, \nu / u_\tau^2 = \pm 0.2$ of an instantaneous field above the porous wall of *case 15*. The y-range (depth) shown extends up to the center of the channel. The negative value has dark shading, the positive a light shading. The view is into the wall and the mean flow is in positive x direction.

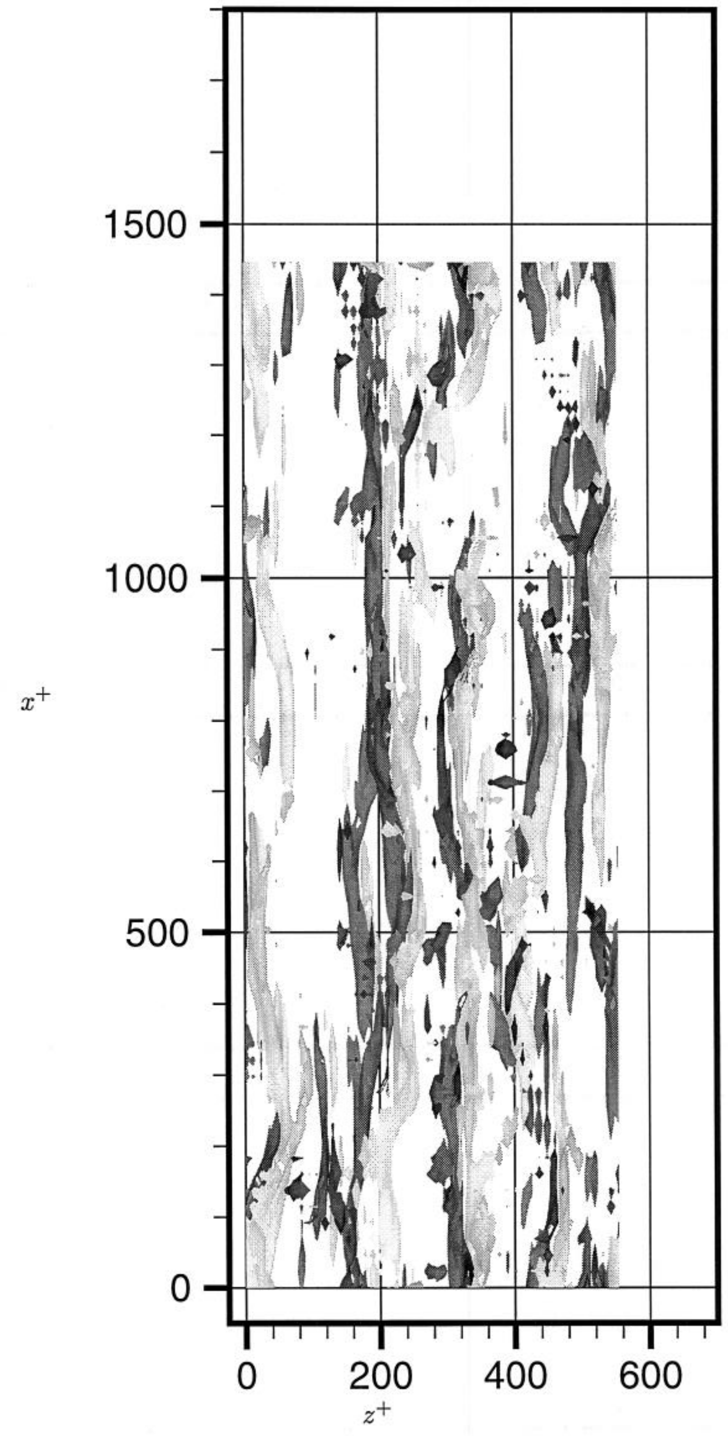

Figure 32: Isosurfaces of fluctuating vorticity $\omega_y' \nu / u_\tau^2 = \pm 0.2$ of an instantaneous field of the impermeable *case 16*. The y-range (depth) shown extends up to the center of the channel. The negative value has dark shading, the positive a light shading. The view is into the wall and the mean flow is in positive x direction.

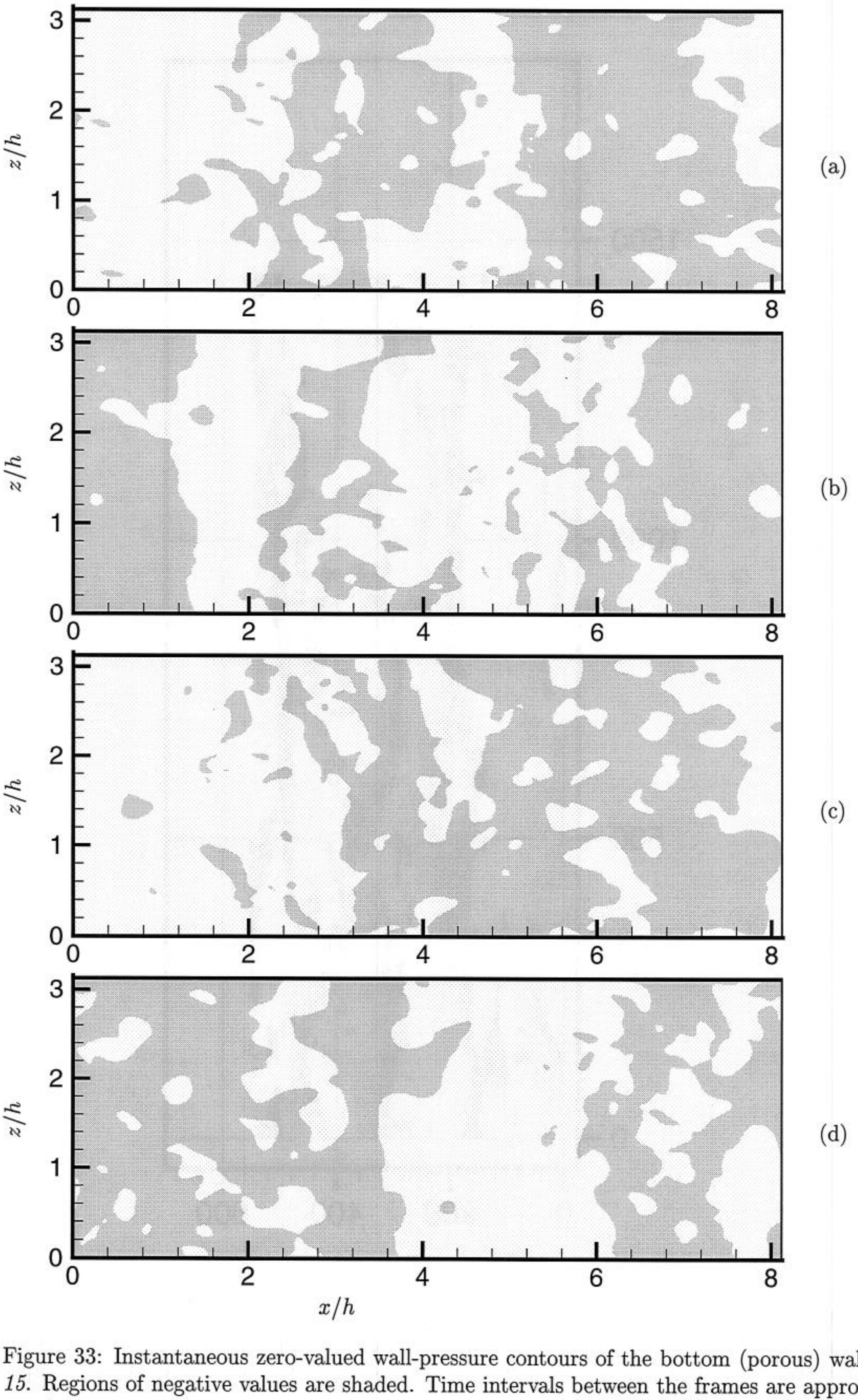

Figure 33: Instantaneous zero-valued wall-pressure contours of the bottom (porous) wall of *case 15*. Regions of negative values are shaded. Time intervals between the frames are approximately $30\,h/U_0$, advancing from (a) to (d). The mean flow is in positive x-direction.

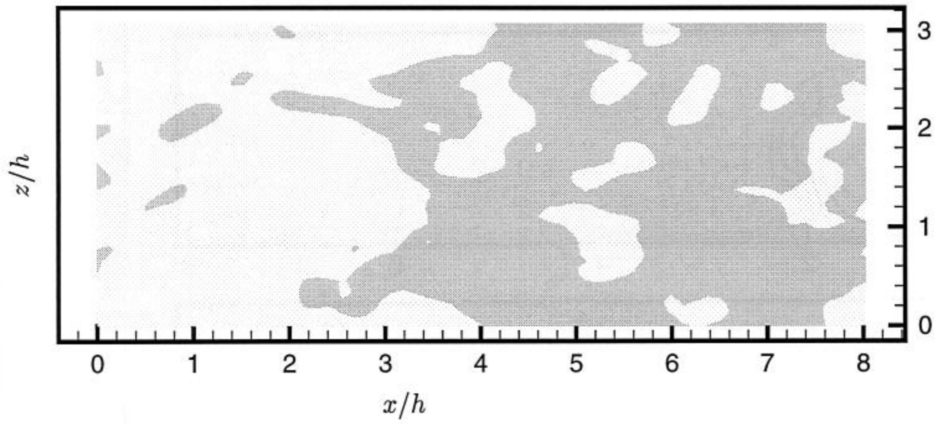

Figure 34: Instantaneous zero-valued wall-pressure contours of the top (impermeable) wall of *case 15*. Regions of negative values are shaded. The time corresponds to image (a) of figure 33. The mean flow is in positive x-direction.

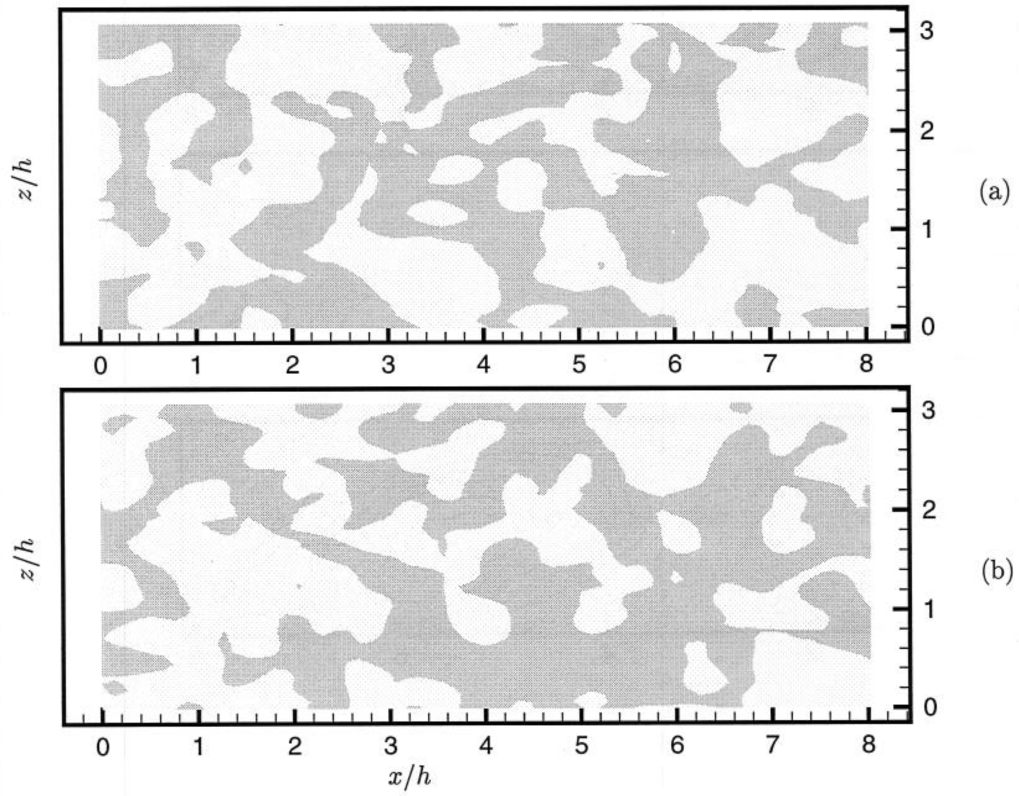

Figure 35: Instantaneous zero-valued wall-pressure contours of *case 16*. (a) bottom wall (b) top wall of the same flow field. Regions of negative values are shaded. The mean flow is in positive x-direction.

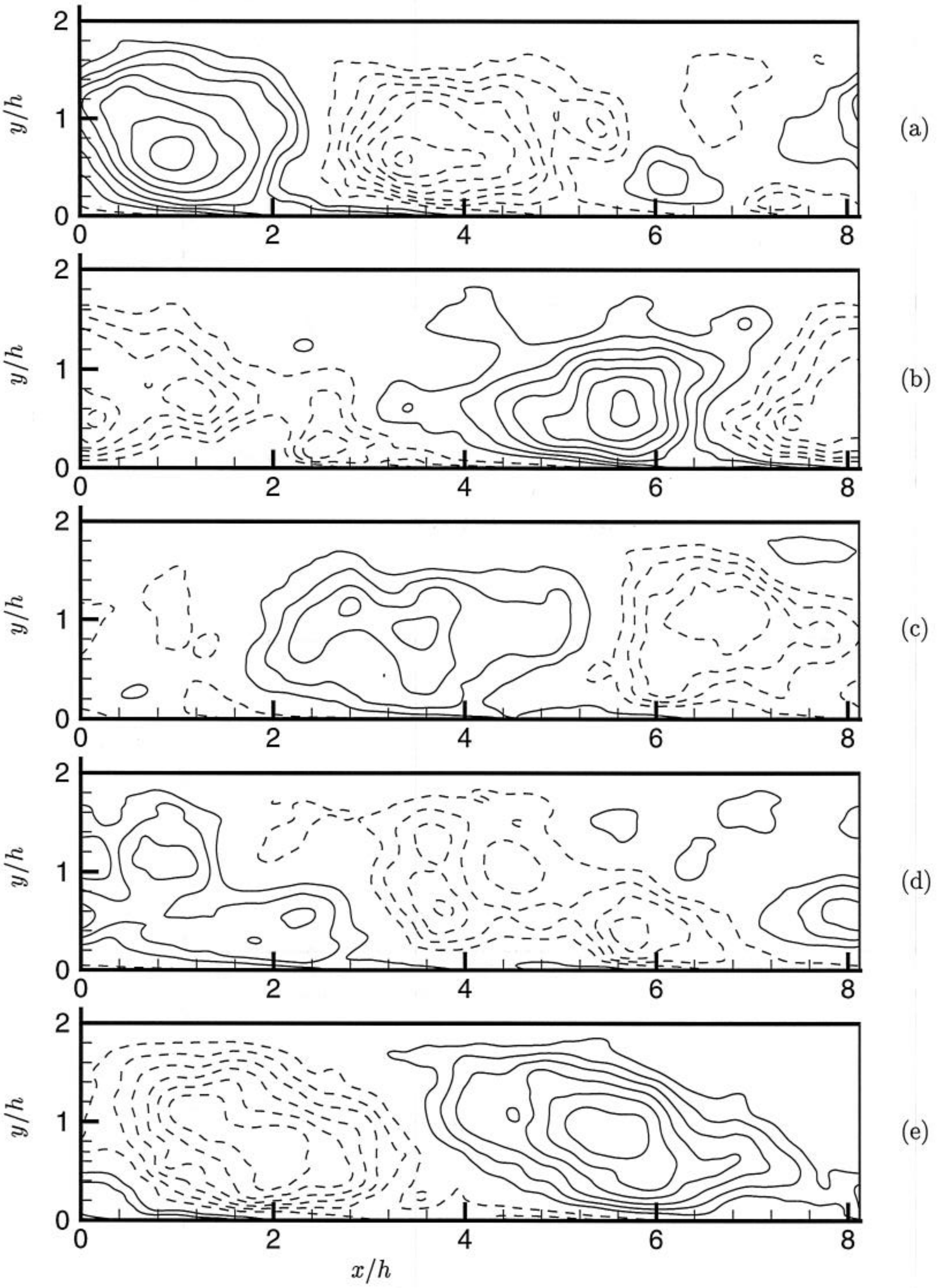

Figure 36: Instantaneous contours of the streamfunction of the fluctuations in (x, y)-plane of *case 15*. Isovalues are $\Psi = \pm\{0.035, 0.03, 0.025, 0.015, 0.01, 0.005\}$ where negative contours are dashed. Time intervals between the frames are approximately $30\,h/U_0$, advancing from (a) to (e). The mean flow is in positive x-direction.

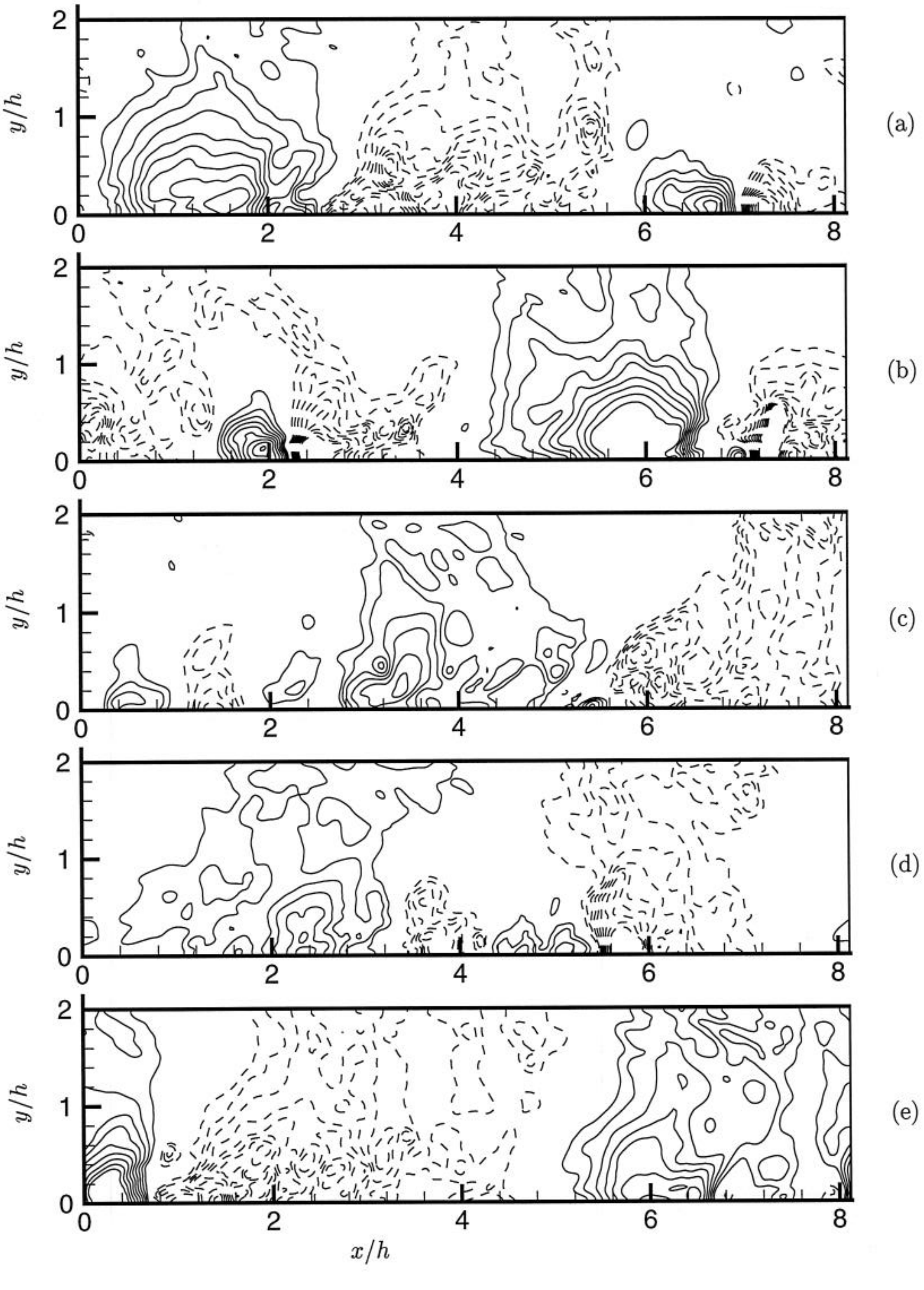

Figure 37: Instantaneous contours of the two-dimensional mode of the pressure fluctuations ((x, y)-plane) of *case 15*. Isovalues are $p'_{2D} = \pm\{0.02, 0.018, 0.016, 0.014, 0.012, 0.010, 0.008, 0.006, 0.004\}$ where negative contours are dashed. Time intervals between the frames are approximately $30\, h/U_0$, advancing from (a) to (e). The mean flow is in positive x-direction.

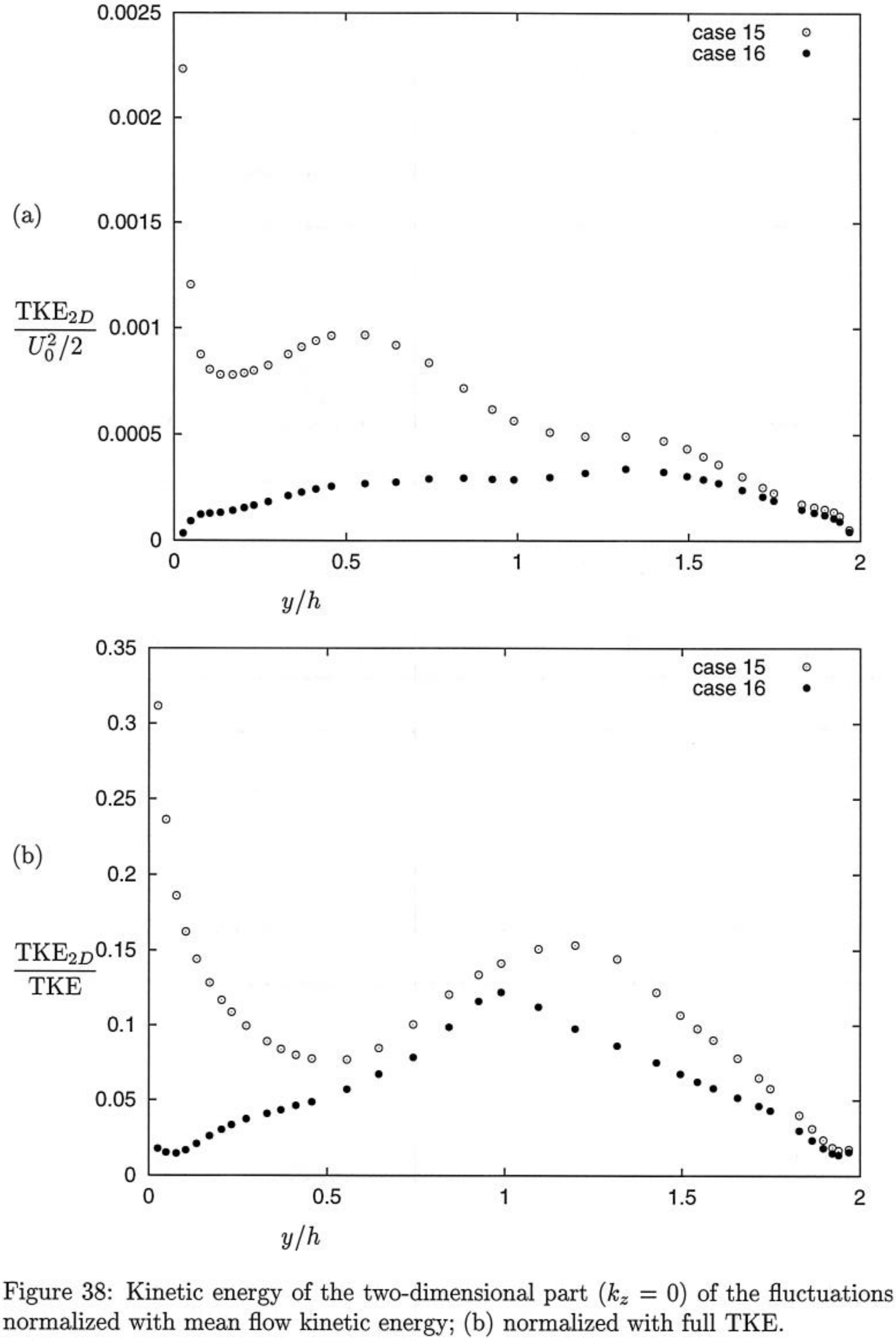

Figure 38: Kinetic energy of the two-dimensional part ($k_z = 0$) of the fluctuations TKE_{2D}. (a) normalized with mean flow kinetic energy; (b) normalized with full TKE.

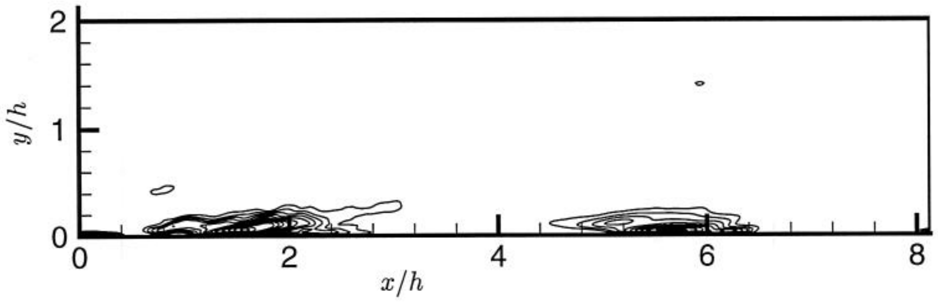

Figure 39: Instantaneous contours of the kinetic energy contained in the two-dimensional ($k_z = 0$) mode of *case 15.* Isovalues are $\mathrm{TKE}_{2D} = \{0.005, 0.008, 0.011, 0.014, 0.017, 0.02, 0.023, 0.026, 0.03, 0.033, 0.036\}$. The flow field corresponds to figures 36(e) and 37(e). The mean flow is in positive x-direction.

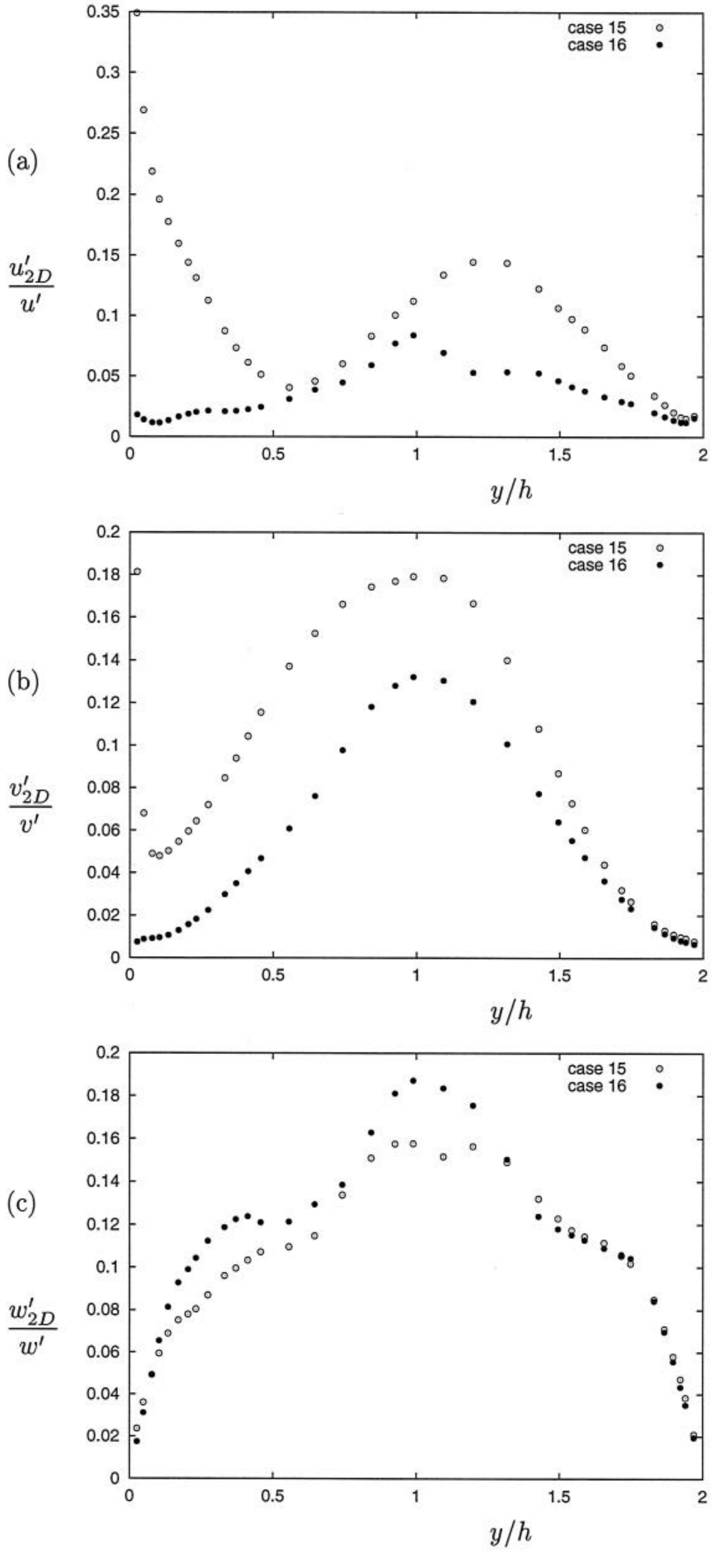

Figure 40: The *rms* value of the two-dimensional part ($k_z = 0$) of the fluctuations of velocity relative to the *rms* value of the full fluctuations. (a) streamwise component; (b) wall-normal component; (c) spanwise component.

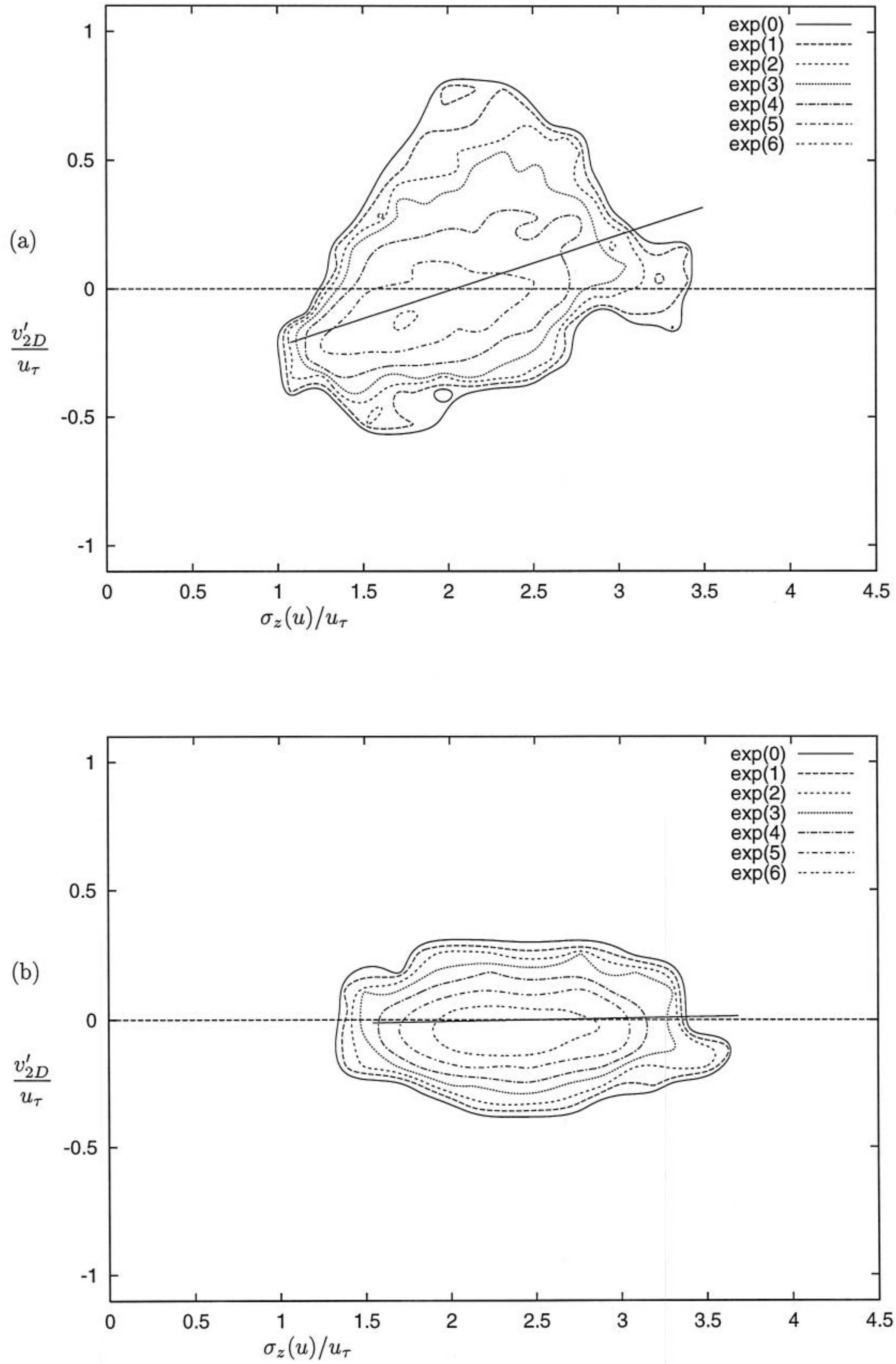

Figure 41: Histograms of the joint probability density function of vertical motion in the (x, y)-plane (measured by the $(k_z = 0)$-mode of wall-normal velocity v'_{2D}) and streak intensity (measured by the spanwise standard deviation of streamwise velocity $\sigma_z(u) = \left(\sum_{k=1}^{n_z}(u(x,y,z,t) - \overline{u}(x,y,t))^2/n_z\right)^{1/2}$). The data is accumulated in the range of wall distances $20 \leq y^+ \leq 30$. The straight line indicates the linear regression obtained by a least-squares fit of the data. (a) *case 15*; (b) *case 16.*

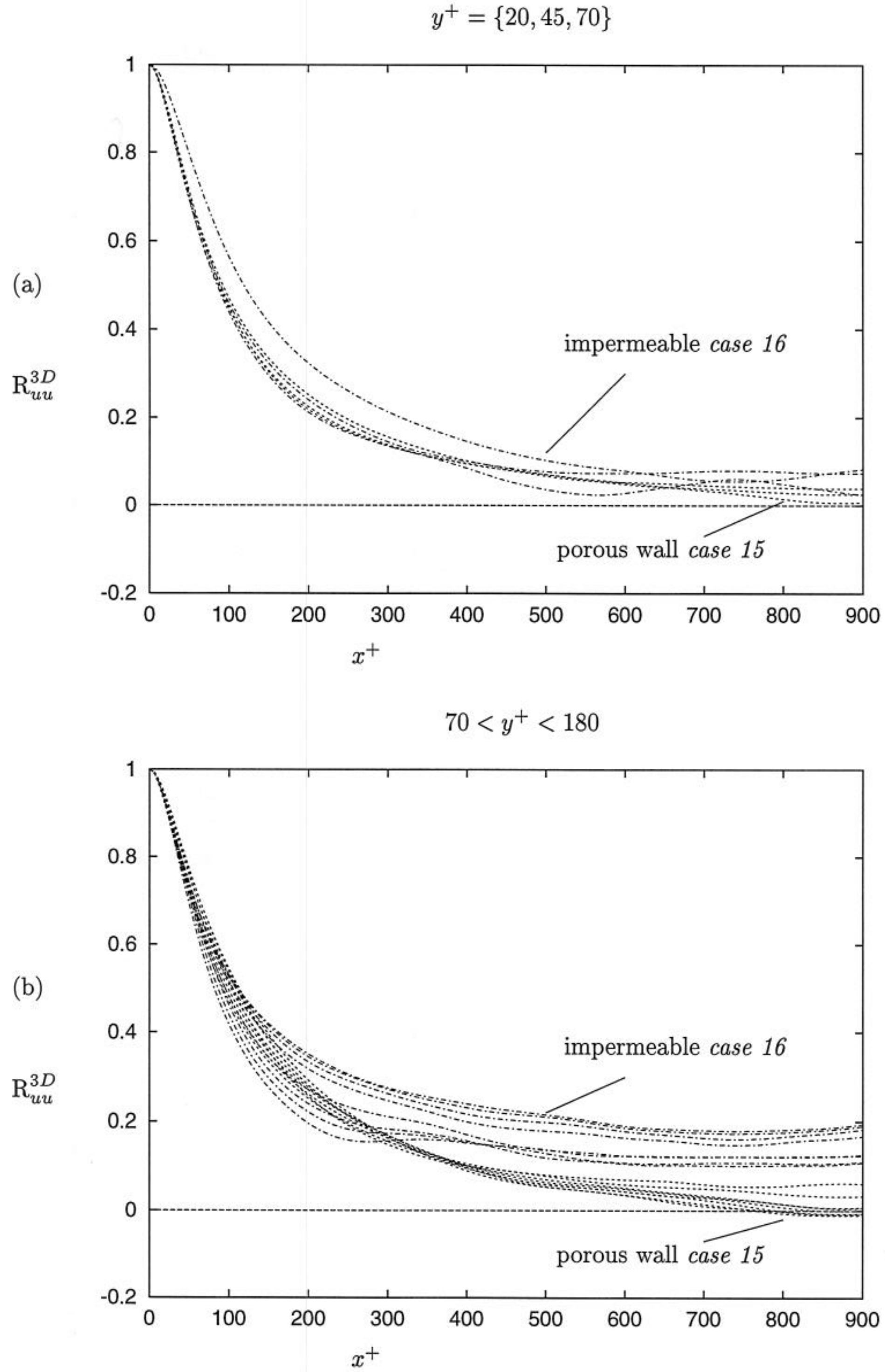

Figure 42: Time-averaged two-point autocorrelations of the modes of streamwise velocity for which $k_z > 0$. (a) Planes at $y^+ = \{20, 45, 70\}$; (b) Planes in the interval $70 \leq y^+ \leq 180$.

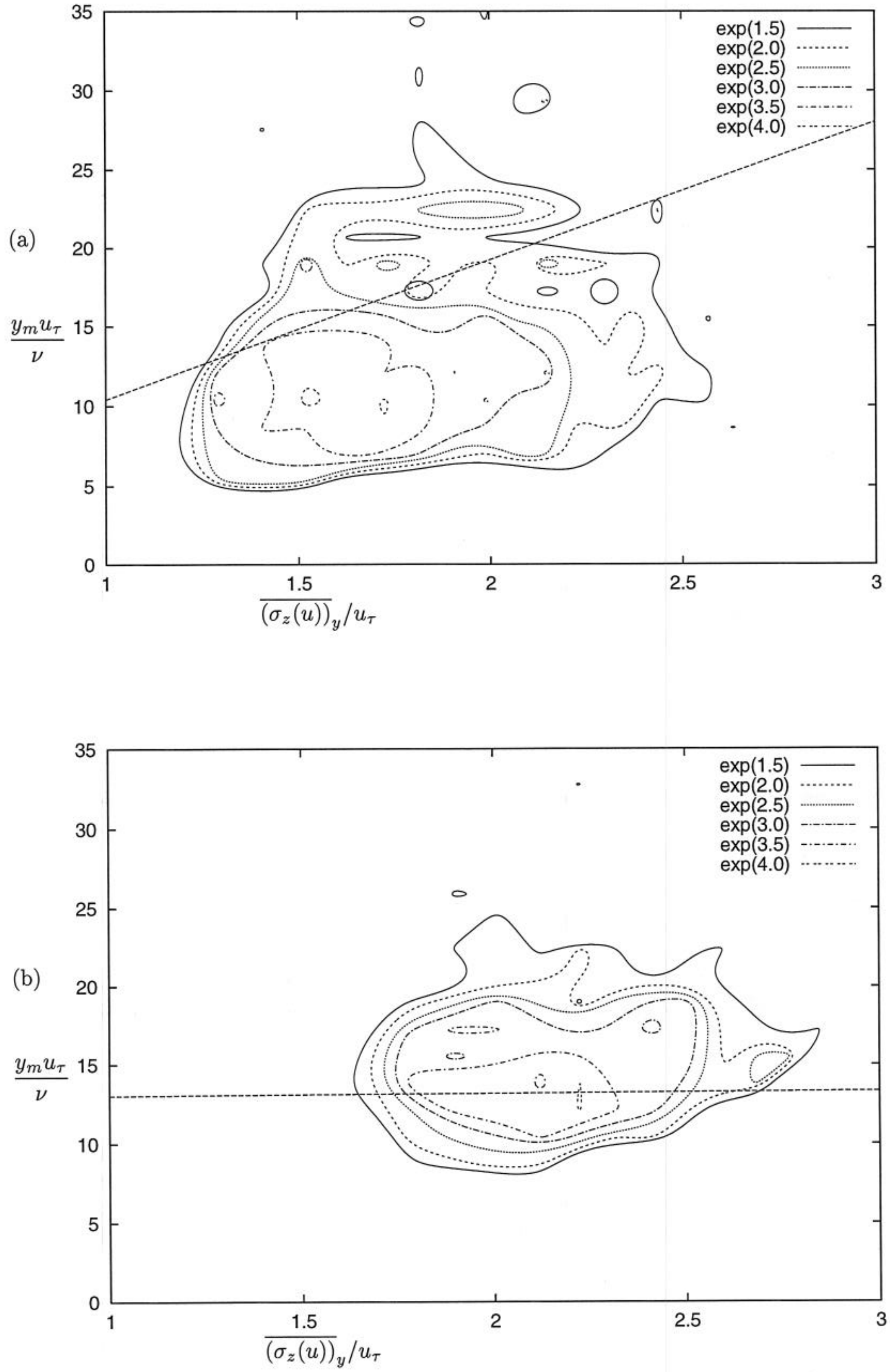

Figure 43: Histograms of the joint probability density function of streak height (measured by the wall-distance y_m of the maximum of spanwise averaged streak intensity at each streamwise station x_i of the grid) and corresponding wall-normal *rms* value of streak intensity $\overline{(\sigma_z(u))}_y$ as defined in Equ. (46)). The straight line indicates the linear regression of the data. (a) *case 15*; (b) *case 16*.

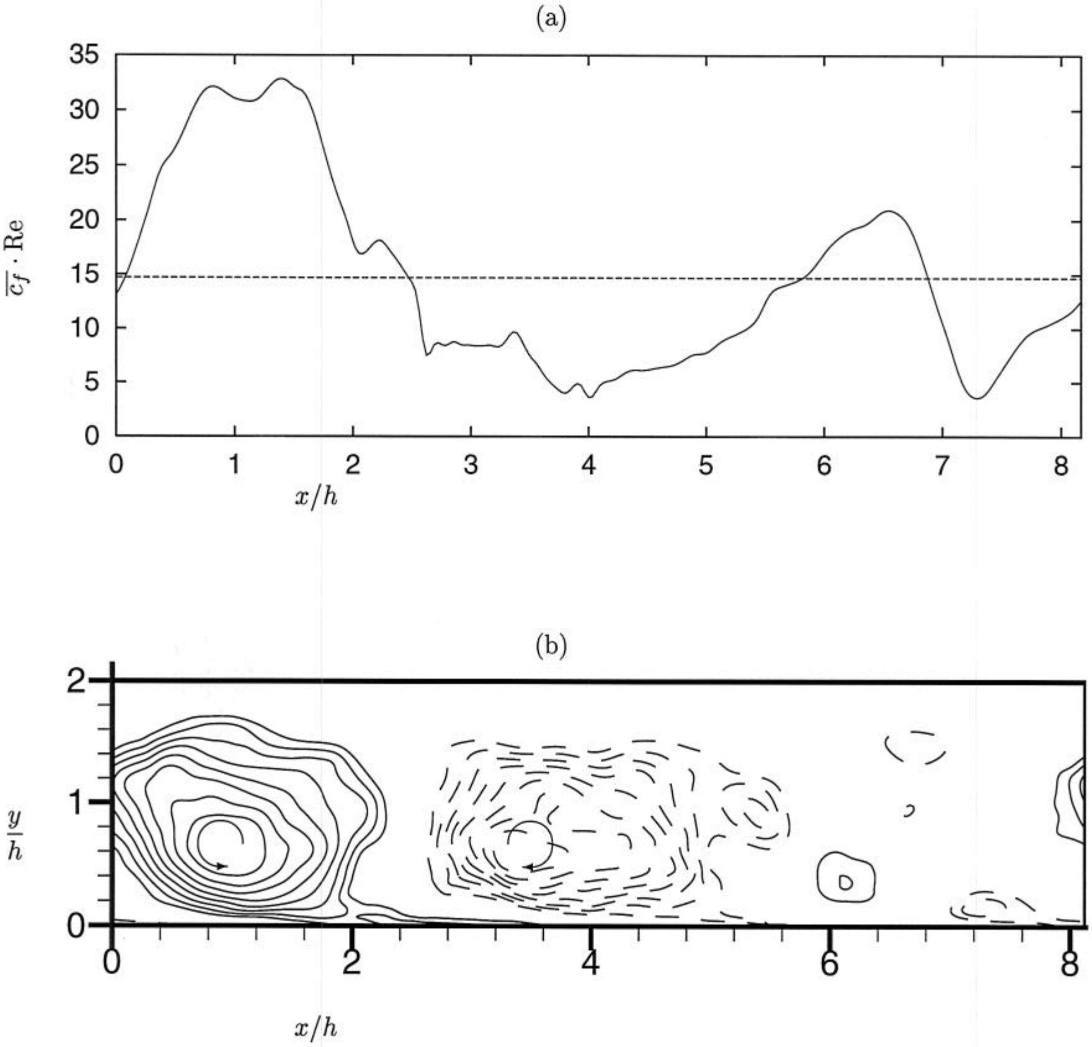

Figure 44: Influence of "rollers" on wall friction: instantaneous data of simulation *15*. (a) The spanwise-averaged skin friction on the lower (porous) wall as a function of the streamwise coordinate x. (b) Isovalues of the streamfunction of the $k_z = 0$ mode of fluctuating velocity, the arrows indicating the sense of rotation of the two large structures (negative contours are dashed).

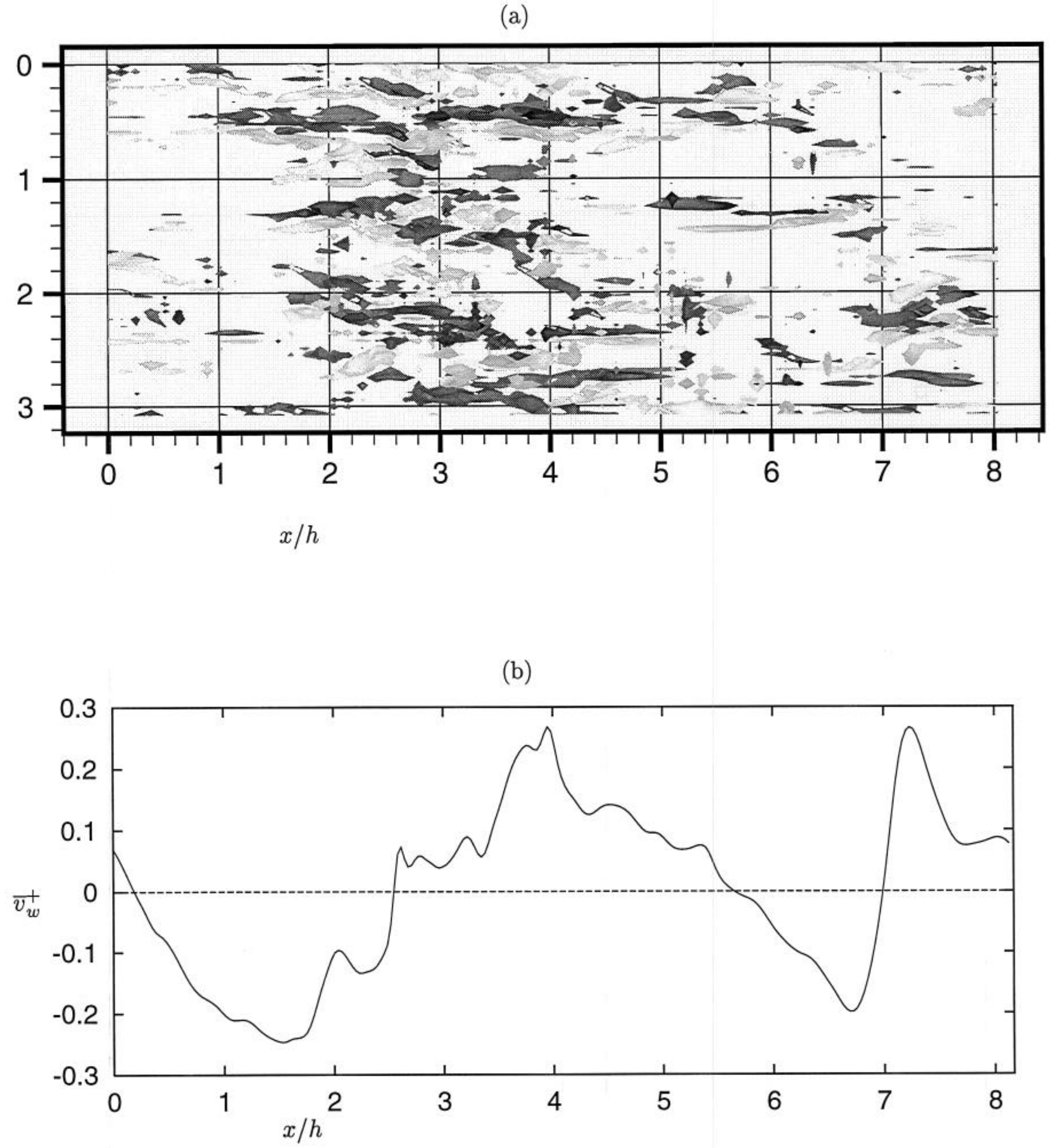

Figure 45: Effect of "rollers": instantaneous data of simulation *15* at the same moment as in figure 44. (a) Isosurfaces of fluctuating vorticity $\omega'_y \, \nu / u_\tau^2 = \pm 0.2$ above the lower (porous) wall of *case 15*. The y-range (depth) shown extends up to the center of the channel. The negative value has dark shading, the positive a light shading. The view is into the wall. (b) The spanwise-averaged wall transpiration of the lower (porous) wall as a function of the streamwise coordinate x.

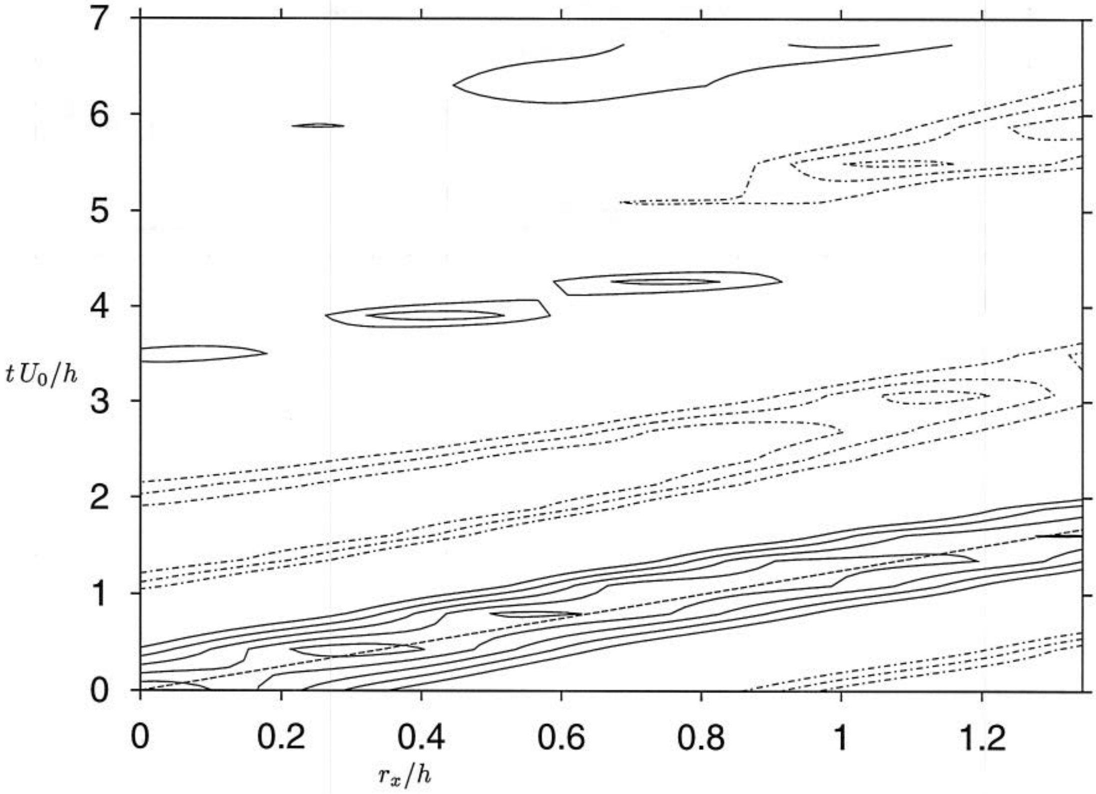

Figure 46: Isocontours of the streamwise space-time correlation of the $(k_z = 0)$-mode of streamwise velocity fluctuations at a wall-distance $y^+ = 30$ of *case 11* (small box, high porosity). Positive values $\{0.9, .7, .6, .5\}$ have solid lines, negative values $\{-.3, -.4, -.5\}$ are dashed. The straight line across the primary peak going through the origin has a slope of $1.25\,U_0$. This gives a phase velocity of $U_c/U_0 = 0.8$ which is equivalent to $U_c/u_\tau = 12.56$.

A Details related to b-splines

A.1 B-spline collocation derivatives

In the following we are exclusively concerned with approximations to first derivative expressions since the non-linear terms (4) of the governing equations do not involve higher order derivatives in the non-periodic direction y. Similar results, however, have been obtained for second derivatives in the framework of a boundary layer code.

A.1.1 The present spline base

Classic textbooks [32, 6] give the mathematical background on b-splines, which are here recalled to be piecewise polynomial functions that can be most conveniently defined by the following recursion formula:

$$B_j^o(y) = \frac{(y - t_{j-k-1})}{(t_{j-1} - t_{j-k-1})} B_{j-1}^{o-1}(y) + \frac{(t_j - y)}{(t_j - t_{j-k})} B_j^{o-1}(y) \quad j = 1 \ldots N \quad , \tag{48}$$

where $B_j^o(y)$ denotes the j-th b-spline of order o and $t = \{t_1, \ldots, t_{N+o}\}$ is a set of knot points which will determine completely the desired spline base. We note that a spline function of order o as defined in this context consists actually of polynomials of degree $o-1$. The number of necessary points for the construction of N splines of order o is $N + o$ since each spline has a support of $o + 1$ knots.

Let us consider a periodic b-spline base, i.e. the knot points t are equidistantly distributed at intervals $L_y/(N - o + 1)$ from $-(o - 1)L_y/(N - o + 1)$ to $L_y + (o - 1)L_y/(N - o + 1)$ (see figure 47).

A spline expansion of a variable $f(y)$ in terms of b-splines B_i^o,

$$f(y) \to s(y) = \sum_{i=1}^{N} \hat{s}_i \cdot B_i^o(y) \quad , \tag{49}$$

necessitates a transformation of N discrete functional values $f(y_j)$, $j = \{1 \ldots N\}$ to spline coefficients $\hat{s}_j$, $j = \{1 \ldots N\}$. As collocation points y_j for this transformation, we choose the $N + (2 - o)$ knot points that lie inside the domain $[0, L_y]$ and which we supplement by $(o - 2)$ additional points in the intervals $[t_k, t_{o+1}]$ and $[t_{N-o-1}, t_{N-o}]$ in order to obtain a closed and well-posed system of order N. Specifically in the case of (cubic) splines of order $o = 4$, which will be used in the following, we choose the 2 additional points to be located at the centre of the first and last interval, i.e. $y_2 = (t_4 + t_5)/2$ and $y_{N-1} = (t_N + t_{N-1})/2$ (see figure 47).

A.1.2 Cubic spline derivatives

Using the expansion (49), a b-spline derivative is given by the following expression:

$$s'(y) = \sum_{i=1}^{N} \hat{s}_i \cdot B_i'(y) \quad . \tag{50}$$

Since our collocation points $\{y_j\}$ in general coincide with the knots $\{t_i\}$, the collocation derivative can simply be expressed by

$$s'(y_j) = \sum_{i=1}^{N} \hat{s}_i \cdot B_i'(y_j) = \frac{1}{2h}\left[\hat{s}_{j+1} - \hat{s}_{j-1}\right] , \qquad h = L_y/(N - o + 1) \quad . \tag{51}$$

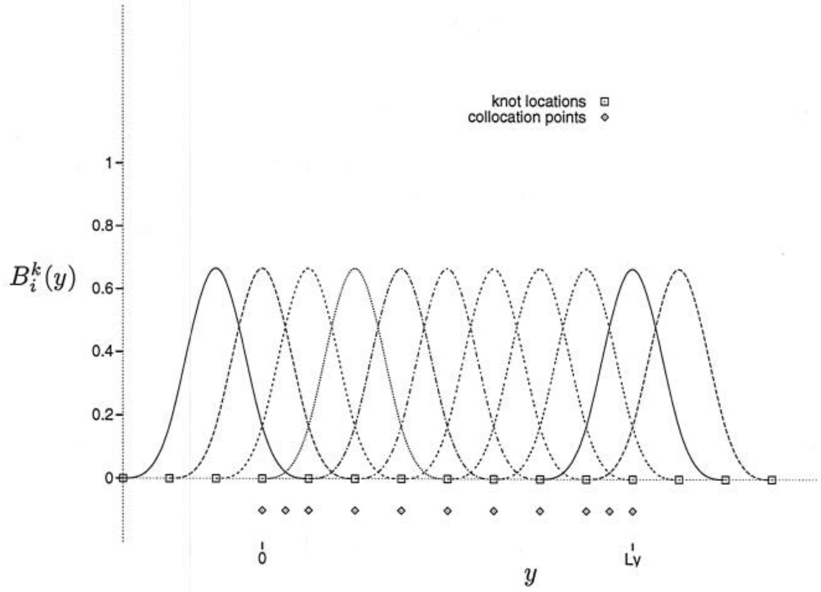

Figure 47: Example of a spline base consisting of $N = 11$ b-splines of order $o = 4$ constructed on 15 equidistant knots over the interval $[-3L_y/(N-3), L_y + 3L_y/(N-3)]$. Also indicated are the corresponding locations of the collocation points used in the variable transformation.

The following cubic spline identity will be needed [25]:

$$s'_{i-1} + 4\, s'_i + s'_{i+1} \;=\; \frac{3}{h}\left[s_{i+1} - s_{i-1}\right] \quad . \tag{52}$$

It will be useful in the following to resort to the formalism of difference operators and their calculus (e.g. [9]). Denoting $E = e^{hD}$ the displacement operator, where D is the forward difference operator, we can express the spline collocation derivative (52) as:

$$s'_i \;=\; \underbrace{\frac{3}{h}\left(e^{hD} - e^{-hD}\right)\left(e^{-hD} + 4\,I + e^{hD}\right)^{-1}}_{\mathcal{D}} \, f_i \quad . \tag{53}$$

Note that the right hand side is expressed in terms of the functional values f_i since the b-spline expansion (49) is an exact representation at the collocation locations, i.e. $s(y_i) = f(y_i)$. A Taylor series expansion of (53) gives the following expression for the accuracy of the numerical derivative:

$$s'_i \;=\; f'_i \;-\; \frac{h^4}{180}\, f^v_i \;+\; \mathcal{O}(h^6) \quad . \tag{54}$$

A.1.3 Raising the formal accuracy by an explicit stencil

We will follow the ideas of Lucas [25] and Houstis *et al.* [10] and apply an explicit stencil to the spline representation of the first derivative with the aim of cancelling the formal truncation error up to a predetermined order.

Posing a stencil over five indices,

$$\widetilde{s}'_i \;=\; a \cdot s'_{i-2} \;+\; b \cdot s'_{i-1} \;+\; c \cdot s'_i \;+\; d \cdot s'_{i+1} \;+\; g \cdot s'_{i+2} \quad , \tag{55}$$

we can calculate the accuracy of this operator by formally expanding the following expression

$$\underbrace{\left(a \cdot e^{-2hD} \;+\; b \cdot e^{-hD} \;+\; c\,I \;+\; d \cdot e^{hD} \;+\; g \cdot e^{2hD}\right)}_{\mathcal{S}} \cdot s'_i \quad , \tag{56}$$

while substituting (53). Solving for the coefficients $\{a \dots g\}$, requiring all terms of the expansion to disappear up to fifth order, gives:

$$a = g = 1/180\,, \quad b = d = -4/180\,, \quad c = 186/180\,, \tag{57}$$

so that the approximation becomes

$$\tilde{s}'_i \;=\; f'_i + \frac{f_i^{vii}}{630}\,h^6 \;+\; \mathcal{O}(h^{10}) \quad . \tag{58}$$

We can now summarize the three operations necessary to obtain the numerical derivative in a manner consistent with the notation of the main body of this report (i.e. (13)):

$$\partial_y\, \boldsymbol{f}(y) \;\rightarrow\; \boldsymbol{f}^S \;=\; \mathcal{S}\cdot\mathcal{D}\cdot\mathcal{C}^{-1}\cdot \boldsymbol{f} \quad , \tag{59}$$

where $\mathcal{C}^{-1}$ denotes the inverse of the collocation matrix, representing the transformation into spline space (49). This latter operation necessitates inverting the tridiagonal collocation matrix. The two remaining operators are explicit and thus performed at low computational cost.

A.1.4 Resolution characteristics of the numerical derivative

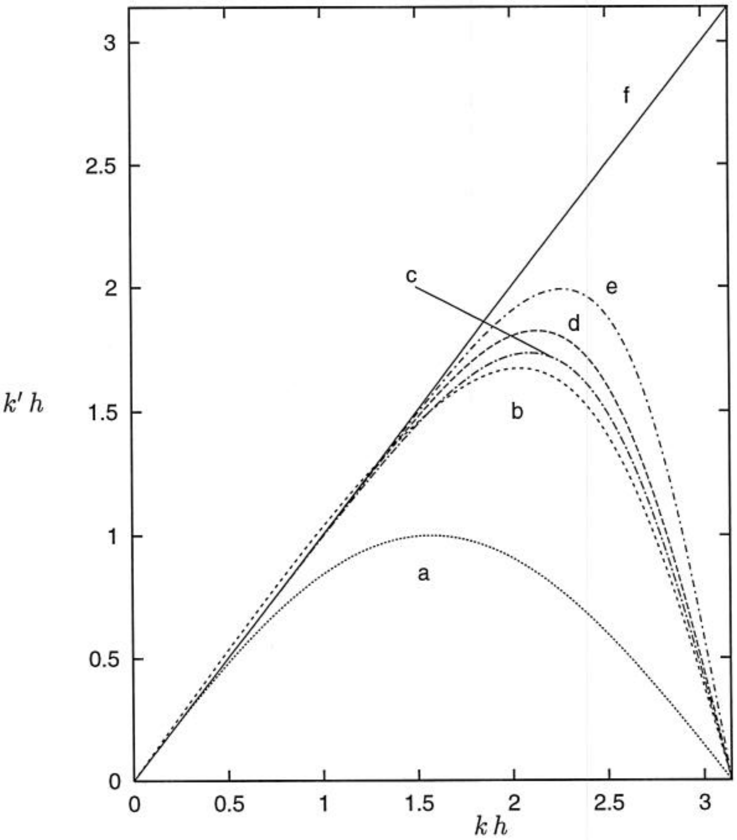

Figure 48: Modified wavenumber as a function of the wavenumber for the approximation of the first derivative. (a) second order central finite difference scheme, (b) fourth order Padé scheme, (c) cubic spline derivative (fourth order), (d) cubic splines with explicit sixth-order stencil, (e) sixth-order tridiagonal compact finite difference scheme, (f) exact value.

In order to estimate the error introduced by the above numerical approximation to the first derivative, we present a Fourier analysis of the differencing errors in this section (e.g. [23, 26]). We consider a periodic domain of length 2π, using N uniformly distributed collocation points. A discrete test function $f_j = e^{iky_j}$ has the analytic derivative $f'_j = ike^{iky_j}$, while the numeric representation bears some error that can be interpreted as a modified wavenumber k', viz.

$$f'_{num} = ik'e^{iky_j} \quad . \tag{60}$$

The modified wavenumber is thus simply defined by

$$k' = \frac{f'_{num}}{i\, f_j} \quad . \tag{61}$$

Inserting the difference operator and expressing the exponentials by means of trigonometric functions gives for the cubic spline derivative (53):

$$k'\, h = \frac{3\, \sin(kh)}{\cos(kh) + 2} \quad , \tag{62}$$

and for the sixth order formula (55):

$$k'\, h = \frac{\sin(kh)\,(\cos(2kh) - 4\cos(kh) + 93)}{30\,(\cos(kh) + 2)} \quad . \tag{63}$$

Figure 48 shows the modified wavenumber as a function of the exact wavenumber over the range of all resolvable scales. The exact differentiation – indicated by the line of slope unity – corresponds to a spectral scheme. The explicit stencil is seen to reduce the differencing error of the cubic splines throughout the spectrum. Also included are several pure finite difference schemes at similar computational cost. The tridiagonal compact finite difference scheme with highest formal accuracy $\mathcal{O}(h^6)$ [23] has a lower error than the present method and might thus be preferable from the mere point of view of the present analysis of a periodic wave-type function. The result can more conveniently be quantified by defining a maximum "well" resolved wavenumber k_{max} for a given error tolerance ϵ, viz.

$$k_{max} \quad \backslash \quad \left| \frac{k'(k_{max}) - k_{max}}{k_{max}} \right| \leq \epsilon \quad , \tag{64}$$

such that $e = k_{max}/\pi$ signifies the *resolving efficiency.* The corresponding values for the numerical schemes in the figure are given in table 2.

scheme	$\epsilon = .1$	$\epsilon = .01$	$\epsilon = .001$
(a)	.250	.080	.020
(b)	.590	.350	.200
(c)	.594	.355	.205
(d)	.636	.435	.294
(e)	.701	.502	.351

Table 2: Values of the resolving efficiency e as a function of the tolerance ϵ for different numerical representations of the first derivative. Labels as in figure 48

A.1.5 Explicit finite difference formulas for the boundary nodes

The above outlined differentiation can only be carried out in the interior of the domain, while at the boundary, one-sided formulas need to be applied. This leads us to two tasks:

- Calculate derivative values directly by an explicit finite difference formula of desired (sixth) order at nodes where the above stencil cannot be applied. Those include the collocation points $\{y_1 \dots y_3\}$ and $\{y_{N-2} \dots y_N\}$ (note that $\{y_2, y_{N-1}\}$ are the intermediate points, figure 47). Furthermore, we need to provide a difference value at two supplementary points $\{y_{3/4}, y_{N-3/4}\}$ which are utilized in the Galerkin part of the current method where a spline base of order $o=6$ is employed. If we define the one-sided stencil as follows

$$\widetilde{s}'_j = \frac{1}{h} \sum_{l=1}^{7} c_l \cdot f(y_l) \quad , \tag{65}$$

and stress that these collocation points y_l now are

$$y_l = \{0, \frac{1}{2}h, \frac{3}{4}h, h, 2h, \dots, L_y - h, L_y - \frac{3}{4}h, L_y - \frac{1}{2}h, L_y\} \quad , \tag{66}$$

we can give the coefficients and the respective truncation errors

$$\widetilde{s}'_j = f'_j + \alpha f_j^{vii} h^6 + \mathcal{O}(h^7) \quad , \tag{67}$$

in the following table:

collocation point	c_1	c_2	c_3	c_4	c_5	c_6	c_7	α
y_1	$-\frac{65}{12}$	$\frac{768}{35}$	$-\frac{16384}{585}$	12	$-\frac{3}{5}$	$\frac{4}{45}$	$-\frac{3}{364}$	$-\frac{1}{560}$
y_2	$-\frac{35}{192}$	$-\frac{562}{105}$	$\frac{896}{117}$	$-\frac{35}{16}$	$\frac{7}{96}$	$-\frac{7}{720}$	$\frac{5}{5824}$	$\frac{1}{6144}$
y_3	$\frac{65}{1024}$	$-\frac{117}{56}$	$-\frac{128}{585}$	$\frac{585}{256}$	$-\frac{117}{2560}$	$\frac{13}{2304}$	$-\frac{45}{93184}$	$-\frac{39}{458752}$
y_4	$-\frac{1}{12}$	$\frac{64}{35}$	$-\frac{4096}{585}$	$\frac{31}{6}$	$\frac{1}{10}$	$-\frac{1}{90}$	$\frac{1}{1092}$	$\frac{1}{6720}$

We note that the sign of the coefficients c_l is inverted at the other boundary of the domain.

- Since the sixth-order stencil (56) is based upon an exact cancellation of the fourth-order truncation error (54), we have to assure that the boundary nodes $\{y_1, y_N\}$ carry exactly the same error as the interior nodes if the final scheme is to be of sixth-order throughout. This fact is not satisfied by the direct cubic spline derivation (53) because of the intermediate points that are used in the transformation (49). This means that the entries of the first row of the collocation matrix $\mathcal{C}$ have to be modified to read now

$$\mathcal{C}_{1m} = \left[\frac{220}{123}, -\frac{743}{246}, \frac{602}{123}, -\frac{175}{41}, \frac{238}{123}, -\frac{28}{123}, -\frac{6}{41}, \frac{11}{246}, 0, \dots, 0\right] \tag{68}$$

instead of

$$\mathcal{C}_{1m} = \left[\frac{1}{6}, \frac{2}{3}, \frac{1}{3}, 0, \dots, 0\right] \tag{69}$$

The last row has the same entries, but in reverse order ($\mathcal{C}_{Nm} = \mathcal{C}_{1(N-m)}$).

A.1.6 Analytical grid mapping

In order to increase the spatial resolution in the regions of high gradients we accumulate knot points near the wall locations at the extremas. The advantage of an analytical mapping function is that in a collocation method the chain rule can be used to obtain gradients of flow variables, effectuating numerical differentiation simply on equidistant mesh. Let $g(\xi) \rightarrow y$ be a proper variable transformation from computational ξ to geometrical y space, then we can express a derivative with respect to y as follows:

$$\frac{\partial \phi(y)}{\partial y} = \frac{\partial \phi(y)}{\partial \xi} \cdot \frac{\partial \xi}{\partial y} \quad , \tag{70}$$

expressing that the function ϕ is evaluated in y-space (i.e. its discrete values are at locations y_j), but the differentiation is carried out with respect to ξ-space and corrected by the analytic term $\partial\xi/\partial y$. We thus construct the equidistant grid – as mentioned above – in computational ξ-space and use a hyperbolic tangent function $g(\xi)$ to obtain locations in geometrical space y:

$$g(\xi) = 1 + \frac{\tanh(2\alpha(\xi-1)\pi)}{\tanh(2\alpha\pi)} \qquad 0 \le \xi \le 2 \quad . \tag{71}$$

The parameter α has been set to 0.3 in the present work, giving a stretching ratio $\Delta x_{max} / \Delta x_{min} \approx 11$.

A.2 B-spline Galerkin method

In order to achieve the desired sixth-order accuracy in the non-periodic direction of the overall method, we resort to b-splines of order $o{=}6$ in the Galerkin part of our discretization. Here, we use the technique of multiple knots at the extrema [6] while constructing the spline base. As can be seen from figure 49, o coinciding knot points are accumulated at each boundary giving rise to modified spline shapes in the vicinity. This fact leads to a simplified treatment of boundary conditions since the support of the base is very localized there: only one spline value is non-zero on the boundary, two first derivatives, three second derivatives, etc. As already mentioned above, the transformation of a function from physical to b-spline space is performed using N collocation points, out of which $N+(2-o)$ coincide with the knot point locations and the 4 missing ones are the following 1/2 and 3/4 points within the first and last interior intervals: $x_{2,3} = \{(t_6+t_7)/2, 3(t_7-t_6)/4+t_6\}$ and $x_{N-2,N-1} = \{t_{N-1}+(t_N-t_{N-1})/4, (t_N+t_{N-1})/2\}$ (see figure 49). The equidistant b-spline base is transformed into non-uniform space y via the transformation (71). The mass and stiffness matrix $\mathbf{M}$ and $\mathbf{K}$ (equation (22)) can now be evaluated by 6 point Gauss quadrature (e.g. [1, p.916]) using the recursion formula (48).

A.2.1 Resolution characteristics of the numerical derivative

Calculating an nth derivative $g \equiv \partial^n f/\partial y^n$ by means of a Galerkin MWR can be expressed as follows:

$$\sum_j \int \hat{g}_j \, B_j(y) \, B_i(y) \, \mathrm{d}y = \sum_j \int \hat{f}_j \, B_j^{(n)}(y) \, B_i(y) \, \mathrm{d}y \quad , \tag{72}$$

leading to the following operator form

$$\boldsymbol{g} = \left[\mathcal{C} \cdot \mathbf{M}^{-1} \cdot \mathbf{D}^{(n)} \cdot \mathcal{C}^{-1} \right] \boldsymbol{f} \quad , \tag{73}$$

where $\mathbf{D}^{(n)} = \int B_j^{(n)} B_j \mathrm{d}y$. In order to perform a modified wave number analysis of the differencing approximation as in section A.1.4, the eigenvalues of the full operator have to be determined. Considering again a wave-type test function $f_j = e^{iky_j}$ on a periodic domain, the individual

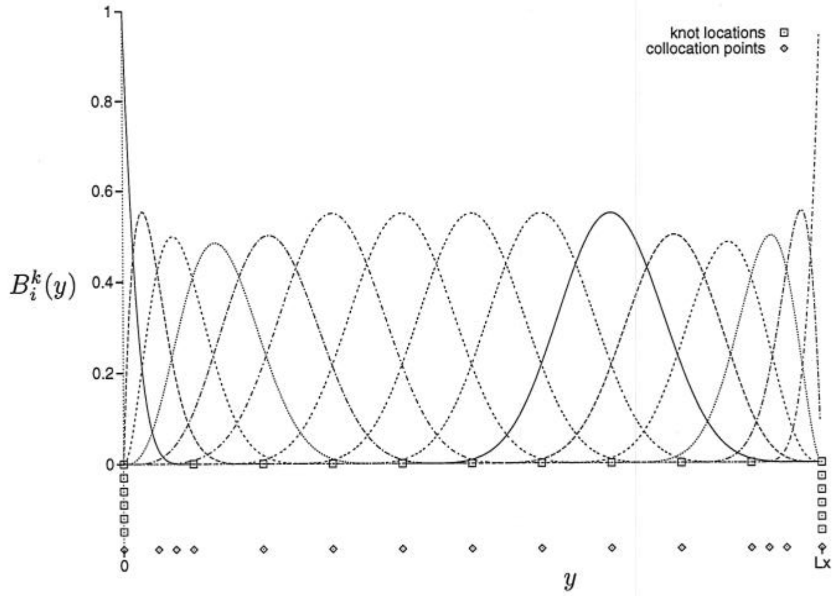

Figure 49: Example of a spline base consisting of 15 b-splines of order $k = 6$ constructed on 21 equidistant knots with multiplicty 6 on the extremas. Also indicated are the corresponding locations of the collocation points for variable transformation.

matrices of the operator in (73) are circulant. Each line thus has an equivalent eigenvalue and furthermore we have

$$\lambda\left(\mathcal{C}\cdot\mathbf{M}^{-1}\cdot\mathbf{D}^{(n)}\cdot\mathcal{C}^{-1}\right) = \frac{\lambda(\mathbf{D}^{(n)})}{\lambda(\mathbf{M})} \quad . \tag{74}$$

The projection upon the test function can then be used to determine the individual eigenvalues, viz.

$$(\mathbf{M}-\mathbf{I}\,\lambda)\,e^{iky_j} = 0 \quad , \tag{75}$$

such that for our 11-banded matrices

$$\lambda = \sum_{l=-5}^{5} \mathbf{M}_{(j,j+l)}\cdot e^{likh} \quad . \tag{76}$$

We obtain the following results:

$$\begin{aligned}
\lambda(\mathbf{M}) \quad &= \quad \tfrac{1}{19958400}\,h\cos(5\,kh) + \tfrac{509}{4989600}\,h\cos(4\,kh) + \tfrac{50879}{6652800}\,h\cos(3\,kh) + \tfrac{1093}{9900}\,h\cos(2\,kh) \\
&\qquad + \tfrac{1623019}{3326400}\,h\cos(kh) + \tfrac{655177}{1663200}\,h \\
\lambda(\mathbf{D}^{(1)}) \quad &= \quad \tfrac{1}{1814400}\,i\sin(5\,kh) + \tfrac{253}{453600}\,i\sin(4\,kh) + \tfrac{5203}{201600}\,i\sin(3\,kh) + \tfrac{16973}{75600}\,i\sin(2\,kh) \\
&\qquad + \tfrac{6787}{14400}\,i\sin(kh) \\
\lambda(\mathbf{D}^{(2)}) \quad &= \quad \tfrac{1}{181440h}\,(\cos(5\,kh) + 500\,\cos(4\,kh) + 13605\,\cos(3\,kh) + 59520\,\cos(2\,kh) \\
&\qquad - 5670\,\cos(kh) - 67956)\ .
\end{aligned} \tag{77}$$

Recalling that the modified wavenumber of the numerical approximation – for the first and second derivative respectively – is defined as

$$k' = \frac{\lambda(\mathcal{C} \cdot \mathbf{M}^{-1} \cdot \mathbf{D}^{(1)} \cdot \mathcal{C}^{-1})}{i}, \qquad k''^2 = -\lambda(\mathcal{C} \cdot \mathbf{M}^{-1} \cdot \mathbf{D}^{(2)} \cdot \mathcal{C}^{-1}) \quad , \tag{78}$$

the results for the sixth-order b-spline Galerkin method are the following:

$$\begin{aligned} k'\,h &= 11\,\frac{\sin(5\,kh)+1012\,\sin(4\,kh)+46827\,\sin(3\,kh)+407352\,\sin(2\,kh)+855162\,\sin(kh)}{\cos(5\,kh)+2036\,\cos(4\,kh)+152637\,\cos(3\,kh)+2203488\,\cos(2\,kh)+9738114\,\cos(kh)+7862124} \\ k''^2\,h^2 &= -110\,\frac{\cos(5\,kh)+500\,\cos(4\,kh)+13605\,\cos(3\,kh)+59520\,\cos(2\,kh)-5670\,\cos(kh)-67956}{\cos(5\,kh)+2036\,\cos(4\,kh)+152637\,\cos(3\,kh)+2203488\,\cos(2\,kh)+9738114\,\cos(kh)+7862124}\,. \end{aligned} \tag{79}$$

Figure 50 shows the modified wavenumber as a function of wavenumber. For our present purposes, the second derivative is of particular interest. The resolving efficiency of this scheme is quite high as can be appreciated quantitatively from table 3.

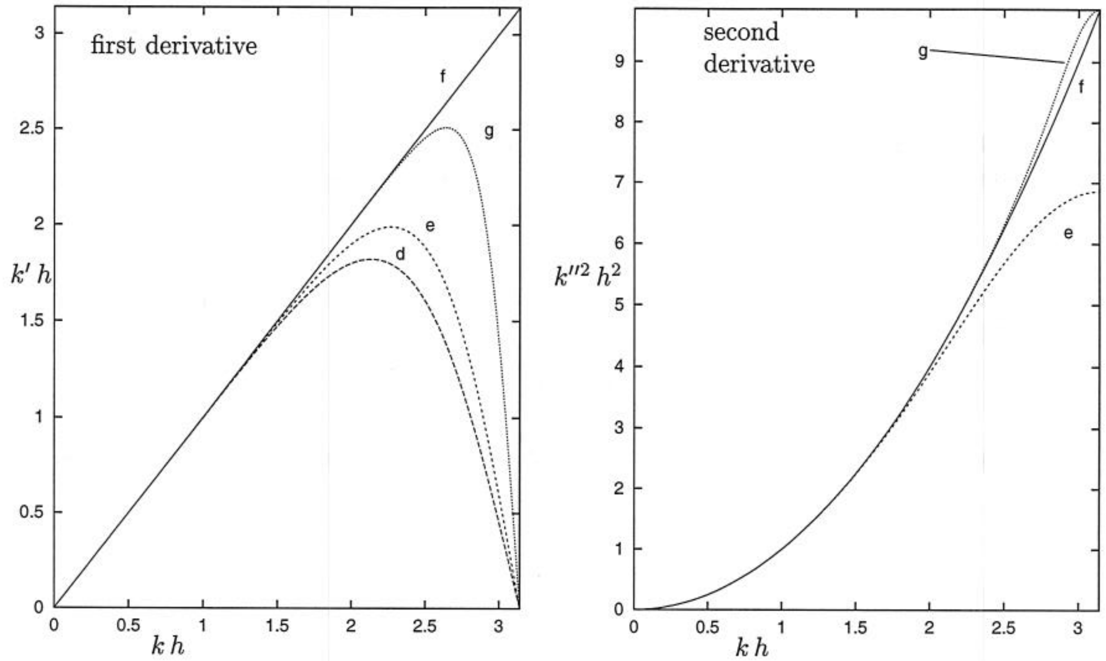

Figure 50: Modified wavenumber as a function of the wavenumber for the approximation of the first and second derivative. (d) cubic spline collocation method with explicit sixth-order stencil, (e) sixth-order tridiagonal compact finite difference scheme, (f) exact value, (g) sixth-order Galerkin method.

scheme	$\epsilon = .1$	$\epsilon = .01$	$\epsilon = .001$
(g)	1.000	.803	.682

Table 3: Resolving efficiency e as a function of the tolerance ϵ for the sixth-order b-spline Galerkin method of approximation to the second derivative.

B Numerical details

B.1 Practical solution of discretized Helmholtz problem

The mono-dimensional Helmholtz problems encountered – constituting second-order linear ODEs – are transformed into algebraic equations by applying the Galerkin MWR, viz.

$$\phi'' - \alpha\,\phi = f \quad \longrightarrow \quad [\mathbf{K} - \alpha\,\mathbf{M}]\,\hat{\phi} = \mathbf{M}\,\hat{f} \quad . \tag{80}$$

In general, the solution involves inverting the left hand side operator. However, we might want to take into account different types of boundary conditions:

(i) homogeneous Dirichlet conditions
The first and last line and column of the matrix $[\mathbf{K} - \alpha\,\mathbf{M}]$ are simply suppressed – *condensation.* Afterwards, the first and last component of the solution vector $\hat{\phi}$ are simply set to zero.

(ii) inhomogeneous Dirichet conditions
The problem at hand being linear, we can superpose the solution obeying homogeneous Dirichlet conditions with a simple analytic solution obeying the non-homogeneous conditions, e.g. a straight line:

$$\phi = \phi_{(hom-D)} + \phi_{(lin)}\,, \qquad \phi_{(lin)} = \frac{\phi(L_y) - \phi(o)}{L_y}\,y + \phi(0) \quad , \tag{81}$$

such that the homogeneous part obeys

$$\phi''_{(hom-D)} - \alpha\,\phi_{(hom-D)} = f + \alpha\,\phi_{(lin)}(y)\,,$$

which can be solved as in (i). The final solution is given by (81).

(iii) homogeneous Neumann conditions
Through integration by parts, the stiffness matrix $\mathbf{K}$ can be evaluated as

$$\mathbf{K}_{ij} = \int B''_j(y)\,B_i(y)\,\mathrm{d}y = \underbrace{\left[B'_j(y)\,B_i(y)\right]_0^{2h}}_{\mathbf{K}_1} \underbrace{- \int B'_j(y)\,B'_i(y)\,\mathrm{d}y}_{\mathbf{K}_2}$$

where the expression $\mathbf{K}_1$ represents the contribution of the first derivative on the boundaries, being zero in the present case. Thus we simply solve the system

$$[\mathbf{K}_2 - \alpha\,\mathbf{M}]\,\hat{\phi} = \mathbf{M}\,\hat{f}$$

without applying any condensation.

(iv) non-homogeneous Neumann conditions
We can again use superposition, the non-homogeneous part now being a quadratic function and the homogeneous part a solution according to (iii).

B.2 Analytical solution of homogeneous Helmholtz problem

The homogeneous bi-Helmholtz problem

$$\left.\begin{aligned} \phi'' - \gamma^2\phi &= 0 \\ \psi'' - \beta^2\psi &= \phi \end{aligned}\right\} \tag{82}$$
$$\underline{\text{with}}:\quad \phi(0) = 1,\ \phi(2) = 0,\ \psi(0) = 0,\ \psi(2) = 0$$

has the following solution:

$$
\begin{aligned}
\phi(y) &= -\frac{\left(e^{2\gamma}-e^{2\gamma(y-1)}\right)e^{-\gamma y}}{e^{-2\gamma}-e^{2\gamma}} \\
\psi(y) &= -\left[2\,e^{-2\beta y+\gamma y-2\beta-2\gamma}+e^{\gamma y-6\beta-6\gamma}-2\,e^{\gamma y-6\beta-2\gamma}-e^{2\gamma y-\beta y-6\beta-6\gamma}\right. \\
&\quad -e^{-2\beta y+\gamma y-2\beta+2\gamma}+e^{-\beta y-2\beta+2\gamma}-e^{-2\beta y+\gamma y-2\beta-6\gamma}+e^{\gamma y-6\beta+2\gamma}+e^{2\gamma y-\beta y-6\beta-2\gamma} \\
&\quad +e^{2\gamma y-\beta y-2\beta-6\gamma}-e^{2\gamma y-\beta y-2\beta-2\gamma}+e^{-\beta y-6\beta-2\gamma}-e^{-\beta y-6\beta+2\gamma} \\
&\quad \left.-e^{-\beta y-2\beta-2\gamma}\right]e^{-y(-\beta+\gamma)} \\
&\quad /\left[(\beta+\gamma)(-\beta+\gamma)\left(e^{-4\gamma}-1\right)\left(e^{-6\beta-2\gamma}-e^{-6\beta+2\gamma}-e^{-2\beta-2\gamma}+e^{-2\beta+2\gamma}\right)\right]
\end{aligned}
\tag{83}
$$

However, some of the appearing exponentials can cause overflow when evaluating the expressions numerically at high values of the coefficients γ and β.

B.3 Stability analysis for an advection-diffusion equation

We consider a monodimensional linear advection-diffusion problem, viz.

$$
u_{,t}+a\cdot u_{,x}-\frac{1}{\mathrm{Re}}\,u_{,xx}=0 \quad , \tag{84}
$$

where all quantities are dimensionless. In the following, we wish to analyze the time transient characterisitcs of our b-spline method with respect to the above model problem. To this end we apply the temporal and (wall-normal) spatial discretisation of the full Navier-Stokes solver to the scalar equation (84), i.e. we utilize a three-stage Runge-Kutta scheme together with an implicit sixth order b-spline Galerkin method for the viscous term and a sixth order time-explicit collocation method based on cubic splines and an explicit stencil for the advection term. The discrete system written for a Runge-Kutta substep $n+k/3$ is the following

$$
\underbrace{\left[\mathbf{K}-\frac{\mathrm{Re}}{\Delta t\alpha_k}\mathbf{M}\right]}_{\boldsymbol{A}_k}\cdot\vec{\hat{u}}^{\,n+k/3}=\underbrace{\left[-\frac{\mathrm{Re}}{\Delta t\alpha_k}\mathbf{M}\right]}_{\boldsymbol{B}_k}\cdot\vec{\hat{u}}^{\,n}+\underbrace{\left[\mathrm{Re}\,a\,\mathbf{M}\,\mathcal{S}\,\mathcal{D}\,\mathcal{C}^{-1}\right]}_{\boldsymbol{F}}\cdot\vec{\hat{u}}^{\,n+(k-1)/3} \qquad \alpha_k=\{\frac{1}{3},\frac{1}{2},1\} \quad . \tag{85}
$$

By successive substitution of the operators at each Runge-Kutta substep k, one obtains the operator for a full time step:

$$
\vec{\hat{u}}^{\,n+1}=\left[\boldsymbol{A}_3^{-1}\cdot\boldsymbol{B}_3+\boldsymbol{A}_3^{-1}\cdot\boldsymbol{F}\left\{\boldsymbol{A}_2^{-1}\cdot\boldsymbol{B}_2+\boldsymbol{A}_2^{-1}\cdot\boldsymbol{F}\cdot\boldsymbol{A}_1^{-1}\left(\boldsymbol{B}_1+\boldsymbol{F}\right)\right\}\right]\cdot\vec{\hat{u}}^{\,n} \quad , \tag{86}
$$

where we remark that the variable vectors $\vec{\hat{u}}$ are the b-spline coefficients of the projection $u(x)=\sum_i \hat{u}_i\,B_i(x)$.

B.3.1 Periodic problems

When the flow problem to be solved can be considered as periodic, no specific boundary scheme is needed to close the system of deiscretized equations. In this simple case, one can directly resort to the von Neumann method of stability analysis [9], in which the error ε_i^n is decomposed into Fourier modes

$$
\varepsilon_j^n=\sum_{l=-N}^{N}E_j^n\cdot e^{ji\phi}\,, \qquad \phi=k_l\,\Delta x \quad , \tag{87}
$$

and its amplification by the numerical scheme is examined. Since the error obeys the same discrete evolution equation as the solution, the amplification factor G is given by the eigenvalue of the full step operator in equation (86). For stability, its modulus needs to be smaller or equal to unity.

Once again, the involved matrices are circulant due to periodicity and we obtain the following analytic expression for the amplification factor:

$$
\begin{aligned}
G(\phi,\sigma,\beta) \; = \; & \lambda \big(\boldsymbol{A}_3^{-1} \cdot \boldsymbol{B}_3 + \boldsymbol{A}_3^{-1} \cdot \boldsymbol{F} \left\{ \boldsymbol{A}_2^{-1} \cdot \boldsymbol{B}_2 + \boldsymbol{A}_2^{-1} \cdot \boldsymbol{F} \cdot \boldsymbol{A}_1^{-1} \left(\boldsymbol{B}_1 + \boldsymbol{F} \right) \right\} \big) \\
= \; & \Big(-\frac{1093}{9900} \cos(2\,\phi) - \frac{50879}{6652800} \cos(3\,\phi) - \frac{1623019}{3326400} \cos(\phi) - \frac{1}{19958400} \cos(5\,\phi) \\
& -\frac{509}{4989600} \cos(4\,\phi) - \frac{655177}{1663200} \Big) \Big(\beta \Big(\frac{62}{189} \cos(2\,\phi) + \frac{907}{12096} \cos(3\,\phi) \\
& -1/32 \cos(\phi) + \frac{1}{181440} \cos(5\,\phi) + \frac{25}{9072} \cos(4\,\phi) - \frac{809}{2160} \Big) \\
& -\frac{1093}{9900} \cos(2\,\phi) - \frac{50879}{6652800} \cos(3\,\phi) - \frac{1623019}{3326400} \cos(\phi) - \frac{1}{19958400} \cos(5\,\phi) \\
& -\frac{509}{4989600} \cos(4\,\phi) - \frac{655177}{1663200} \Big)^{-1} - i \Big(\frac{1093}{9900} \cos(2\,\phi) + \frac{50879}{6652800} \cos(3\,\phi) \\
& +\frac{1623019}{3326400} \cos(\phi) + \frac{1}{19958400} \cos(5\,\phi) + \frac{509}{4989600} \cos(4\,\phi) + \frac{655177}{1663200} \Big) \sigma \\
& \Big(\frac{1}{90} \cos(2\,\phi) - \frac{2}{45} \cos(\phi) + \frac{31}{30} \Big) \sin(\phi) \Big(\Big(-\frac{1093}{4950} \cos(2\,\phi) \\
& -\frac{50879}{3326400} \cos(3\,\phi) - \frac{1623019}{1663200} \cos(\phi) - \frac{1}{9979200} \cos(5\,\phi) - \frac{509}{2494800} \cos(4\,\phi) \\
& -\frac{655177}{831600} \Big) \Big(\beta \Big(\frac{62}{189} \cos(2\,\phi) + \frac{907}{12096} \cos(3\,\phi) - 1/32 \cos(\phi) \\
& +\frac{1}{181440} \cos(5\,\phi) + \frac{25}{9072} \cos(4\,\phi) - \frac{809}{2160} \Big) - \frac{1093}{4950} \cos(2\,\phi) \\
& -\frac{50879}{3326400} \cos(3\,\phi) - \frac{1623019}{1663200} \cos(\phi) - \frac{1}{9979200} \cos(5\,\phi) - \frac{509}{2494800} \cos(4\,\phi) \\
& -\frac{655177}{831600} \Big)^{-1} - i \Big(\frac{1093}{9900} \cos(2\,\phi) + \frac{50879}{6652800} \cos(3\,\phi) + \frac{1623019}{3326400} \cos(\phi) \\
& +\frac{1}{19958400} \cos(5\,\phi) + \frac{509}{4989600} \cos(4\,\phi) + \frac{655177}{1663200} \Big) \sigma \Big(\frac{1}{90} \cos(2\,\phi) - \frac{2}{45} \cos(\phi) \\
& +\frac{31}{30} \Big) \sin(\phi) \Big(-\frac{1093}{3300} \cos(2\,\phi) - \frac{50879}{2217600} \cos(3\,\phi) - \frac{1623019}{1108800} \cos(\phi) \\
& -\frac{1}{6652800} \cos(5\,\phi) - \frac{509}{1663200} \cos(4\,\phi) - \frac{655177}{554400} - i \Big(\frac{1093}{9900} \cos(2\,\phi) \\
& +\frac{50879}{6652800} \cos(3\,\phi) + \frac{1623019}{3326400} \cos(\phi) + \frac{1}{19958400} \cos(5\,\phi) + \frac{509}{4989600} \cos(4\,\phi) \\
& +\frac{655177}{1663200} \Big) \sigma \Big(\frac{1}{90} \cos(2\,\phi) - \frac{2}{45} \cos(\phi) + \frac{31}{30} \Big) \sin(\phi) \, (1/3 \cos(\phi) \\
& +2/3)^{-1} \Big) \Big(\beta \Big(\frac{62}{189} \cos(2\,\phi) + \frac{907}{12096} \cos(3\,\phi) - 1/32 \cos(\phi) + \frac{1}{181440} \cos(5\,\phi) \\
& +\frac{25}{9072} \cos(4\,\phi) - \frac{809}{2160} \Big) - \frac{1093}{4950} \cos(2\,\phi) - \frac{50879}{3326400} \cos(3\,\phi) \\
& -\frac{1623019}{1663200} \cos(\phi) - \frac{1}{9979200} \cos(5\,\phi) - \frac{509}{2494800} \cos(4\,\phi) - \frac{655177}{831600} \Big)^{-1} \\
& (1/3 \cos(\phi) + 2/3)^{-1} \Big(\beta \Big(\frac{62}{189} \cos(2\,\phi) + \frac{907}{12096} \cos(3\,\phi) - 1/32 \cos(\phi) \\
& +\frac{1}{181440} \cos(5\,\phi) + \frac{25}{9072} \cos(4\,\phi) - \frac{809}{2160} \Big) - \frac{1093}{3300} \cos(2\,\phi)
\end{aligned}
$$

$$
\begin{aligned}
&-\frac{50879}{2217600}\cos(3\,\phi)-\frac{1623019}{1108800}\cos(\phi)-\frac{1}{6652800}\cos(5\,\phi)-\frac{509}{1663200}\cos(4\,\phi)\\
&-\frac{655177}{554400}\Big)^{-1}\Big)\Big(\beta\Big(\frac{62}{189}\cos(2\,\phi)+\frac{907}{12096}\cos(3\,\phi)-1/32\cos(\phi)+\frac{1}{181440}\cos(5\,\phi)\\
&+\frac{25}{9072}\cos(4\,\phi)-\frac{809}{2160}\Big)-\frac{1093}{9900}\cos(2\,\phi)-\frac{50879}{6652800}\cos(3\,\phi)\\
&-\frac{1623019}{3326400}\cos(\phi)-\frac{1}{19958400}\cos(5\,\phi)-\frac{509}{4989600}\cos(4\,\phi)-\frac{655177}{1663200}\Big)^{-1}\\
&(1/3\cos(\phi)+2/3)^{-1}\quad ,
\end{aligned}
\tag{88}
$$

where

$$
\sigma=\frac{a\,\Delta t}{\Delta x},\quad \beta=\frac{\Delta t}{\Delta x^2\,\mathrm{Re}},\quad -\pi\le\phi\le\pi\quad . \tag{89}
$$

For a given value of the CFL number σ and a fixed Peclet number $\mathrm{Pe}=\sigma/\beta$, the amplification characteristics of the scheme are thus completely determined over the range of the spectrum for the phase angle ϕ.

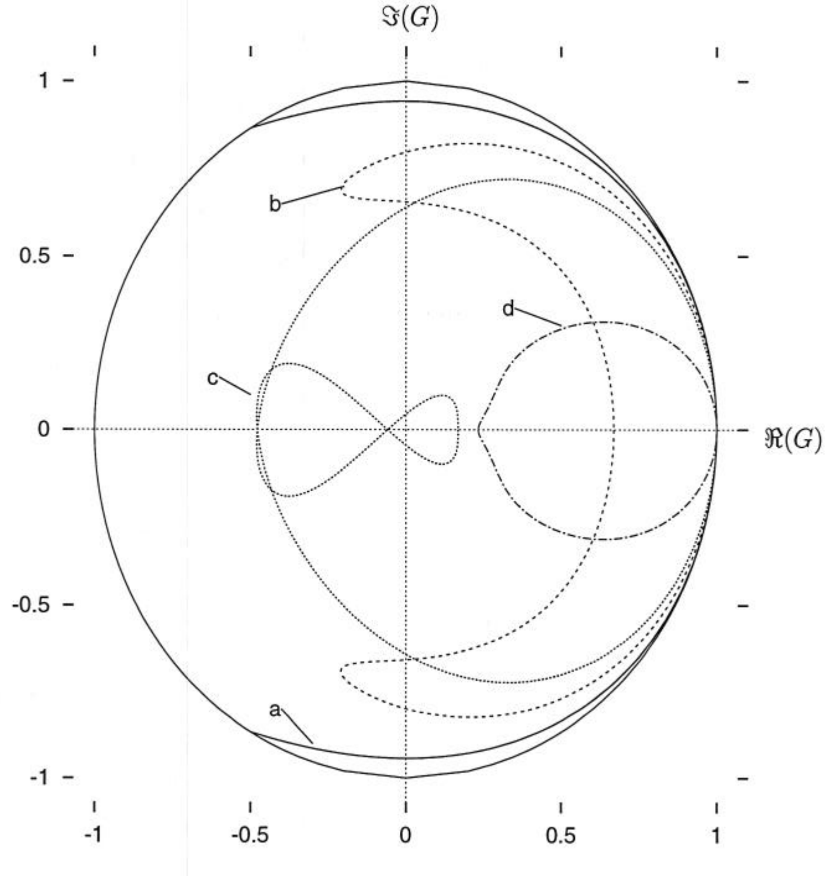

Figure 51: Amplification factor $G(\phi,\sigma,\beta)$ of the discretized advection-diffusion problem in the complex plane: (a) $\sigma=0.95$, $\sigma/\beta\to\infty$, (b) $\sigma=0.95$, $\sigma/\beta=19$, (c) $\sigma=2$, $\sigma/\beta=4$, (d) $\sigma=0.5$, $\sigma/\beta=1.5$.

In figure 51 we have plotted the complex amplification function $G(\phi)$ for several values of the parameter pair $(\sigma,\sigma/\beta)$. It is difficult to obtain a stability limit in closed form, but individual values can be verified in this manner. The proposed scheme is seen to be stable in the inviscid limit up to a CFL value of around 0.95. For finite Peclet numbers, the allowable time step is larger.

B.3.2 Non-periodic problems

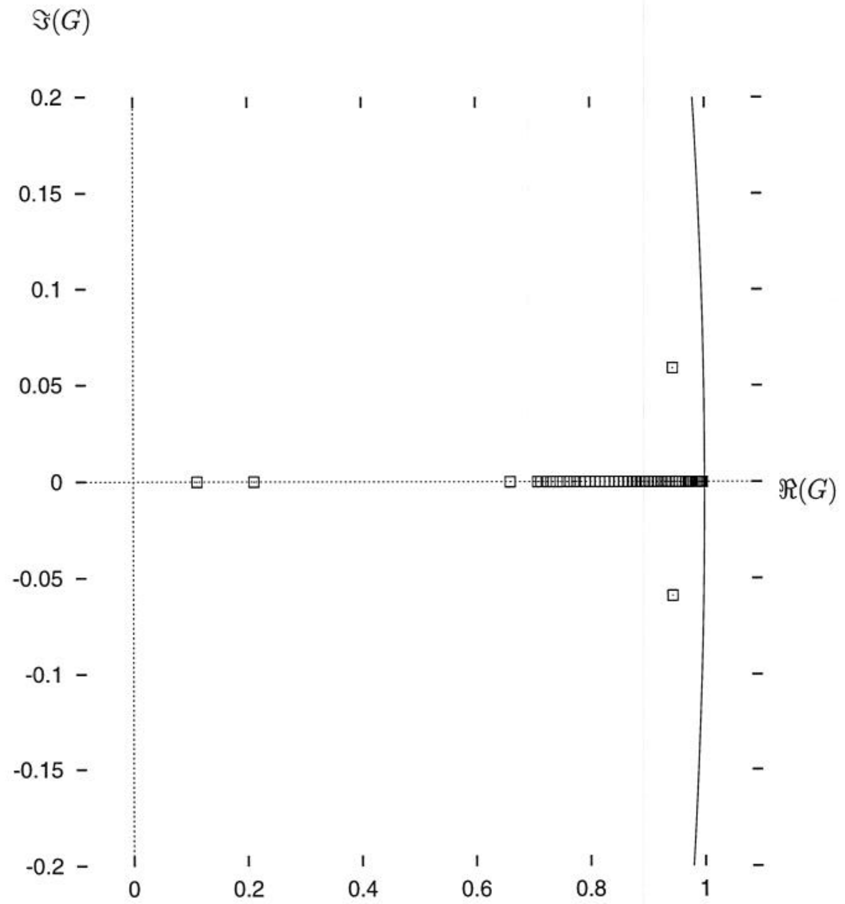

Figure 52: Eigenvalues of the space-time operator $G(\sigma, \beta, N_x)$ of the discretized advection-diffusion problem in the complex plane using a homogeneous Neumann condition at the outflow boundary. $N_x = 50$, $\sigma = 0.1$, $\sigma/\beta = 0.16$.

In general, one is interested in non-periodic flow problems (otherwise, a full spectral method would probably be preferable) for which the discretization has to be modified at the boundaries. In this case, a von Neumann analysis is no longer viable and we employ the so-called matrix method of stability analysis [9], which essentially consists in performing an eigensystem analysis of the operator matrix constructed for a certain computational mesh. In this case, a closed analytic expression for the amplification factor can in general not be obtained and the eigenvalues need to be calculated discretely. Consequently, the individual matrices contributing to G in equation (86) need to be constructed explicitely while incorporating all boundary corrections:

(i) corrections stemming from the fact that the numerical stencil cannot be carried without modification up to the boundary nodes as discussed in appendices A.1.5 and A.2;

(ii) modifications incorporating the physical boundary conditions of the flow problem.

Since the physical flow situation (in wall-normal direction) of our porous plane channel flow cannot be mimicked in a monodimensional framework for reasons of continuity, we consider an inflow/-

outflow configuration. At the inflow ($x = 0$ for positive advection speed $a > 0$) we impose a Dirichlet condition via the condensation method shown in appendix B.1. The actual value that is imposed at that point does not enter the stability considerations since this non-homogeneous contribution $\boldsymbol{Q}$ (see below) to the operator does not affect the characteristics of the transient behaviour of the solution [9]. At the outflow boundary ($x = L_x$) we impose:

(a) a homogeneous Neumann condition (zero gradient) as explained in appendix B.1;

(b) we consider a simple convective condition based on discretizing the equation $u_{,t} + au_{,x} = 0$ at $x = L_x$ by a first order upwind formula such that the entries in the last row of the operator in physical space read $G_{N_x l} = [0, \ldots, 0, 2\sigma, 1 - 2\sigma]$.

The full scheme can now be written as

$$\vec{\hat{u}}^{n+1} = \boldsymbol{G}(\sigma, \beta, N_x) \cdot \vec{\hat{u}}^{n} + \boldsymbol{Q} \quad . \tag{90}$$

The eigenvalues λ_i of the $N_x \cdot N_x$ matrix $\boldsymbol{G}$ should all be contained within the unit circle in the complex plane for stability,

$$|\lambda_i| \leq 1 \qquad \forall \qquad i = 1 \ldots N_x \quad . \tag{91}$$

Figures 52 and 53 show the eigenvalue distribution for a grid consisting of 50 b-splines of order

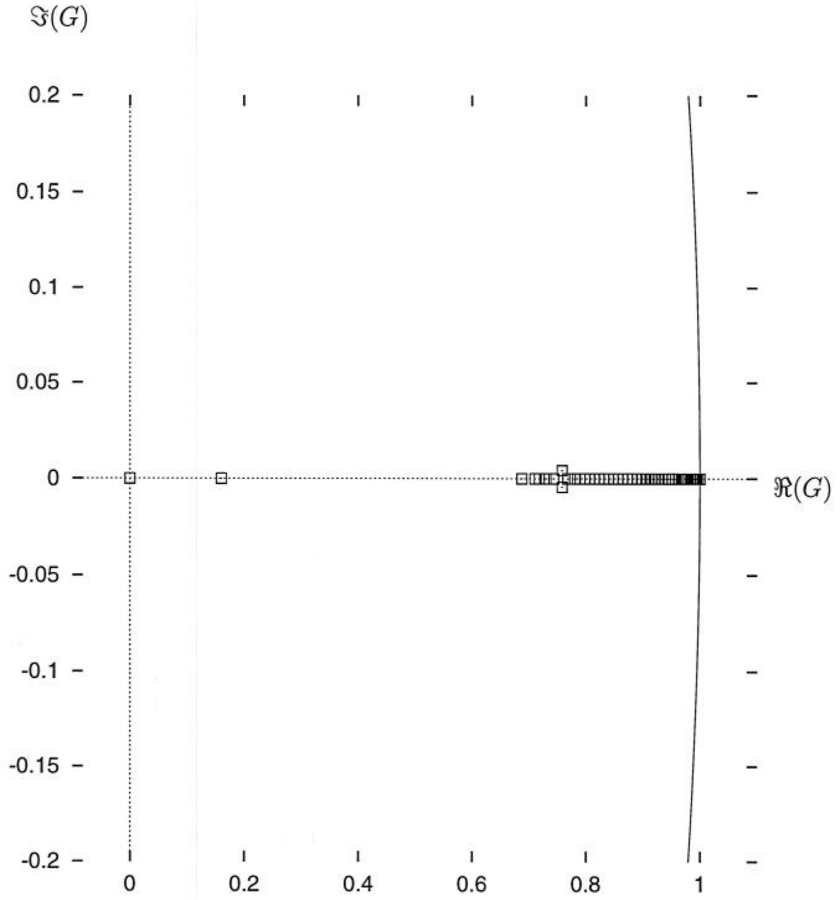

Figure 53: Eigenvalues of the space-time operator $G(\sigma, \beta, N_x)$ of the discretized advection-diffusion problem in the complex plane using a convective condition at the outflow boundary. $N_x = 50$, $\sigma = 0.1$, $\sigma/\beta = 0.16$.

$o = 6$, i.e. 46 collocation points distributed equidistantly plus 4 supplementary points in the two intervals at the extrema (cf. appendix A.2). Parameter values representative of our full DNS runs are chosen: the CFL condition is set to $\sigma = 0.1$ and the Peclet number is fixed at $\sigma/\beta = 0.16$. The eigenvalues are seen to be nearly purely real with the exception of a complex conjugate pair depending on the outflow boundary treatment. In fact, use of the convective condition leads to increased damping which can be explained by the dissipative first order scheme employed. We remark that this latter outflow boundary treatment is not used in our DNS method and is only shown for comparison.

C Calculation of two-point autocorrelations

Remembering that we are dealing with a flow that possesses two statistically homogeneous directions (x, z), let us define the two-point autocorrelation of the fluctuations of a function $f(x, z)$ by the following formula

$$\begin{aligned} \overline{R_{iif}}(r_i) &= \overline{< f'(x_i, x_j, t) \cdot f'(x_i + r_i, x_j, t) >} \\ &= \int_{t_1}^{t_2} \int_0^{L_{x_i}} \int_0^{L_{x_j}} f'(x_i, x_j, t) \cdot f'(x_i + r_i, x_j, t) \mathrm{d}x_j \mathrm{d}x_i \mathrm{d}t\,, \end{aligned} \tag{92}$$

where

$$j, i = \{1, 3\}, \quad i \neq j, \quad 0 < r_i < L_{x_i}, \quad x_i = [x, y, z]^T\,,$$

and the fluctuation being defined as the difference between the instantaneous value of the function and its planewise and temporal average:

$$f'(x_i, x_j, t) = f(x_i, x_j, t) - \frac{1}{(t_2 - t_1)\, L_{x_i} L_{x_j}} \int_{t_1}^{t_2} \int_0^{L_{x_i}} \int_0^{L_{x_j}} f(x_i, x_j, t) \mathrm{d}x_j \mathrm{d}x_i \quad . \tag{93}$$

We remark that the dependence of f on the wall-normal direction y does not enter the following considerations but only signifies that we are working in a plane of the three-dimensional domain. Also note that the temporal integration in (92) is just a simple accumulation of the values at each time step.

C.1 Integration in Fourier space

We use the fact that the two-point autocorrelations and the spectral energy density are a Fourier transform pair (the symbol "$\Longleftrightarrow$" denoting a Fourier transform in either direction), viz.

$$R_{iif}(r_i) \Longleftrightarrow E_{ii}(k_i) \quad , \tag{94}$$

where

$$\begin{aligned} E_{ii}(k_i) &= \int_{k_j} E_{ii}(k_i, k_j) \mathrm{d}k_j \qquad i \neq j \\ E_{ii}(k_i, k_j) &= F'(k_i, k_j) \cdot F'^*(k_i, k_j) \\ f'(x_i, x_j) &\Longleftrightarrow F'(k_i, k_j)\,, \end{aligned}$$

and $()^*$ denoting a complex conjugate. The important point is to perform the integration over the second direction (x_j) in Fourier space [2, p.35]. Another, more technical aspect is the arrangement of the data in Fourier space in the arrays that are used in the actual bidimensional discrete Fourier transforms.

C.1.1 Details of bidimensional discrete Fourier transform

We perform first a real to complex discrete FFT in the streamwise direction x, viz.

$$\widetilde{F}(k_x, z) = \frac{1}{2} \sum_{n=0}^{N_x - 1} f(x_n, z) \cdot e^{2\pi i n k_x / N_x} \quad . \tag{95}$$

For $f(x, z)$ being real, we know that $\widetilde{F}(-k_x, z) = \widetilde{F}^*(k_x, z)$ and thus we only keep in memory the coefficients corresponding to positive wavenumbers. The dimension in Fourier space of the first index (corresponding to streamwise wavenumbers) is thus $(0 : N_x/2 - 1)$ and wavenumbers are arranged in ascending order from the constant mode on upwards.

In the spanwise (z) direction, a complex to complex FFT is performed subsequently, viz.

$$F(k_x, k_z) = \frac{1}{2} \sum_{n=0}^{N_z-1} \widetilde{F}(k_x, z_n) \cdot e^{2\pi i n k_z / N_z} \quad . \tag{96}$$

Here, we store all N_z values along the second index of the array F. The way the wavenumbers are arranged follows the explanation in reference [28, p. 497]. Positive wavenumbers occupy the first $(N_z/2-1)$ slots in ascending order (the zero mode corresponds to the index 0) and negative wavenumbers occupy positions $(N_z/2+1)$ to (N_z-1) in descending absolute value.

C.1.2 Algorithm for correlation computation

We actually perform only the time integration of the spectral energy density at run time, while the remaining procedure is done by a post-processor module once the statistics have been obtained.

At <u>run time</u> we perform the following steps:

```
at each time step $t_n$
    for each positive streamwise mode $k_x$: $0 \le i \le N_x/2 - 1$
        for each spanwise mode $k_z$: $0 \le j \le N_z$
            • accumulate spectral energy density
              $\mathtt{SED}(i,j) = \mathtt{SED}(i,j) + F(k_x,k_z) \cdot F^*(k_x,k_z)$        (97)
```

We remark that the spectral energy density constitutes the square of the module of the function at each wavenumber pair (k_x, k_z) and is thus equal for negative and positive streamwise wavenumbers (k_x) that have the same absolute value and whose corresponding coefficients were above seen to be complex conjugates.

Sine we do not have access to the time-averaged mean value $\overline{<f>}$ during the process of accumulation, we need to correct the result such that the correlation according to definition (92) is obtained. Using the correlation theorem (94) we can write:

$$\begin{aligned}
\overline{R_{iif}(r_i)} \quad &\Longleftrightarrow \quad \overline{\int_{k_j} F'_{ij} \cdot F'^{*}_{ij} \, \mathrm{d}k_j} \\
&= \quad \overline{\int_{k_j} \left(F_{ij} - \overline{F_{00}}\,\delta_0^0\right) \cdot \left(F^*_{ij} - \overline{F_{00}}\,\delta_0^0\right) \mathrm{d}k_j} \\
&= \quad \int_{k_j} \left[\overline{F_{ij}F^*_{ij}} + \overline{F_{00}}^2\,\delta_0^0 - \overline{F_{ij}\overline{F}_{oo}}\delta_0^0 - \overline{F^*_{ij}\overline{F}_{oo}}\delta_0^0\right] \mathrm{d}k_j \\
&= \quad \int_{k_j} \left[\overline{F_{ij}F^*_{ij}} - \overline{F_{00}}^2\,\delta_0^0\right] \mathrm{d}k_j \\
&= \quad \begin{cases} \overline{\int_{k_j} F_{ij}F^*_{ij}\,\mathrm{d}k_j} & \text{if} \quad \delta_0^0 = 0 \\[2ex] \overline{F^2_{00}} - \overline{F_{00}}^2 & \text{if} \quad \delta_0^0 = 1 \end{cases} \qquad ,
\end{aligned} \tag{98}$$

where $\delta_i^j = 1$ if $i = j = 0$ (otherwise zero), and $F_{ij} = F(k_i, k_j)$.

At post-processing level we perform the following operations on the data accumulated according to (97):

- set $\texttt{SED}(0,0) = \texttt{SED}(0,0) - \overline{F(0,0)}^2$

for each positive streamwise mode k_x: $0 \leq i \leq N_x/2 - 1$

- sum over spanwise wavenumbers:

$$\texttt{SEDX}(k_x) = \sum_{k_z=0}^{N_z} \texttt{SED}(k_x, k_z)$$

for each spanwise mode k_z: $0 \leq j \leq N_z$

- sum over streamwise wavenumbers:

$$\texttt{SEDZ}(k_z) = \texttt{SED}(0, k_z) + 2 \sum_{k_x=1}^{N_x/2-1} \texttt{SED}(k_x, k_z) \tag{99}$$

- backtransform to physical space:
  $\texttt{CORR}(r_x) \Longleftrightarrow \texttt{SEDX}(k_x)$
  $\texttt{CORR}(r_z) \Longleftrightarrow \texttt{SEDZ}(k_z)$

- normalize:

$$\overline{R_{iif}}(r_i) = \frac{\texttt{CORR}(r_i)}{\texttt{CORR}(0)}$$

The following remarks apply to the algorithm (99):

- In fact the value of the zero mode SED(0,0) can be set by taking into account that

  $$\overline{F_{00}^2} - \overline{F_{00}}^2 = \overline{(F_{00} - \overline{F}_{00})^2} = \overline{F_{00}'^2}$$

  This corresponds to the square of the rms value of the fluctuations of f accumulated by the usual statistics module.

- The sum over streamwise modes (k_x) needs to account for the missing negative wavenumbers that are not explicitely stocked in the actual array. Thus a factor of 2 appears in front of the respective sum for non-zero wavenumbers.

D Potential flow due to point vortices above a porous surface

We consider inviscid flow in a plane (x, y) and assume that vorticity is concentrated in discrete singularities (point vortices) such that the flow is potential and there are analytic velocities everywhere else:

$$w^*(z) = u^* - \mathrm{i}\,v^*\,, \qquad z^* = x^* + \mathrm{i}\,y^*\,. \tag{100}$$

Assuming unit density, the pressure is given by Bernoulli's equation

$$p^* = p_0^* - \frac{1}{2}\,|w^*|^2 \quad , \tag{101}$$

and Darcy's relation $v^* = -\beta^* \cdot p^*$ gives the following boundary condition at the wall $(y^* = 0)$

$$\Im(w^*(z^* = x^*)) = b^* - \frac{\beta^*}{2}\,|w^*(z^* = x^*)|^2 \quad . \tag{102}$$

The constant b^* is adjusted such that the mean volume flux across the surface is zero, viz.

$$b^* = \frac{\beta^*}{2} < |w^*(x^*)|^2 > \quad , \tag{103}$$

where the average is defined along the horizontal coordinate

$$< \phi > = \lim_{X_0 \to \infty} \left\{ \frac{1}{2X_0} \int_{-X_0}^{X_0} \phi(x)\mathrm{d}x \right\} \quad . \tag{104}$$

Let us consider an infinite array of point vortices with individual circulation Γ^*, equally spaced at intervals of $\lambda^* = \pi\,H^*/\alpha$ and located at a uniform height H^* above the surface (figure 54). We perform the following normalization of variables:

$$w = \frac{H^*}{\Gamma^*}\,w^*\,, \quad z = \frac{z^*}{H^*}\,, \quad \beta = \frac{\Gamma^*}{2\,H^*}\beta^*\,, \quad b = b^*\frac{H^*}{\Gamma^*}\,. \tag{105}$$

The velocity field induced by a single vortex at z_0 is

$$w_s = \frac{1}{2\pi\,\mathrm{i}}\,\frac{1}{z - z_0} \quad , \tag{106}$$

such that the row of vortices is described by

$$w_+ = \frac{\alpha}{2\,\pi\,\mathrm{i}}\cot\left(\alpha(z - \mathrm{i})\right) \quad . \tag{107}$$

In the impermeable case $(\beta = 0)$ the wall has the well-known effect of a mirror, i.e. vortices of equal strength and opposite sign are located on the other side of the boundary $y = 0$. The full velocity field of a row of vortices above an impermeable wall can thus be written as

$$w_0 = \frac{\alpha}{2\,\pi\,\mathrm{i}}\left[\cot\left(\alpha(z - \mathrm{i})\right) - \cot\left(\alpha(z + \mathrm{i})\right)\right] \quad . \tag{108}$$

In the porous case $(\beta > 0)$ the wall boundary condition (102) is quadratic due to the pressure. In the following we will suppose that porosity takes small values $(\beta \ll 1)$. In fact, a straightforward linearization of (102) lets us obtain an approximation of the induced velocity field in the case of a porous wall. However, when computing the *rms* intensity of velocity – which is the quantity of interest with respect to the statistical results of our DNS – the linearized velocity is of little use since neglected terms can be of the same order as retained ones. We will thus apply a rescaling that is valid close to the surface allowing us to select the significant terms of the next level of approximation.

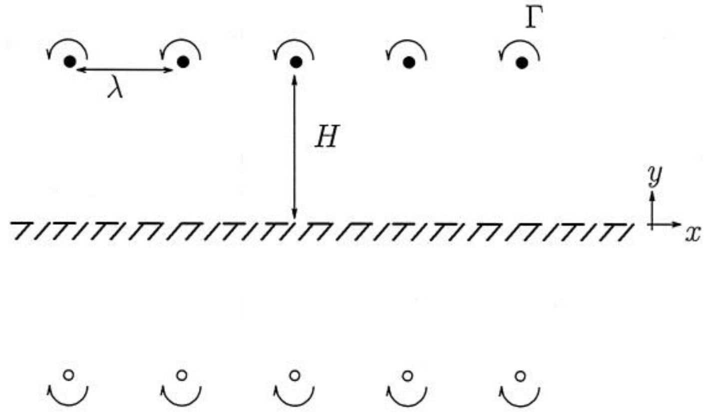

Figure 54: An array of equally spaced point vortices of individual circulation Γ and their counter-rotating images on the opposite side of the surface.

Let the velocity be expnded as

$$w = w_0 + \beta \cdot w_1 + \beta^2 \cdot w_2 + \dots \quad , \tag{109}$$

so that, for example,

$$< v^2 >=< v_0^2 > +2\beta < v_o v_1 > +\beta^2 \left(< v_1^2 > +2 < v_0 v_2 >\right) + \mathcal{O}(\beta^3) \quad . \tag{110}$$

Looking at the zeroth order velocity w_0, rewritten as follows from (108),

$$w_0 = \frac{\alpha}{\pi} \frac{\sinh(2\alpha)}{\cosh(2\alpha) - \cos(2\alpha z)} \quad , \tag{111}$$

we get for small wall-distances $y \ll 1$ (using $\sin(ay) \approx ay$, $\cos(ay) \approx 1$ and performing a series expansion up to first order in y):

$$w_0 \approx \frac{\alpha}{\pi} \frac{\sinh(2\alpha)}{\cosh(2\alpha) - \cos(2\alpha x)} \left[1 - \frac{2\alpha\,\mathrm{i}\sin(2\alpha x)}{\cosh(2\alpha) - \cos(2\alpha x)} \cdot y\right] \quad , \tag{112}$$

and for the vertical velocity:

$$v_0 = \frac{\alpha^2}{2\pi} \frac{\sinh(2\alpha)\sin(2\alpha x)}{(\sinh^2(\alpha) + \sin^2(\alpha x))^2} \cdot y \quad . \tag{113}$$

We note that, in this inviscid case, (113) is directly proportional to the wall distance such that we can introduce the following new variables

$$\widetilde{y} = y/\beta\,, \quad \widetilde{v}_0 = v_0/\beta \quad , \tag{114}$$

which leads to

$$< v^2 >= \beta^2 \left[< \widetilde{v}_0^2 > +2 < \widetilde{v}_o v_1 > + < v_1^2 >\right] + \mathcal{O}(\beta^3)\,, \qquad y = \mathcal{O}(\beta) \quad . \tag{115}$$

Expanding the frst order velocity v_1 in terms of the new variable $\widetilde{y}$ gives

$$v_1 = v_1(0) + v_1'(0) \cdot y + \ldots = v_1(0) + v_1'(0) \cdot \beta\widetilde{y} + \mathcal{O}(\beta^2) \quad , \tag{116}$$

of which we can only retain the first (constant) term in order to maintain the order of the approximation (115). Substituting $\widetilde{v}_0 = v_0' \cdot \widetilde{y}$ and $v_1 \approx v_1(0)$ into (115) leads to

$$< v^2 >= \beta^2 \left[< v_{0,y}^2 > \widetilde{y}^2 + 2 < v_0' v_1(0) > \widetilde{y} + < v_1(0)^2 >\right] + \mathcal{O}(\beta^3)\,, \qquad y = \mathcal{O}(\beta) \quad , \tag{117}$$

where v_0' is given by the derivative of (113) with respect to y. In order to determine $v_1(0)$ we consider the boundary condition (102), which – in the linear approximation $w \approx w_0 + \beta w_1$, $b \approx b_0 + \beta b_1$ – reads

$$\Im(w_1) = -|w_0|^2 + b_1 \quad , \tag{118}$$

since $\Im(w_0) = 0$ (impermeability for $\beta = 0$) and $b_0 = 0$ (same reason). The constant term is obtained by the zero-mass-flux-condition (103), viz.

$$b_1 =< |w_0|^2 >=< u_0^2 > \quad , \tag{119}$$

so that we obtain

$$v_1(0) = u_0^2 - < u_0^2 > \quad . \tag{120}$$

We further note that from continuity $v_{0,y} = -u_{0,x}$ it results that

$$< v_{0,y}\, v_1(0) >= - < u_{0,x} (u_0^2 - < u_0^2 >) >= 0 \tag{121}$$

because of the periodicity of the function $u_0(x)$. The expression for the intensity of induced wall-normal velocity is finally

$$< v^2 >=< v_0'^2 > y^2 + \beta^2 \left[< (u_0^2 - < u_0^2 >)^2 > \right] , \qquad y = \mathcal{O}(\beta) \quad . \tag{122}$$

Using v_0' from (113) and the horizontal velocity at the wall

$$u_0 = \frac{\alpha}{2\pi} \frac{\sinh(2\alpha)}{\sinh^2(\alpha) + \sin^2(\alpha x)} \tag{123}$$

(real part of (113)), the integrals in (122) can be evaluated numerically as a function of vortex period α,

$$< v^2 >= A(\alpha) \cdot y^2 + \beta^2 \cdot B(\alpha) \quad , \tag{124}$$

where

$$\begin{aligned} A &= < \left\{ \frac{\alpha^2}{2\pi} \frac{\sinh(2\alpha)\sin(2\alpha x)}{(\sinh^2(\alpha) + \sin^2(\alpha x))^2} \right\}^2 >, \\ B &= < \left\{ \frac{\alpha}{2\pi} \frac{\sinh(2\alpha)}{\sinh^2(\alpha) + \sin^2(\alpha x)} \right\}^4 > - < \left\{ \frac{\alpha}{2\pi} \frac{\sinh(2\alpha)}{\sinh^2(\alpha) + \sin^2(\alpha x)} \right\}^2 >^2 . \end{aligned}$$

Let us now evaluate (124) using data from channel flow. In the experiments, vortex intervals are found to be of the order of the lateral spacing of streaks, i.e. 100 (140) wall units in *case 16* (*case 15*). Together with an average vortex height H of approximately 20 wall units, the corresponding non-dimensional wavenumber α of the model vortex array is $\pi/5$ ($\pi/7$ respectively). The numerical values of the coefficients of (124) are the following:

α	$A(\alpha)$	$B(\alpha)$
$\pi/5$	$1.146 \cdot 10^{-2}$	$1.357 \cdot 10^{-3}$
$\pi/7$	$1.223 \cdot 10^{-2}$	$1.212 \cdot 10^{-3}$

.

In order to allow for a quantitative comparison with DNS data, it has to be taken into account that we have so far only considered motion in the spanwise cross-section of the channel. One simple correction could be the assumption of vortices that follow a sine-like distribution in the streamwise direction, which means that the *rms* (square root of Eq. (124)) should be corrected by a factor of $1/\sqrt{2}$.

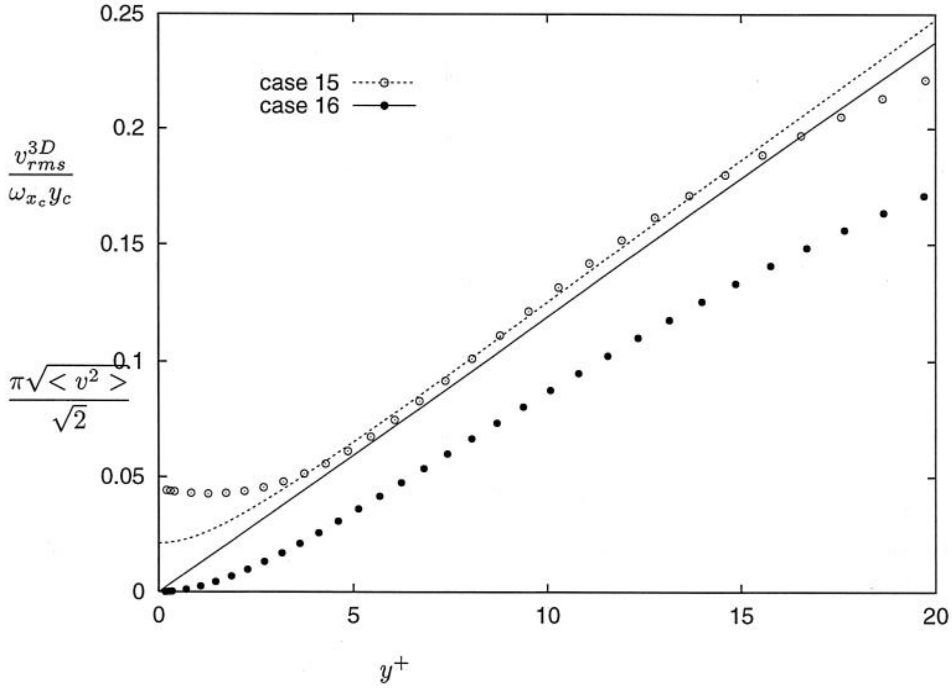

Figure 55: Comparison of the wall-normal velocity fluctuation from DNS (symbols) and from the point vortex model (lines). The DNS data v_{rms}^{3D} corresponds to the stream- and spanwise *rms* intensity of the fluctuations of wall-normal velocity from which the purely two-dimensional intensity in (x, y)-plane has been subtracted. The curves of the point vortex model correspond to formula (124), where the factor $\pi/\sqrt{2}$ is introduced by the normalization as explained in the text. Note that the analytic expression is valid in the range of $y^+ \ll y_c$, where $y_c \approx 20$.

Concerning the normalization of the variables of the vortex model with respect to variables from the main body of this report (cf. §2), we have for porosity:

$$\beta = \frac{\pi}{2\,C_\beta}\,H^+\,\omega_x^+\,\mathrm{Re}_\tau \quad , \tag{125}$$

assuming that the circulation can be expressed by the vortex strength as $\Gamma^* = \omega_x^*\,H^{*2}\,\pi$. The numerical values for the vortex strength and height are taken as the local maximum values indicated in figure 13. Porosity is indeed found to be small, i.e. $\beta = 0.253$ (0.189) in *case 15* (*case 8*).

A comparison of formula (124) with *rms* intensities from our DNS is presented in figure 55. The contribution of two-dimensional fluctuations in the (x, y)-plane of the channel has been subtracted for this representation since that motion does not correspond to the mechanism modelled here. A rather good agreement of the slope with both curves of the simulation is achieved by the simple point vortex model. The offset between the porous *case 15* and the impermeable *case 16* is underestimated. We conclude from the present considerations that the increase of induced wall-normal velocity fluctuations near a porous surface – and consequently the increase in advective streak formation – can be attributed to a direct modification of the velocity potential. In other words, the vortex-induced velocity field near a porous wall is less constrained by the boundary.